2D Modeling of Lower Mantle Structure with WKM Synthetics

Thesis by

Sidao Ni

In Partial Fulfillment of the Requirements
for the Degree of
Doctor of Philosophy

Caltech
Pasadena, California

2001
(Submitted February 02, 2001)

Dedicated to **Nihuai Village,**
a small community in a remote area,
where I was born and raised.

Acknowledgements

It has been a great experience to study as a graduate student at the Seismological Laboratory for five years, both chalenging and enjoyable. I am grateful to many professors and fellow students, as well as postdocs and visiting scholars in this laboratory for their kind help. Among them, I feel indebted to Prof. Don Helmberger, who is insightful and considerate. He is a great advisor, providing help not only in science field but also in many other aspects. I also express special thanks to Prof. Thomas Ahrens, my academic advisor, who helped me in choosing courses and guided me to pass oral exams. Instructive discussions with Prof. Hiroo Kanamori helped me in understanding how much the source (Earthquake) could affect the waveform modeling. Prof. Rob Clayton has always been available for helping me in accessing SCEC data and for his beneficial course GE256 from which I learned basic skills of signal processing. Prof. Mike Gurnis has been a great help on my SEDI projects; he also has reviewed many manuscripts of mine and provided very good advice on improving them. Thanks, Prof. Yuk Yung, for hosting Chinese students on Thankgiving Day.

I also thank all the graduate students in this laboratory: Emily Brodsky always gives good suggestions when I have questions about physics of earthquake; Leo Eisner asks critical questions about the theoretical seismology aspect of my WKM code. Special thanks to Dr. Xiaoming Ding who laid down the important framework of WKM; he is very nice and warmhearted, and he provided important help in my first a few months in the US. Thanks to Dr. Xi Song, Lianxing Wen, and Lupei Zhu for various help. Fruitful discussions with Chen Ji, Brian Savage and Jascha Polet helped me in my understanding more about the Earth. Magali Billen and Julie Norith, once my office-mates, helped a lot on improving my English.

Evilnia Cui and Sue Yamada are very nice to students and helped me a lot in dealing with the work of submitting papers and traveling for conferences.

The IRIS DMC, Geoscope, GEOFON and German Array have been indispensable

sources of help; without them, my research would be groundless.

My wife, Dongdong Niu, has been a great support of my studies with her steadfast encouragement and care.

Abstract

The Earth is very heterogeneous, especially in the region close to the surface of the Earth, and in regions close to the core-mantle boundary (CMB). The lowermost mantle (bottom 300km of the mantle) is the place for fast anomaly (3% faster S velocity than PREM, modeled from Scd), for slow anomaly (-3% slower S velocity than PREM, modeled from S,ScS), for extreme anomalous structure (ultra-low velocity zone, 30% lower in S velocity, 10% lower in P velocity). Strong anomaly with larger dimension is also observed beneath Africa and Pacific, originally modeled from travel time of S, SKS and ScS. Given the heterogeneous nature of the earth, more accurate approach (than travel time) has to be applied to study the details of various anomalous structures, and matching waveform with synthetic seismograms has proven effective in constraining the velocity structures. However, it is difficult to make synthetic seismograms in more than 1D cases where no exact analytical solution is possible. Numerical methods like finite difference or finite elements are too time consuming in modeling body waveforms. We developed a 2D synthetic algorithm, which is extended from 1D generalized ray theory (GRT), to make synthetic seismograms efficiently (each seismogram per minutes). This 2D algorithm is related to WKB approximation, but is based on different principles, it is thus named to be WKM, i.e., WKB modified. WKM has been applied to study the variation of fast D" structure beneath the Caribbean sea, to study the plume beneath Africa. WKM is also applied to study PKP precursors which is a very important seismic phase in modeling lower mantle heterogeneity. By matching WKM synthetic seismograms with various data, we discovered and confirmed that (a) The D" beneath Caribbean varies laterally, and the variation is best revealed with Scd+Sab beyond 88 degree where Scd overruns Sab. (b) The low velocity structure beneath Africa is about 1500 km in height, at least 1000km in width, and features 3% reduced S velocity. The low velocity structure is a combination of a relatively thin, low velocity layer (200km thick or less) beneath the Atlantic, then rising very sharply into mid mantle towards Africa. (c) At the edges of this huge Africa low velocity structures, ULVZs are found by modeling the large separation between S and ScS beyond 100 degree. The ULVZ to the eastern boundary was discovered with SKPdS data, and later is confirmed by PKP precursor data. This is the first time that ULVZ is verified with distinct seismic phase.

Contents

List of Figures

List of Tables

Chapter 1 Introduction

Perhaps seismology is the most important tool in the study of the structure of Earth. There are different branches of seismology that provide constraints on the modeling of the Earth; these include, for example:

- Normal modes modeling is sensitive to large scale structure and provides information about density contrast.
- Travel time tomography assumes small perturbation of velocity structure, therefore, assuming seismic arrivals are advanced or delayed , yet with nondisturbed waveforms.
- Waveform modeling stresses the effects of velocity structures on waveforms. Triplication (e.g., Scd *Lay and Helmberger* [1983]), multipathing (split PKPab,*Luo et al.* [2001]), diffraction (longer period S beyond 90 degree, this study) of certain seismic phases provide very important information about the smaller scale (than tomography) variation of velocity which is hard to resolve.

Among these branches, waveform modeling is crucial in revealing detailed structures, e.g., both the velocity jump in D" and the Ultra Low Velocity Zone (ULVZ, which is presumed to have 10% reduction in P velocity, 30% reduction in S velocity) have been discovered with waveform studies. Typically waveform modeling involves (1) a forward velocity model, (2) an algorithm to construct theoretical seismograms for the model, (3) match the synthetic seismograms with observed data, and (4) find the difference, then back to (1) by changing the velocity model, until satisfactory match is achieved. For 1D velocity models, a few algorithms have been developed to compute synthetics seismograms, e.g., Generalized Ray theory, *Helmberger et al.* [1996b]; Frequency-wave number (FK) method; Normal model summation. All these methods are applied in various studies where 1D modeling is appropriate.

However, the Earth is heterogeneous, not only radially (1D), but also laterally (3D). In some situations, the lateral heterogeneity can be up to tens of percent (e.g., ULVZ), where small perturbations may not be valid. To apply waveform modeling for these regions a 2D or 3D synthetic algorithm is required. Finite difference or finite element and their variants (pseudo spectrum, spectrum element) provide accurate results, but are computationally expensive. Wen and Helmberger [1998a] developed a hybrid method by interfacing 1D GRT synthetics with 2D numerical synthetics which reduces computation time substantially while proving effective in modeling ULVZ structures. However, this method can be used where the anomalous region is spatially limited so that the numerical computation for the anomalous region is not overwhelming.

Through this thesis, we propose an approximate analytical algorithm to construct synthetic seismograms for 2D heterogeneous media, and apply this algorithm to model various velocity structures. The advantage of an approximate analytical approach is that it produce synthetics fast while maintaining accuracy. In the following chapters, we show how this algorithm works (chapter 2); apply this method to fast D" to model Scd variation (chapter 2); then apply this method to study slow velocity anomaly beneath Africa (chapters 3, 5); and finally apply this method to ULVZ and predict details of PKP precursors (chapter 6).

Our goal is not limited to refined algorithms for the solution of synthetic seismograms, rather we hope to understand the velocity structure with the application of the algorithms and comparison to detailed record sections. Thus 1D waveform modeling (chapter 4) is combined with 2D modeling to constrain the velocity structure beneath Africa. Preliminary application of 1D and 2D waveform modeling shows that there are strong lateral variation in the lower most mantle: some are fast (3% larger in shear wave velocity as compared to PREM); some are slow anomaly, but have geometry characterized by a long layer or a upwelling (typically 3-4% lower in S wave velocity); at the boundary between fast and slow velocity region or at the foot of the upwelling, ULVZ is probably similar in appearance to an elongated dome, a conclusion based on SKPdS waveform modeling (Appendix A) while also being verified with PKP precursor modeling.

Chapter 2 Constructing Synthetics from Deep Earth Tomographic Models

2.1 Abstract

Recent studies of deep mantle structure indicate strong heterogeneity. To conduct high resolution waveform modeling of these structures, we have developed a new method to construct 2D synthetics directly from block-style tomographic models. Unlike the WKBJ approximation which utilizes rays overshooting and undershooting receivers, our method (WKM approximation) uses rays that arrive at the receiver. First, the ray paths from the 1D layered reference model are used to localize each ray segment, where the anomalous velocities are applied by overlay, as in tomography. Next, new p_i (t_i) (p_i ray parameter, t_i travel time) are computed to satisfy Snell's law along with their numerical derivative $(\delta p/\delta t)$, which is used to construct a synthetic seismogram similar to the WKBJ method. As a demonstration of usefulness of this method, we generated WKM synthetics for the D$''$ region of high velocities beneath Central America based on Grand's tomography model. Reasonable fits to broadband data are obtained by condensing his distributed anomalies into his lowermost mantle layer which predicts synthetics containing a laterally varying Scd triplication similar to observations.

2.2 Introduction

Recent studies of lower mantle structure reveal strong heterogeneity at scales from 10 to 10,000 kilometers and velocity variations of up to 50% in extreme situations (see review, Lay et al., 1998). Long period global studies display a circum-Pacific pattern of normal velocities with embedded high velocity structures, particularly beneath eastern Asia and the Caribbean. The mid-Pacific is relatively slow, with very low velocities within specific regions(Wen and Helmberger 1998, Breger and Romanowicz 1998, Breger et al. 1998). Some of the high-velocity pockets seen in travel-time tomography are underlain by sharp features which can produce triplications. Lay and Helmberger (1983) employed several 1D S-velocity models (figure 2.1) to explain some of these observations. In these models, the thickness of D$''$ varies considerably and has been inferred to be 250 km (SLHA), 280 km (SLHO) and 320 km (SLHE). These models, though very simple, can fit about 90 percent of their data. The basis for their differences is that the triplications, as displayed in figure 2.2, vary in position between S and ScS from region to region, i.e., points b and c are not global (Wysession et al., 1998). Moreover, there is considerable variation across any particular region as shown by Weber et al. (1996), for the area beneath Asia (SLHE), and by Kendall and Nangini (1996) for the Caribbean (SLHA) region. The lateral variation associated with the triplication beneath America was noted in the initial report by Lay and Helmberger (1983) as displayed in figure 2.3. Note that FBC is located in eastern North America while EDM is in western North America (figure 2.14). Their waveforms show distinctly different interference patterns for events arriving from South America. It would be particularly useful to explain such variation from tomography-based models with some fine scale adjustments, as proposed by Sidorin et al.(1998a). They demonstrate that the above Scd triplication can be produced by a combination of a positive velocity-gradient induced by subducted material superimposed on a small global velocity discontinuity of 1%. Dynamic modeling suggests why this phenomenon is likely to be rapidly varying and 3D in nature, Sidorin et al. (1998b).

To retrieve this type of detail from seismology, we need to move beyond 1D modeling and use 3D tomographic models based on travel time analysis as a starting point. In particular, we introduce a new method of generating synthetics directly from 2D sections through these models so that local modifications can be made to explain regional features such as displayed in figure 2.3. Generating synthetics for heterogeneous earth models has a long history, in which many useful methods have been developed (Aki and Richards, 1980). For many applications, the WKBJ ap-

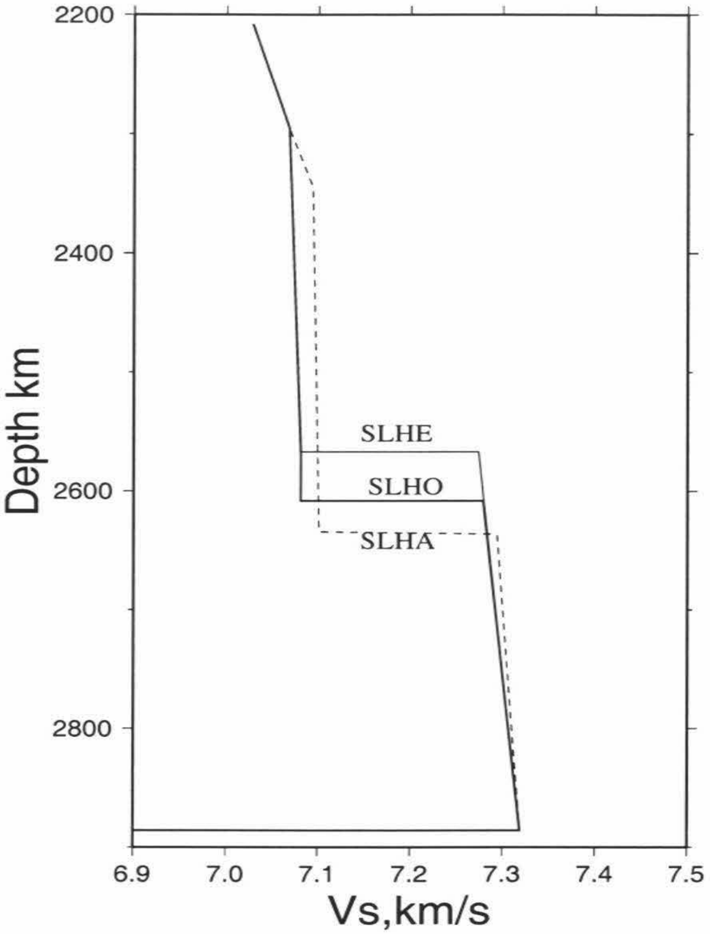

Figure 2.1: S velocity models showing regional variation of D″ thickness. SLHA denotes the model beneath central America. SLHE denotes the model beneath Asia, and SLHO denotes the model beneath Alaska. The basic feature is a 2.75 percent velocity discontinuity. After Lay and Helmberger, 1983.

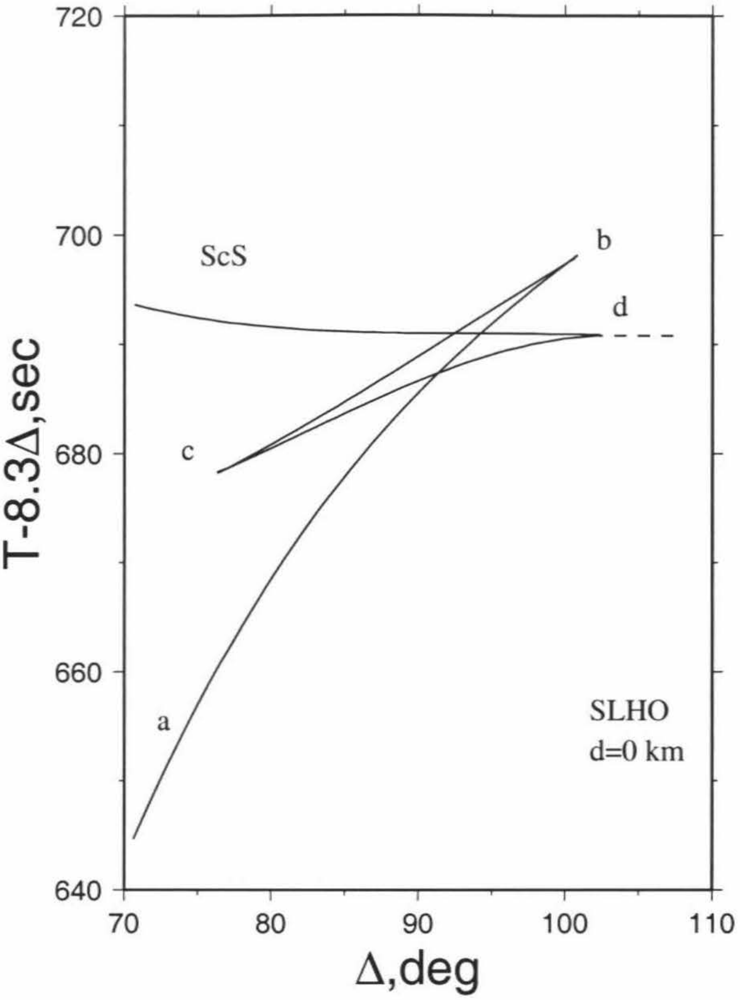

Figure 2.2: Triplication for the S phase (S_{cd}) along with ScS assuming a surface event for model SLHO. The crossover distance shifts back for deeper sources, i.e., 85° for a 600km deep source.

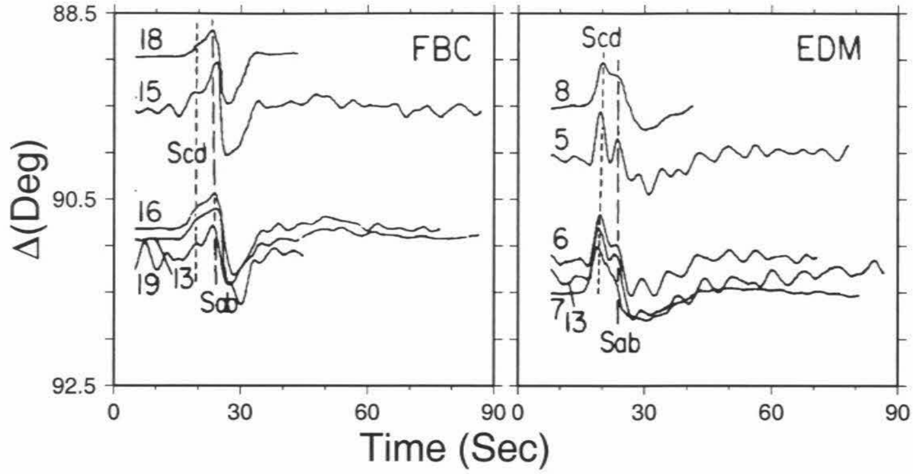

Figure 2.3: Long period SH records at FBC (Frobisher Bay, Canada) and EDM (Edminton, Canada) for some events beneath South America. The traces are aligned on the first arrival. For FBC, S_{cd} is weaker than S_{ab}, while for EDM, S_{cd} is stronger than S_{ab}. After Lay and Helmberger (1983).

proximation proves particularly appealing (Chapman, 1978). An application of the method to deep earth models is discussed by Chapman and Orcutt (1985) along with a comparison of 1D synthetics generated against those generated by the FK method. The WKBJ method has been extended to 2D by Chapman and Drummond (1982), referred to as Maslov Theory. Graves and Helmberger (1988) applied this approach to modeling multiple S phases (S, SS, ...) with some success. Liu and Tromp (1998) demonstrate that this method can produce D″ triplications from long wavelength variations if they inflate the structural contrast of the Su et al. (1994) model, but no comparison of synthetics with data was presented.

Ding and Helmberger (1997) modeled a profile of broadband Scd data from the Californian arrays, TERRAscope (Caltech) and BDSN (Berkeley Digital Seismography Network), and again found evidence for lateral variation on several scales. They presented synthetics for a possible 2D model consisting of layers with varying thickness by applying a modified Cagniard-de Hoop approach (Helmberger et al.,1996). Here we introduce an approximate solution, WKM, to a layered-block model, with constant layer thickness but varying velocity, and apply it to the Caribbean anomaly discussed above.

2.3 The WKM Approximation

We begin with a brief review of the WKBJ method and its relationship to generalized ray theory (GRT), for a 1D layered model. Figure 2.4 displays the primary difference in ray path geometry for the simple turning-ray solution in a smoothly varying material, assumed to be a layered model. The WKBJ method can be derived directly from asymptotic theory (wavefront expansion),(Chapman 1978, 1982) and is based on geometric ray paths of the type displayed in figure 2.4b. The solution is constructed from a large number of rays arriving before and beyond the receiver. These rays have ray parameter (p_i) and travel time (t_i). The wave field at the receiver can be approximated with the summation

$$\sum_i \frac{p_i - p_{i-1}}{t_i - t_{i-1}} \tag{2.1}$$

Following the GRT approach *Helmberger* [1968], we sum generalized rays connecting the source to the receiver after reflecting from each layer interface, starting and ending with the rays displayed in figure 2.4a. Chapman (1976) shows that the sum of these generalized rays can be replaced by a complex integration over depth and that this integral can be approximated by again expression (2.1). A similar solution was found by a numerical approximation of GRT synthetics *Wiggins* [1976]. The two solutions with similar expressions yield about the same synthetics, Helmberger et al. (1996), but have distinctly different ray paths. So as to avoid confusion, we will refer to methods involving the type of ray paths displayed in figure 2.4a as the WKM method. Also displayed in Fig.2.4 is a LVZ situated to demonstrate the differences in methods that can arise. WKM (top) utilizes rays arriving at the receiver, total responses are derived by summing contribution from each ray, while WKBJ (bottom) uses rays overshooting and undershooting the receivers which might potentially violate causality as discussed by Burdick and Salvado (1986). They used the earlier approach

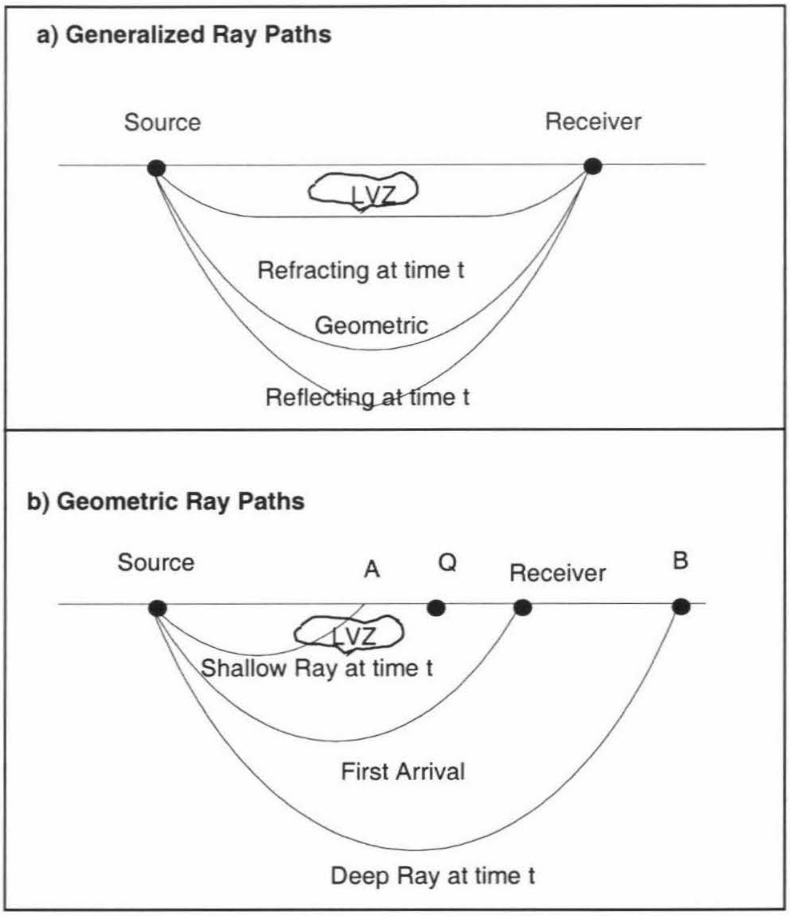

Figure 2.4: Two possible choices of ray paths for slowness calculations involving generalized ray paths and geometric ray paths. The generalized paths in (a) define a different envelope of causality than the geometric paths displayed in (b). In (a) the rays are generalized rays, each ray is reflected from each layer interface. The rays above the geometric one carry refracted energy, while the rays below the geometric one carry reflected energy. All the rays connect the source and receiver, WKM integrates the contribution of each ray to produce synthetics (see figure 2.6 for details). In (b) the rays are geometric rays; these rays overshoot or undershoot the receiver. WKBJ method integrates all the contributions of these geometric rays to produce synthetics. The two sets of rays interact with perturbations in very different ways. After Burdick and Salvado, 1986.

Chapman [1976], in their development of a 3D slowness method.

Because WKBJ can be directly derived from classical optic theory, it proves relatively easy to treat 3D problems for smoothly varying media (Liu and Tromp, 1996). Sharp boundaries cause difficulties following this approach where GRT has some advantages. Energy trapping caused by locally dipping structure provides a good example where comparisons of GRT solution with finite-difference methods prove GRT quite favorable *Vidale and Helmberger* [1988]. Unfortunately, such solutions involve dealing with spatially dependent ray parameters and their attendant problems *Frazer and Phinney* [1980]. A simple example of locally dipping interfaces and how they have been treated is displayed in figure 2.5 *Hong and Helmberger* [1988]. The relationship between t_i and local ray-parameter p_i becomes

$$t = p_i d_i + h_i(\frac{1}{\beta_i^2} - p_i^2)^{\frac{1}{2}} \tag{2.2}$$

with β_i the shear velocity and d_i and h_i defined in the figure 2.5. Changes in the ray parameter p caused by the dipping interfaces are embedded in p_i. Applying this procedure to a large number of layers is obviously cumbersome in the same way as computing synthetics in spherical shells *Gilbert and Helmberger* [1972]. In this case, the solution was simplified by adjusting the velocities to correct for changes in the relative slopes of interfaces which leads to earth flattening.

Following this approach, Helmberger et al. (1996) introduced the local stretching approximation to 2D structures which maps d_i, β_i, and h_i from figure 2.5 into d_i', β_i', h_i' where $p_i = p$ is constant along a ray path. Thus, the ray path displayed in figure 2.5 maps the dipping structures into a flat-layered model with d_i's lying along the interfaces and h_i's at right angles. Note that if the ray was reflected back through the layers, these parameters would take on different values. The accuracy of this approach is demonstrated in the above study by comparing synthetics against finite-difference methods. A 2D profile of synthetics generated with this code was presented in Ding and Helmberger (1997). Synthetics generated from such a parameterization has a natural relationship with block-style tomography models. Following the tomographic

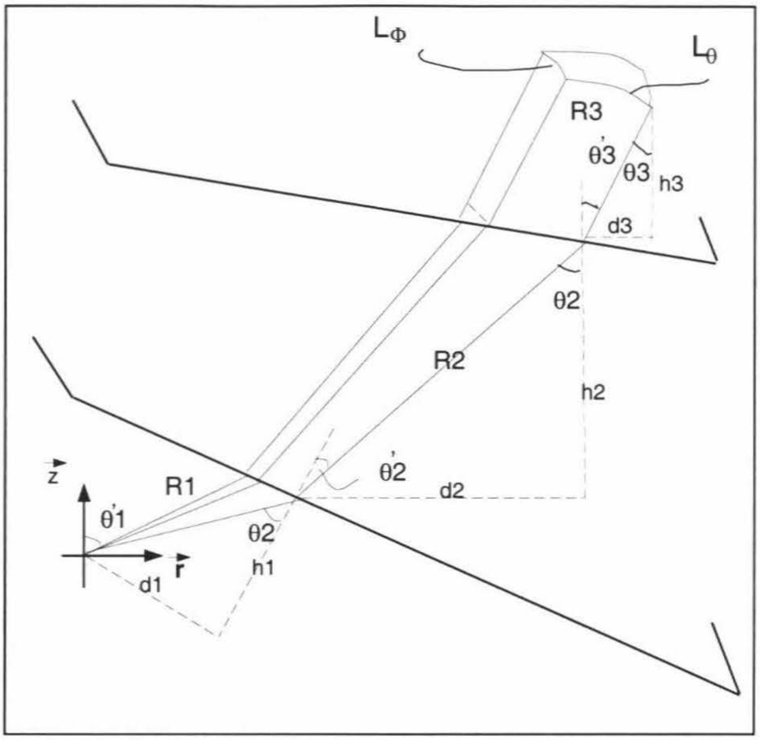

Figure 2.5: Diagram displaying geometrical spreading for locally dipping interfaces. The parameterization used in generating GRT synthetics is indicated in terms of d_i, and h_i, after Hong and Helmberger (1978).

approximation, we find d_i, h_i, β_i for the 1D reference model, we overlay a new velocity structure and obtain d_i, β'_i, h_i which freezes the path but will change the time. This scheme is used in most tomography studies which will be referred to as the time-corrected approach. A better approximation is to overlay the velocities and recompute the path d'_i, β'_i. Thus more accurate responses may be achieved. We call this approximation path corrected. Figure 6 displays such paths for an earth-flattened model containing a fast block in D$''$.

Although this approach appears simple, the treatment of the vertical block boundaries needs to be addressed, in particular, the way we handle the ray bending that occurs when a ray crosses into a neighboring block within a layer. In figure 2.6a the velocity β'_i is assigned when a crossing from interface (i-1) into (i) and remains so until encountering interface (i+1), essentially no correction at vertical boundaries in each layer. In figure 2.6b, the rays are bent to correct for wall-crossing. Ray paths for B satisfies reciprocity while those in case A do not. A blow-up of the ray paths is displayed in figure 2.6c showing the slight adjustment in path when leaving the fast block. To determine those paths involves iteratively recomputing ray parameter p so that the ray arrives at the receiver; in particular the ray satisfies Snell's law on all velocity boundaries, both horizontal and vertical. The drawback of this exact ray tracing method when applied to tomographic models is that the ray will not always arrive at the receiver because of the existence of the corners of blocks in tomographic models. The travel time vs. ray parameter plots (t_i:p_i) with these various approximations are displayed in figure 2.7a and b, for a distance of 82°. The PREM model (1D) produces a smooth minimum which yields a simple square-root singularity for (dp/dt) as expected for a geometric arrival (Chapman, 1978). The time corrected or tomographic approximation yields a slight secondary inflection while the path-corrected approximation (case A in figure 2.6) produces a true secondary arrival or triplication as can be seen in figure 2.8 . The (t_i:p_i) curves for a comparison of the two ray-tracing approaches discussed in figure 2.6 are given in figure 2.7b. The two methods yield a small shift between S and the triplication, but with similar amplitudes. This particular example was computed assuming layer thickness of 20km which produces about

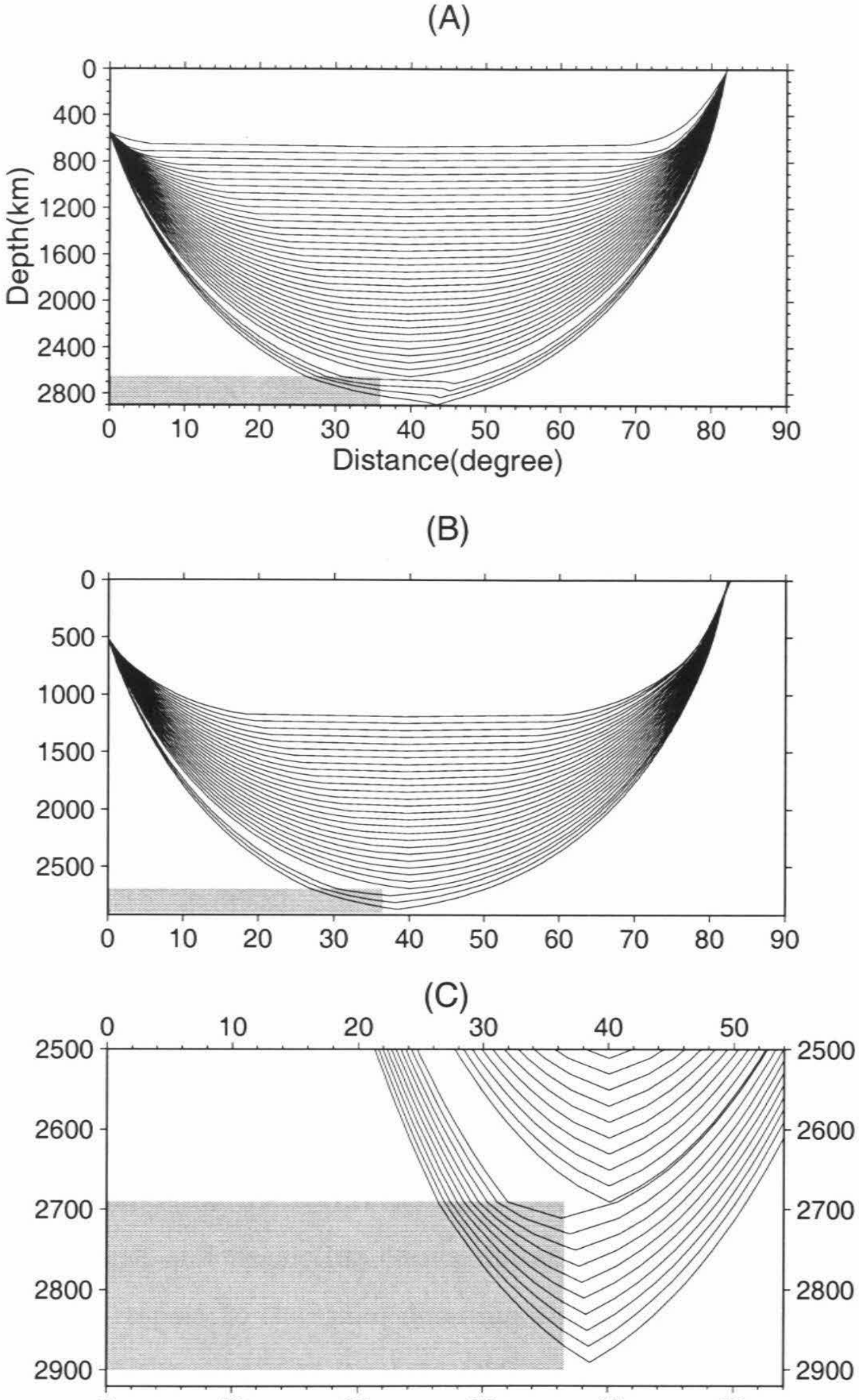

Figure 2.6: Ray paths connecting the various interfaces to the source and receivers at a distance of 82 °. The shaded zone represents a 4% increase in velocity relative to PREM where the anomaly extends from 0°to 36°. Plot (A) displays these paths where the ray path does not bend when crossing the walls of the box have been neglected. Plot (B) includes such bending while plot (C) displays a blow-up of the anomalous region where the bending is more obvious.

a quarter of a second offset in synthetics as shown in figure 2.7c. Decreasing layer thickness reduces this offset, but this level of accuracy is equally effected by the choice of fitting a smooth curve through the discrete (t_i:p_i) points needed in performing the derivative (dp/dt). While a number of useful approximations are available (Chapman, 1978), we found the generalized cross validation (GCV) method *Wahba* [1990] to be particularly effective. Basically the GCV method minimizes simultaneously the integral of the square of second derivative of the data and the variation between the data and the smoothed curve. Choosing cubic splines as basis function f(x), one can show that for a set of discrete data (x_i,y_i), $f_\lambda^{[k]}(x)$ minimizes

$$\frac{1}{n}\sum_{i\neq k}^{n}(y_i - f^{[k]}\lambda(x_i))^2 + \lambda\int_{x_0}^{x_n}(f''(x))^2dx \tag{2.3}$$

and the λ is obtained by minimizing:

$$V_0(\lambda) = \frac{1}{n}\sum_{k=1}^{b}(y_k - f_\lambda^{[k]}(x_k))^2 W_{kk} \tag{2.4}$$

where W_{kk} is the weight for each data point which is estimated automatically. For details, see Wahba (1990).

In summary, the distinction between the paths for approach A and B of figure 2.6 goes away as the layer thickness is decreased and neglecting ray bending at vertical boundaries circumvents the corner problem. Moreover, we do not expect such structures in the earth and neglecting corner-diffractions is probably a reasonable approximation with respect to the usual determinations of tomographic models. In short, we will assume the simplified local stretching approximation where every ray path is obtained from a specific homogeneous layered velocity structure and can be easily determined.

The response for each of these rays can be generated following the GRT approach or we can obtain a useful WKM approximation, applying equation (1)(Chapman 1976). The three sets of synthetics corresponding to the reference model and to

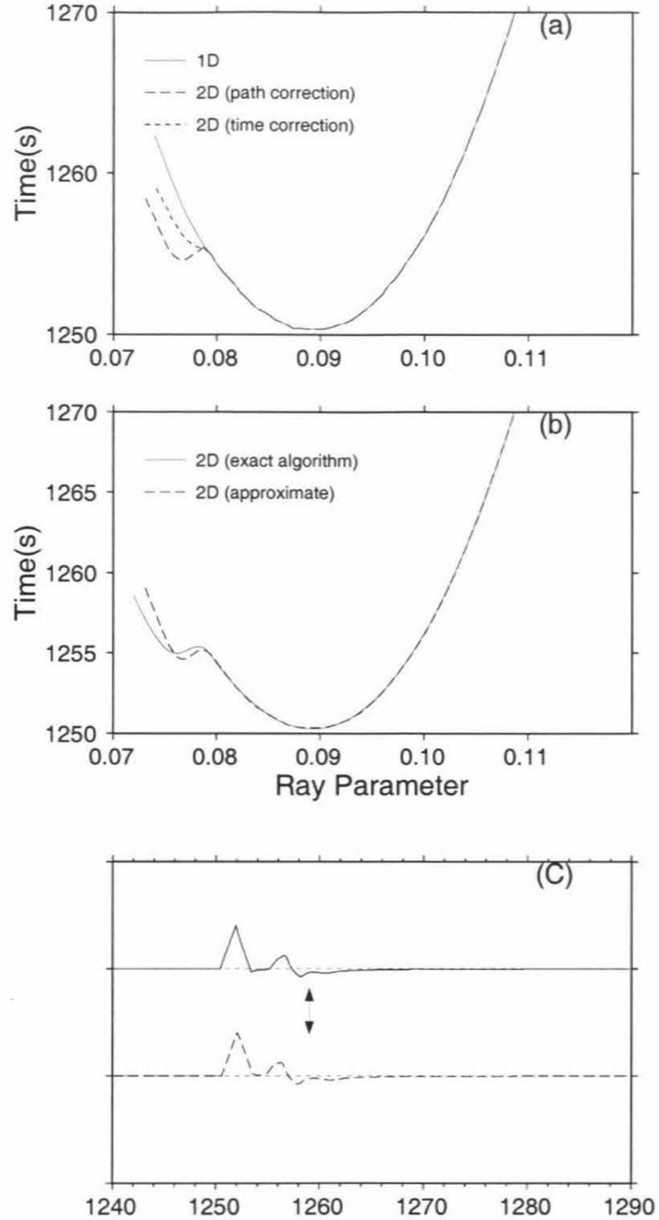

Figure 2.7: (a)p-t curves for the three approximations for a distance of 82 degrees. The solid curve is for the 1D reference model (PREM). The dashed line is for path corrected approximation where the faster zone flattens ray paths causing a triplication, while 2D time correction does not produce extra phases. (b) Approximate path correction vs. exact path correction. The dashed curve is an approximate path-corrected p-t curve, the solid curve is the p-t curve for exact path correction which is achieved by ray-tracing to every interface by applying snells law. The approximate path correction is achieved by local stretching algorithm assuming constant layer velocity with no bending. (c) The synthetics based on the approximate path correction (dashed line) and exact path correction (solid) respectively. The arrows indicate the beginning of truncation phase due to the existence of the CMB. The two seismograms show a very similar S_{cd} phase.

the two approximations are shown in figure 2.8 following the latter method. The ScS phase is shifted ahead about the same amount in both approximations relative to the PREM synthetics since the ScS path correction is less severe than for Scd. The absence of the Scd phase in time-corrected synthetics shows the necessity of performing the path corrections. Doubling the number of layers produces about the same synthetics which is a good test of the procedure.

2.4 Application

Most tomographic models display relatively high-velocities beneath Central America including the inversion by Grand (1994) which we will use for demonstrative purposes figure 2.9. This model displays a strong structural gradient beneath the Caribbean. While the paths towards Newfoundland shows nearly a PREM-like structure, the western paths cross major fast velocity structures. This feature appears to be compatible with the observation of Kendall and Nangini (1996) who argued for strong variations in S_{cd} beneath the Caribbean, being strong towards the west and weak toward the east. However, Grand's model has a relatively smooth vertical D$''$ structure since this tomography model does not contain information about the Scd phase. This can be seen in the 2D cross section as displayed in figure 2.9d connecting Argentina to California. Synthetic predictions from this section are given in figure 2.10a with no noticeable Scd phase. A modification is displayed in figure 2.9e, where we follow Grand's (1998) suggestion of enhancing the anomalies in the bottom most layer with a factor of 3 while compensating in overlying layers. These modifications of tomography models is quite similar to the approach used to study travel time and waveform anomalies (Ni et al., 1999) and has proven to be quite useful. This change artificially produces a triplication (S_{cd}) while roughly conserving the travel time variations in S and its multiples, ScS and SKS, which are used in the original tomographic model. Clearly, such a mapping is rather arbitrary and we will simply use it as one possible idealization and make synthetic predictions along various profiles. Note that these tomographic images are, by their nature, rough, and some smoothing procedure should

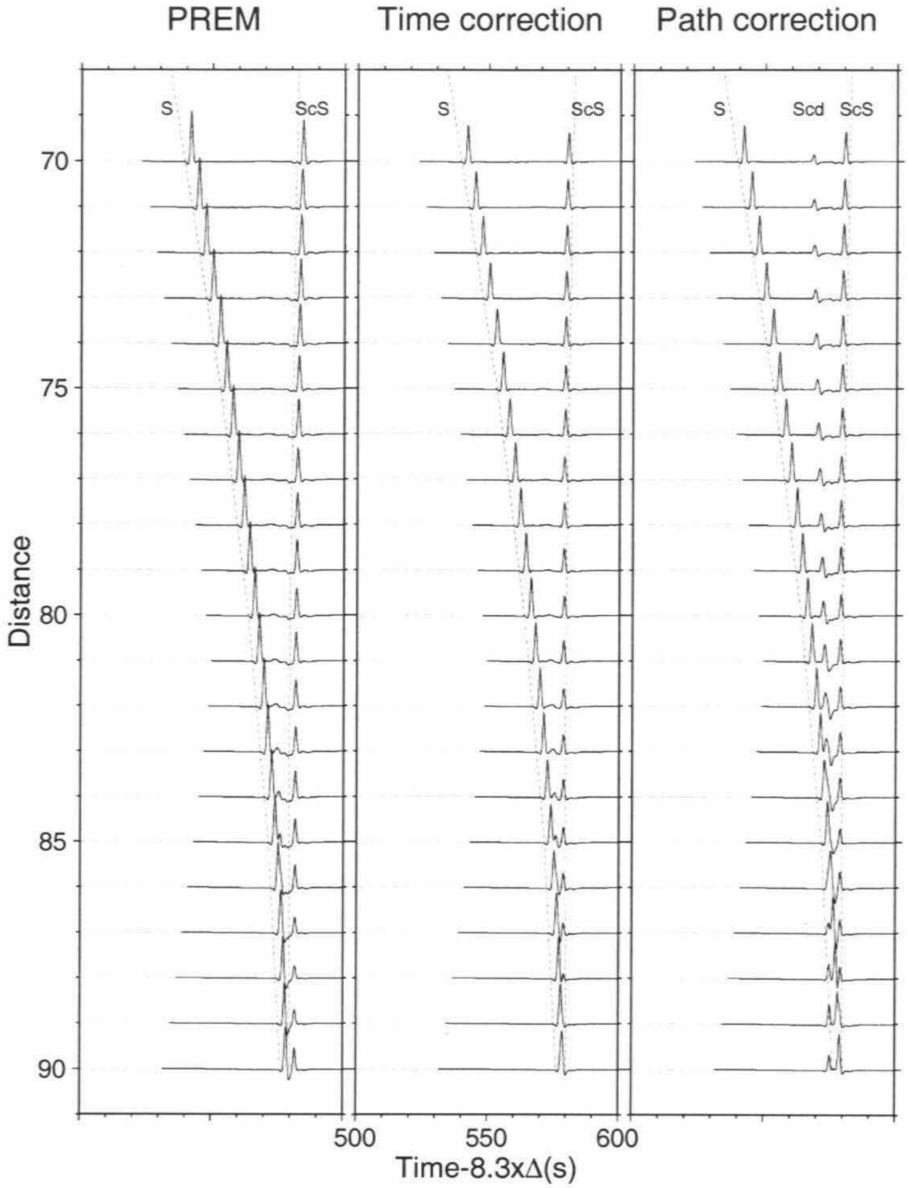

Figure 2.8: Synthetic record sections for 1D, 2D time corrected, 2D path corrected. Travel time is in reduced form. Note that the 2D time correction synthetics do not show the S_{cd} phase while the 2D path correction synthetics do.

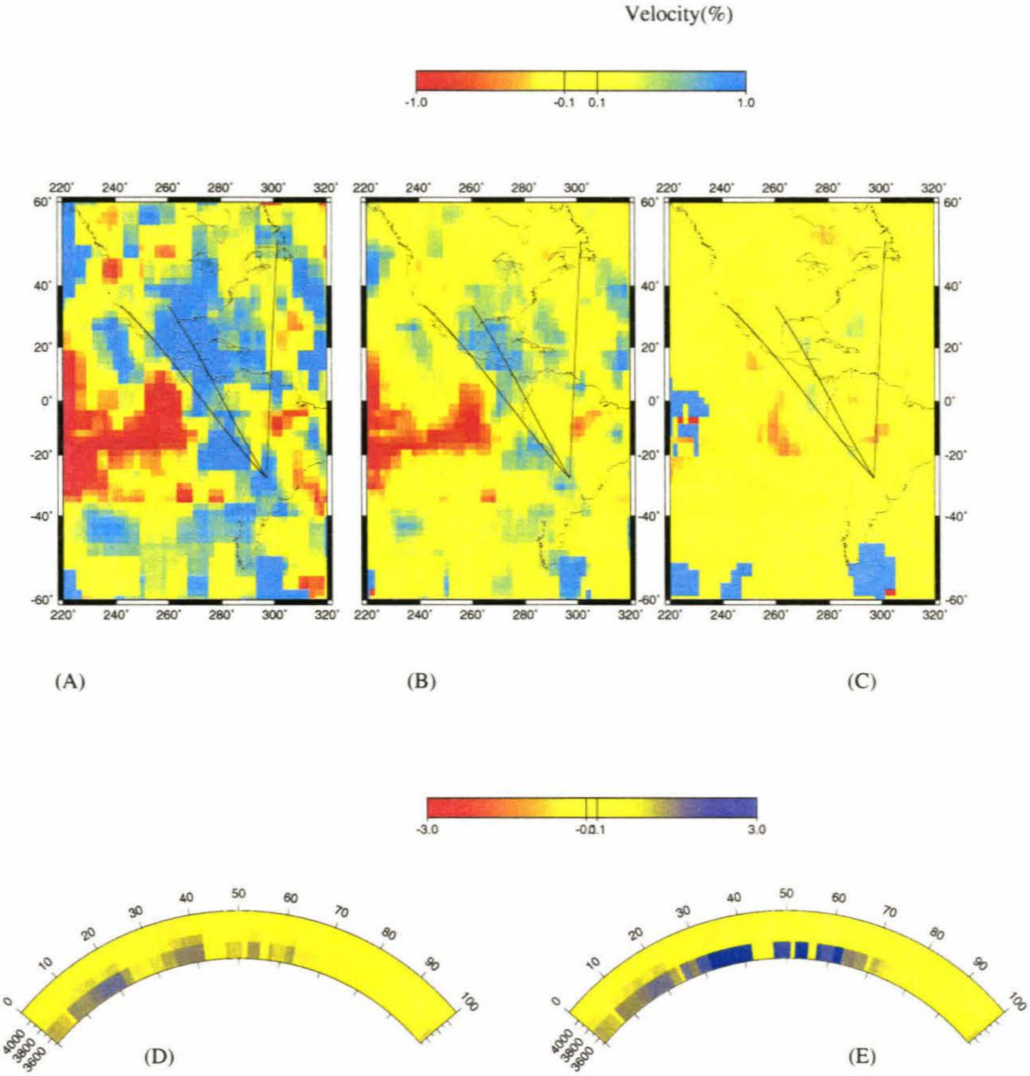

Figure 2.9: Horizontal slices of Grand's tomographic velocity model at three depths displaying the Caribbean anomaly; (a) the depth between 2890(CMB)-2650km. (b) the depth between 2650-2500km. (c) the depth between 2500-2350km. The three lines indicate azimuth samples of the structure for an event located in Argentine (05/10/1994). The left line marks the western margin of the fast zone, the middle line marks the most anomalous portion. Note that the western region beneath the Caribbean is relatively faster than the eastern region which is marked line on the right. (d) Grand's Model. (e) Enhanced Grand's Model, as described in the text.

probably be applied, but at this stage of exploratory waveform imaging we will simply use them directly, although, by omitting "corners", we have de facto smoothed.

As discussed earlier, D$''$ appears to contain a broad range of structures on different scales. Thus, for our first numerical experiment we will revisit the broadband California data studied by Ding and Helmberger (1997). A selection of data showing the S_{cd} phase is displayed in figure 2.11, along with synthetics from a 1D subducted slab model proposed by Sidorin et al. (1998a). Their particular model contains a double thermal boundary layer, one at the CMB (negative gradient) and the other approaching a 1% velocity jump (positive gradient) a couple of hundred km above CMB. Synthetics for the enhanced model clearly show S_{cd} phases (Figure 2.11c). Though 1D synthetics fit the travel times well, the amplitudes of the S_{cd} phases are too strong as compared with observed data at some stations, e.g., PAS. The 2D synthetics fit the relative amplitude of S_{cd} to S at some stations, but do not fit the timing separation between S and ScS as well as the 1D model. This feature is easily accommodated by adding a low-velocity boundary layer approaching the CMB, as in Sidorin et al.(1998a). Perhaps a more interesting feature displayed by this observed record section is the rapid variation associated with S_{cd}. Note that S_{cd} appears early and strong at NEE while relatively weak and late at BAR; the pattern changes for different events (Ding and Helmberger, 1997). We could alter the 2D structure to increase the amplitude of S_{cd} and make it more variable, but to be meaningful would require extensive data analysis. This will be possible with the extended broadband network installation now in progress (Jones et al., 1999).

Two synthetic record sections along the paths to FBC and EDM are displayed in figure 2.12. As expected, the FBC synthetics show a weak S_{cd} relative to S_{ab} since the structure is approaching PREM. These predictions can be compared with the observations displayed earlier in figure 2.3. While these predictions do not overlay the observed waveforms exactly, they do compare quite well at the range of 89°(figure 2.13). Note that the strong shoulder indicated by the second arrow in EDM (LP) matches the data. In contrast, the second arrival (S_{ab}) appears stronger in the FBC (LP) synthetics which agrees with the data. Lay and Helmberger (1983) also displayed

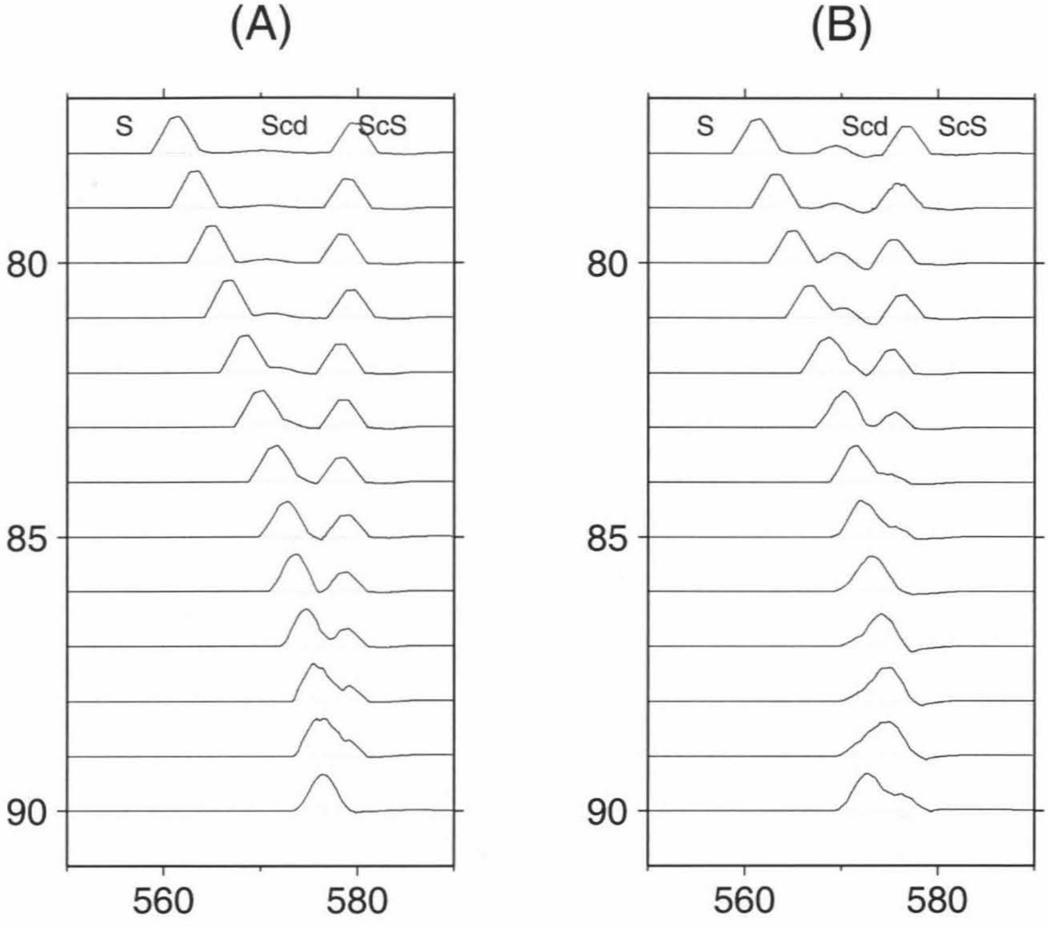

Figure 2.10: 2D synthetics for Grand's model (a) and enhanced model (b). Before enhancement, Grand's model does not produce an appreciable S_{cd} phase, while the enhanced model does.

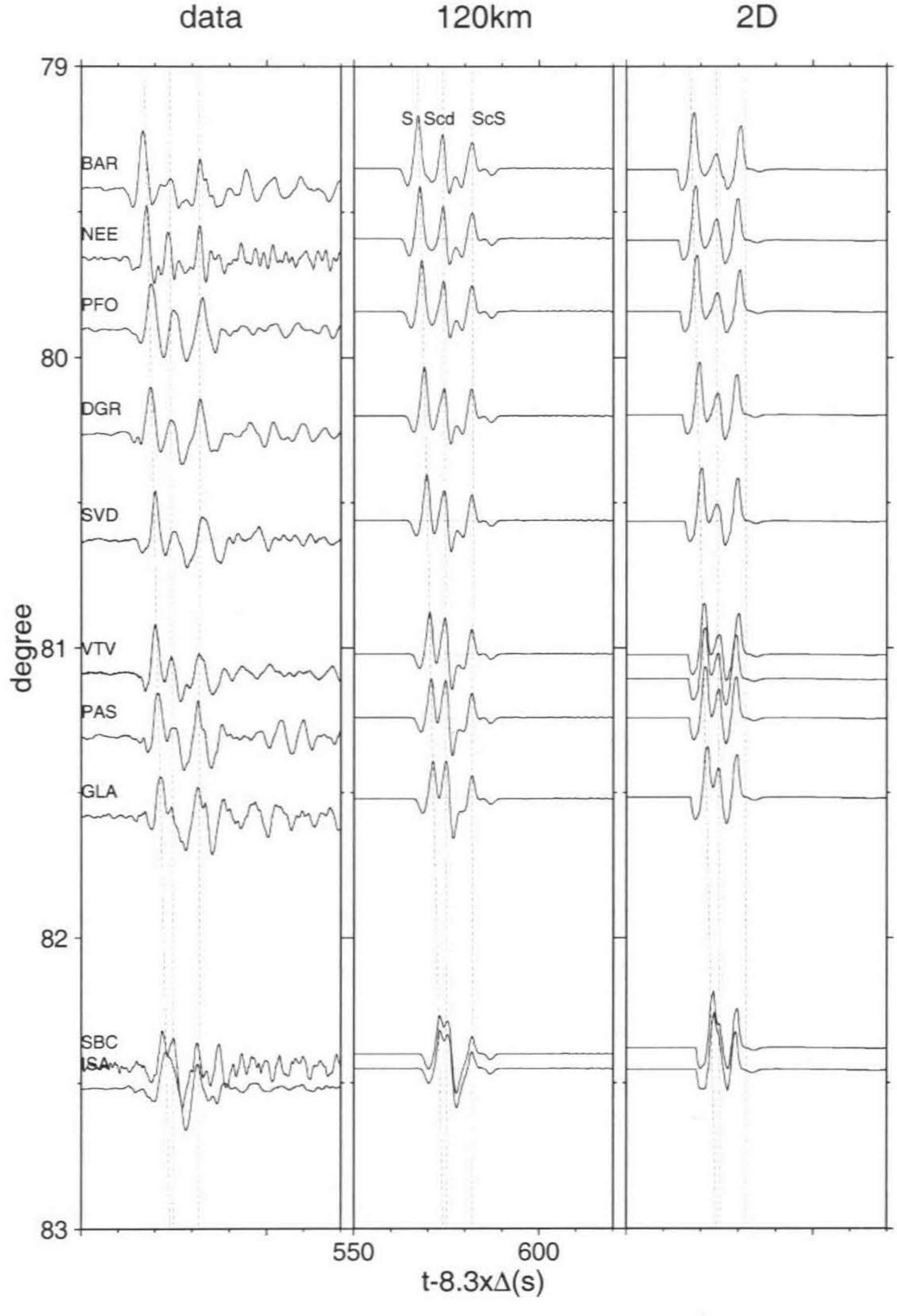

Figure 2.11: Comparison of waveform data with 1D synthetics and 2D synthetics. The data (SH) are recorded by TERRAscope stations for the Argentine event (05/10/94) (Ding and Helmberger 1997). 1D synthetics assumes a 1D model with 120 km transitional zone 280 km above CMB; see Sidorin et al.(1998a). 2D synthetics are based on the enhanced model in figure 2.9e.

short-period observations at those ranges where EDM data clearly show two arrivals similar to those in our synthetics. Thus, even though these waveform features appear subdued, they are probably observable, especially at distances greater than 90° with the new broadband data currently available and new classes of D″ models recently introduced.

An overlay of the synthetics generated along the azimuths to the EDM and FBC shows some interesting time shifts. At the smallest ranges, the FBC records arrive about 6 seconds earlier than at EDM as expected from the contrast in upper mantle structure (Grand and Helmberger, 1984). However, at the largest ranges, they have nearly the same arrival times because of the fast D″ structure along the EDM azimuth which essentially compensates for the upper mantle delay. The cross-over distance shifts to smaller ranges for this reason. In the lower panel of figure 2.14, a contour map indicating the position of cross-over (heavy line) is displayed along with timing lines. These curves indicate the separation between the two arrivals, S_{ab} versus S_{cd}, as displayed in figure 2.2. Mapping cross-over distance has the advantage of excluding the upper mantle effects, since S_{cd} ray paths and S_{ab} ray paths are very close together in the upper mantle. If the lower mantle velocity structure is 1D, the cross-over distance should be equal along different azimuths. Thus, the deviation of crossover contours from a circle implies lateral variation in the lower mantle velocity structure which is easily observable with the deviation of about about 1° in this case. The pattern changes most rapidly along the eastern edge of the Grand's Caribbean anomaly as displayed.

The upper portion of figure 2.14 displays a cross section across the North America continent roughly along the cross-over contour. The triangles indicate the azimuth appropriate to EDM and FBC with the event in South America. Thus the path passing through the upper mantle to EDM is clearly tectonic (TNA) relative to FBC (SNA). The bars indicate travel time steps in intervals of 0.5 second which are appropriate for the upper mantle contribution to travel times along the cross-over lines. The relative changes between S_{ab} and S_{cd} for the whole paths are considerably less because of the compensating effects discussed earlier.

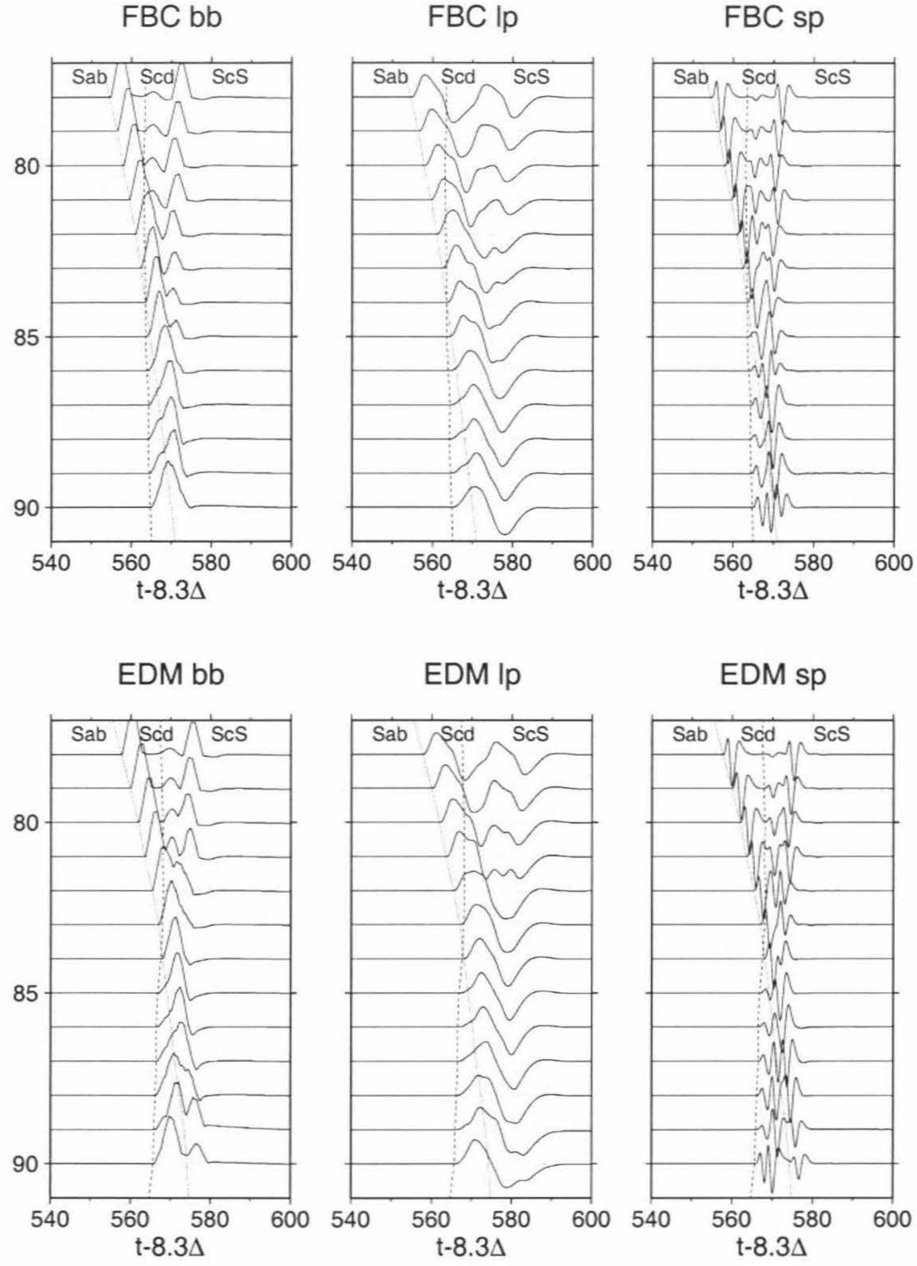

Figure 2.12: Synthetic profile along azimuths to FBC (TOP) and EDM (BOTTOM). The left, middle, and right panels are synthetics of broadband, WWSSN long period, WWSSN short period respectively; the latter are for comparison with observation given in Lay and Helmberger (1983). On the broadband synthetics, FBC shows a weak S_{cd} phase while EDM shows a strong S_{cd} phase relative to S_{ab}. Arrows mark the peaks of S_{cd} and S_{ab} on the long period synthetics.

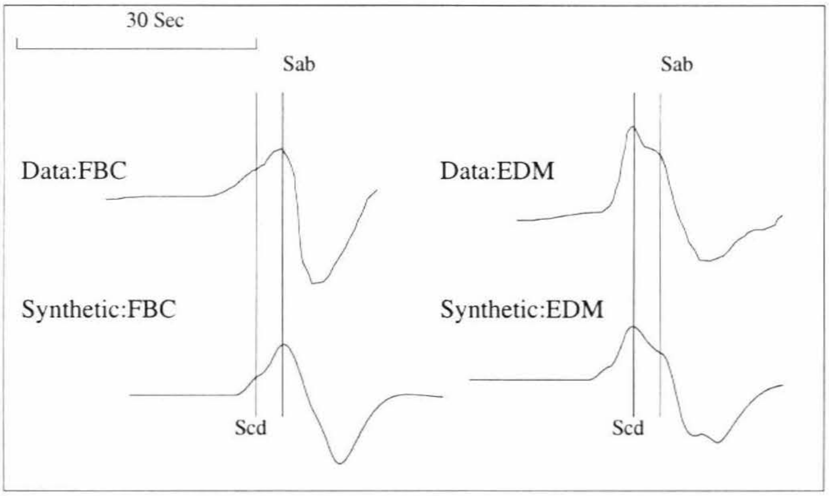

Figure 2.13: Data and synthetics for Station EDM and FBC respectively. The data (top row) is for event 18 from Lay and Helmberger (1983), (c.f. fig 2.3) . The synthetics are those marked by arrows in fig 2.12 .

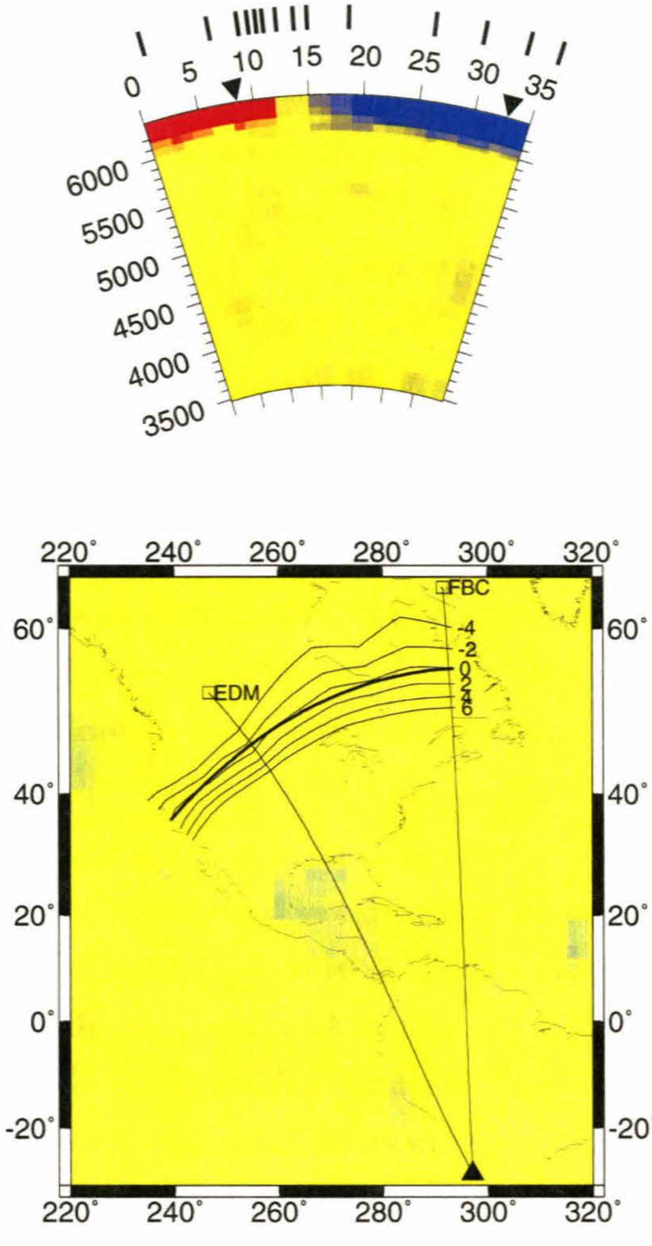

Figure 2.14: (a) Travel-time of S$_{ab}$ obtained from 2D synthetics along various azimuths. The velocity structure is from Grand's modified model, the cross section is defined by the 1D crossover contour (the bold line in bottom panel) starting from the western edge. The bars above the velocity profile display the variation of travel time, and each bar marks the point where S_{ab} is 0.5 earlier than its western neighbor. Dense bar spacing indicates a strong transverse velocity gradient, thus stronger 3D effects. (b) Equi-differential time contours where the differential is $S_{ab} - S_{cd}$. The numbers -4, -2,0,2,4,6 are the differential time in seconds. The background is the velocity profile of the basal layer near the CMB from Grand's model.

2.5 Discussion and Conclusion

The 2D synthetics predicted from a modified Grand's model show amplitude variation and differential travel time variations, common to S_{cd} modeling attempts. However, as discussed in the introduction, the lower mantle is 3D. This questions the validity of 2D modeling. If the velocity gradients are small enough, or, if the velocity does not vary more than a few percent in one wavelength, 2D modeling should be adequate. There are some post priori criteria to test the validity of 2D modeling. If the 2D synthetics do not change much for a small change in azimuth, it appears that the 2D modeling is applicable. An example of this situation can be seen in figure 2.14, where the bar spacing indicates rapid travel time variation laterally. Dense bars imply strong variation and while the transition from TNA to SNA is interesting, studying deep earth structure near this transition boundary is probably risky. In short, the earth is 3D, but 2D sections judiciously chosen should prove useful in mapping out these structures.

Another limitation of our method occurs when the structures have sharp features. For example, in the study of TERRAscope data, we can begin to see rapid variations in the timing and shapes of S_{cd}. TRINET (Jones et al., 1999) is increasing station density tenfold, which will undoubtedly provide such data as well as the many PASCAL experiments either existing or planned. Sharp features in the presence of strong velocity contrasts will, indeed, produce diffraction effects which are not handled with this approximation. But since the waveform solution can be decomposed into individual rays (dp_i/dt_i), they can be shifted and reassembled to simulate neighboring models as in Song and Helmberger (1998). The inverse problem can be effectively addressed and structures defined. Complete wave fields from such structures can be produced by more sophisticated codes such as discussed in Wen and Helmberger (1998).

In conclusion, we developed a useful method of constructing 2D synthetics for tomography models. The method is related to a modification of WKBJ, thus the name WKM. However, it is basically a first-motion approximation of generalized ray theory and compatible with Cagniard-de Hoop methods. This feature makes it attractive for studying structures with large velocity jumps near the CMB, and shadow-zone boundaries. An application of the method to Grand's tomography model proved quite successful in explaining some of the S_{cd} behavior observed for the D'' structure beneath central America.

Chapter 3 Application of WKM to Low Velocity Structure Beneath Africa

3.1 Abstract

Seismic waveforms observed in South Africa containing the first arrival crossover of S to SKS (70° to 110°) are analyzed. The data consist of analog records from the World Wide Seismographic Station Network (WWSSN) of deep events beneath South America. The S-waves arrive 2 to 3 sec early relative to PREM at ranges from 70° to 95° and then become increasingly delayed, becoming 5 to 6 sec late at 110°. The SKS phase is late by 3 to 5 secs over the entire range. This pushes crossover between S and SKS, normally observed at about 81°, out about 2° to 3°, which is the most anomalous shift ever reported. To model such features, we modified Grand's tomography model [*Grand*, 1994], and generated 2D synthetics to match the data. The overall shape and position of the lower mantle low-velocity anomaly proposed by Grand predicts good results if lower mantle anomalies are enhanced to a level of about 4%. This results in a complex tabular structure extending upward from the core-mantle boundary about 1500 km into the mantle. These features appear to be consistent with a large young plume which is erupting off the CMB.

3.2 Introduction

The core-mantle boundary and adjacent transition zones play a critical role in Earth dynamics. Lateral variation in this structure provides some fundamental constraints on lower mantle dynamics. There have been a variety of studies on the seismic structure of the lower mantle at various wavelengths [*Loper and Lay*, 1995]. The 3D seismic tomographic model [*Grand*, 1994] appears to have the highest S-velocity resolution, roughly a few hundred km for some well-sampled regions. This model was constructed by picking the travel-times of multiple S phases along with core phases, S_cS and SKS, as recorded on analog records. These data are unique and not used by any other modeling group. In contrast, most global models have been constructed by inverting long-period waveforms as recorded on the Global Digital Seismic Network (GDSN) or by constructing tomographic models from compiled travel time observations and, thus, share the same data. While these methods vary somewhat, they produce similar models near the surface but disagree significantly for the lower mantle and near the core-mantle boundary (CMB). Structures above a depth of 2500 km agree remarkably well with P-velocity tomography [*van der Hilst et al.*, 1997; *Grand et al.*, 1997]. The agreement degenerates below this level.

To check the lower structure displayed in these models in regions containing rapid variation, we can examine some key profiles of data to see how well synthetics constructed from these models predict the waveform observations. The most anomalous lower mantle structure in Grand's global model occurs beneath Africa as displayed in figure 3.1. It shows that most of the region beneath Southern Africa and the Southeastern Atlantic is very slow, typically up to several percent. This feature is also seen in the long-period tomography studies [*Li and Romanowicz*, 1996; *Masters et al.*, 1996; *Liu and Dziewonski*, 1994], as discussed in *Ritsema et al.* [1998a]. Large travel-time delays of up to 5 sec for shear waves that traverse the lower mantle in this region are well predicted by Grand's model. However, the limited number of stations used in his tomography study does not allow good resolution and results in streaking, as discussed by [*Ritsema et al.*, 1998a]. This feature tends to reduce the concentrated velocity structures. A 2D cross section of Grand's model from South America to South Africa is presented in figure 3.2a. A modification (ALVS) displayed in figure 3.2b produces synthetics matching the waveform data and travel-time differentials (SKS-S) obtained along this azimuth. The objective of this forward modeling study is to validate this modification found by trial and error.

The analysis starts with a set of numerical seismograms generated from these two models along with reference models to establish the waveform features that are the

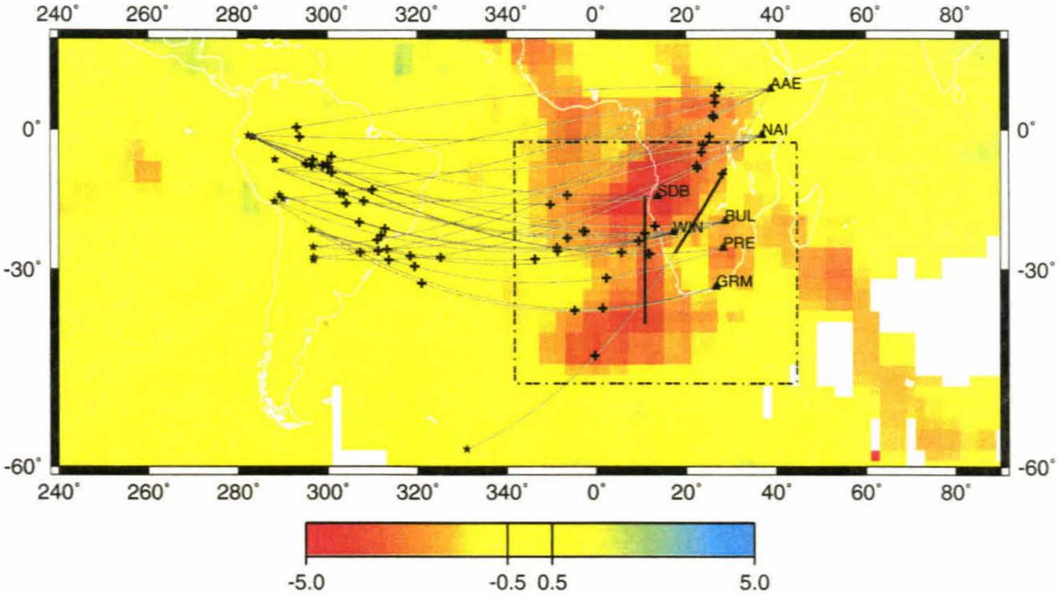

Figure 3.1: Map displaying locations of deep South American events and African WWSSN stations recording these events. Their respective SKS ray paths containing core-mantle piercing points (crosses) is overlaying Grand's lowermost mantle shear velocity tomographic model [*Grand*, 1994]. A heavy line denotes the 2D (depth ~ 1500 km) section presented by *Ritsema et al.* [1998a]. The vertical bar displays roughly the region sampled in this study assumed to be 2D, that is independent of latitude. The rectangle indicates the boundary for the velocity modifications made in this study.

most diagnostic. This is followed by a detailed discussion of the complexity of the data set including short-period data and phase picking. A comparison of observed travel-times with synthetic predictions is given in conjunction with direct comparisons of waveforms near the crossover range (81°) expected for deep events.

3.3 Analysis

One of the strongest constraints on lower mantle structure is provided by the behavior of S and SKS as a function of crossover distance [*Schweitzer and Muller*, 1986; *Garnero et al.*, 1988]. This feature is amplified in 2D structures where CMB ray crossing becomes particularly important on the timing of SKS where SKS can avoid anomalies seen by (figure 3.1). While the tomographic approximation gives reasonably accurate results in many situations involving small percentage anomalies, correcting paths to

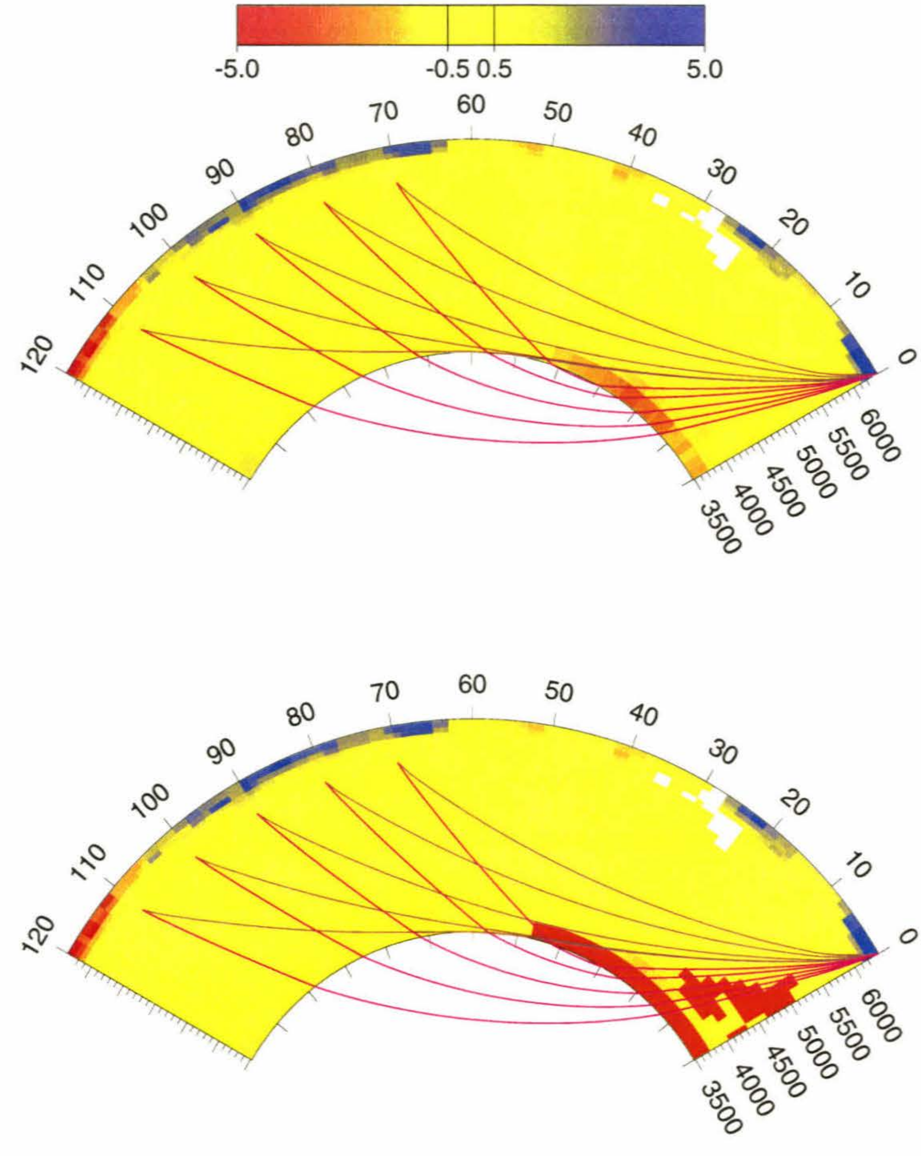

Figure 3.2: Upper panel displays a 2D cross-section from station BUL through South America (passing through Lat. = 2 S, Lon. = 77 W). Ray paths for S (brown) and SKS (rose) sampling Grand's model are presented. The lower panel displays a modified model (ALVS) derived in this study with increased lower mantle anomalies discussed in the text. Note the ray path sampling of the low-velocity structure by SKS relative to S.

satisfy Snell's law yield more accurate synthetics [*Ni et al.*, 2000]. Some examples of these 2D synthetics generated by this new method called WKM are given in figure 3.3. These synthetics are based on the 1D reference model, PREM, a 2D section of Grand's model as displayed in figure 3.2a and some modified models derived in this study. The principal phases are S, SKS, and S_cS at the top, which evolve into SKS, SKKS, and S_{diff} at the bottom. The latter is formed by the interference of S and S_cS as these two phases come together asymptotically. This feature starts near 93° for PREM (shadow boundary) but is shifted to larger ranges for models containing slow D'' regions. Note the delayed S_cS which allows this feature to develop and since S_cS approaches S very slowly, it can persist to rather large ranges. A slow basal layer (SBL) will suffice for this feature as displayed in the third column of figure 3.3. The biggest difference between these synthetics occurs near the crossover as indicated by the bars. This is caused by the upgoing, near vertical segment of SKS, which is strongly influenced by the upward enhanced slow structure (figure 3.2). In summary, the most characteristic feature of a radially extended upward low velocity zone is a shift in crossover, and a reduced separation between SKS and S. Unfortunately, these idealized features are not that easy to see in observations from the sparse station coverage presently available.

3.3.1 (a) Data

Long-period (LP) and short-period (SP) observations from deep focus South American events recorded in Southern Africa by the WWSSN were used to construct record sections such as displayed in figure 3.3 used in modeling. These LP records have been digitized and rotated to obtain the SV and SH motions and presented in figure 3.4. Table 3.1 lists the events used and figure 3.1 displays the paths to the various stations. These records have been aligned on SKS as a straight line showing the S phase crossing quite clearly. Small shifts in distances have been added to correct for depth effects [*Garnero and Helmberger*, 1998a]. The radiation patterns for the events tend

Table 3.1: South American events list

No.	origin	lat(°)	lon(°)	depth(km)
1	650917 11:13:53.5	-1.4	-77.7	161
2	651103 1:39:3.20	-9.04	-71.32	587
3	670117 1:7:54.3	-27.4	-63.3	586
4	670909 10:6:44.5	-27.62	-63.15	577
5	671227 8:53:51.4	-21.2	-68.3	135
6	680823 22:36:49.8	-22	-63.64	513
7	690725 6:6:42.1	-25.49	-63.21	573
8	700617 4:44:20.9	-16	-71.88	99
9	720112 9:59:10.3	-6.83	-71.77	575
10	731025 14:8:58.5	-21.96	-63.65	517
11	790521 22:22:23.0	-15.44	-70.04	209
12	831212 12:21:12:0	-28.13	-63.15	602

to be SV-rich with a fairly constant polarity across the section. The SH is less clear but has been included at the larger ranges. The gray zone indicates the normal range of signal reversal, where the first arrival becomes SKS. Note that the data do not reverse until nearly 84°. This should be compared with these same events as recorded in North America where a clear crossover occurs near 81°, i.e., figure 21 [lay83].

The identification of S_cS proves quite difficult and shows considerable variability, much more than for samples of these same events to North America [*Lay and Helmberger*, 1981]. Often two component data, in conjunction with short-period observations, proves useful for this purpose as displayed in figure 3.5a. While the LPT (Long-period tangential) components show clear S and S_cS arrivals of the same polarity as expected, little signal is apparent on the SPT (Short-period tangential). S_cS appears identifiable at SDB but is not apparent at WIN. However, SKS can be seen in both LPR (Radial) records but not on SPR. S is especially clean on the SPR observations. Thus, while it appears that the propagational features of the S-phase ($\Delta = 72°$) are normal and well behaved as expected by their relatively simple paths (figure 3.2b), phases reaching the CMB appear unstable even between two stations near each other. An extra phase appears in some of these observations, denoted by

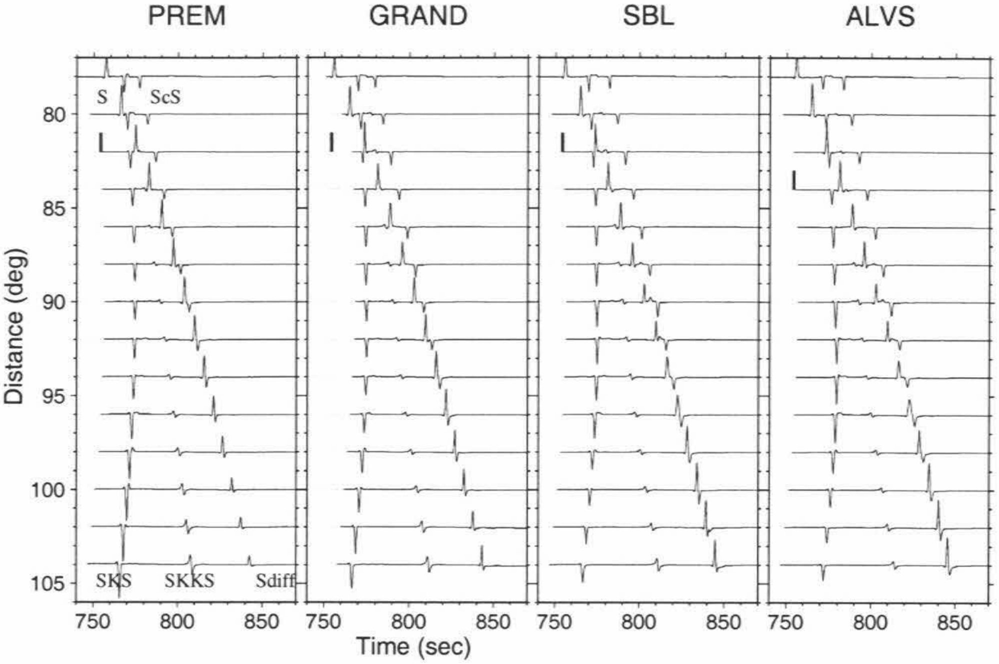

Figure 3.3: Synthetic record sections for the 1D PREM model, Grand's tomography model along the 2D projection displayed in figure 3.2, a modified version (SBL) containing only an enhanced basal layer (velocity decreases up to 5%) and our modified model (ALVS) displayed on the far right. The heavy bars indicate the location of S to SKS crossover for that particular model.

S_x, which could be a reflection from a reduced velocity structure (same polarity as S_cS), but this arrival is not so clear on the LPT, nor is it apparent at WIN.

In figure 3.5b, we display the records of PRE (731025, $\Delta = 82.3°$) with BUL (731025, $\Delta = 84.6°$ near the expected cross-over distance. The LPR records are those in the record section presented earlier in figure 3.4 and used later in modeling. The first arrival at PRE breaks downward on both the SPR and LPR components as expected for S. However, at BUL the first arrival is flipped in polarity indicating a crossover. Note that S_cS on the LPR components has the same polarity at both stations. The behavior of SPT is problematical in that it is difficult to explain the strength of SKS; perhaps it is anisotropic behavior [*Lay et al.*, 1998].

Many of these features argue for propagational complexities in the lower mantle and are difficult to explain with a simple 2D model. Thus, we will attempt to use travel-times referenced to a particular path from South America to BUL as a guide in constructing an average model (figure 3.1).

3.3.2 b) Travel-time Analysis

The travel-time picks were made from a combination of long-period and short-period records following the procedure discussed with respect to figure 3.5. These picks are plotted in figure 3.6. The open symbols are from the central African stations, AAE and NAI, and are late relative to southern Africa stations, as predicted by station statics (station travel-time corrections based on global P data [*Dziewonski and Anderson*, 1981]. South Africa stations, BUL and PRE, are slightly negative, while GRM, WIN, and SDB are slightly positive in terms of P-wave residuals. The stations AAE and NAI have large positive P residuals of 2.5 and 2.1 sec respectively, which we have mapped into S-wave residuals by multiplying by 2.5. This correction produces travel-time delays for S-waves encountering extreme upper-mantle structures comparable to those reported by [*Grand and Helmberger*, 1984], and also appears compatible with direct teleseismic offsets beneath Africa [*Ritsema et al.*, 1998b]. Also, the data have been corrected for event shifts by normalizing to common stations, i.e.,

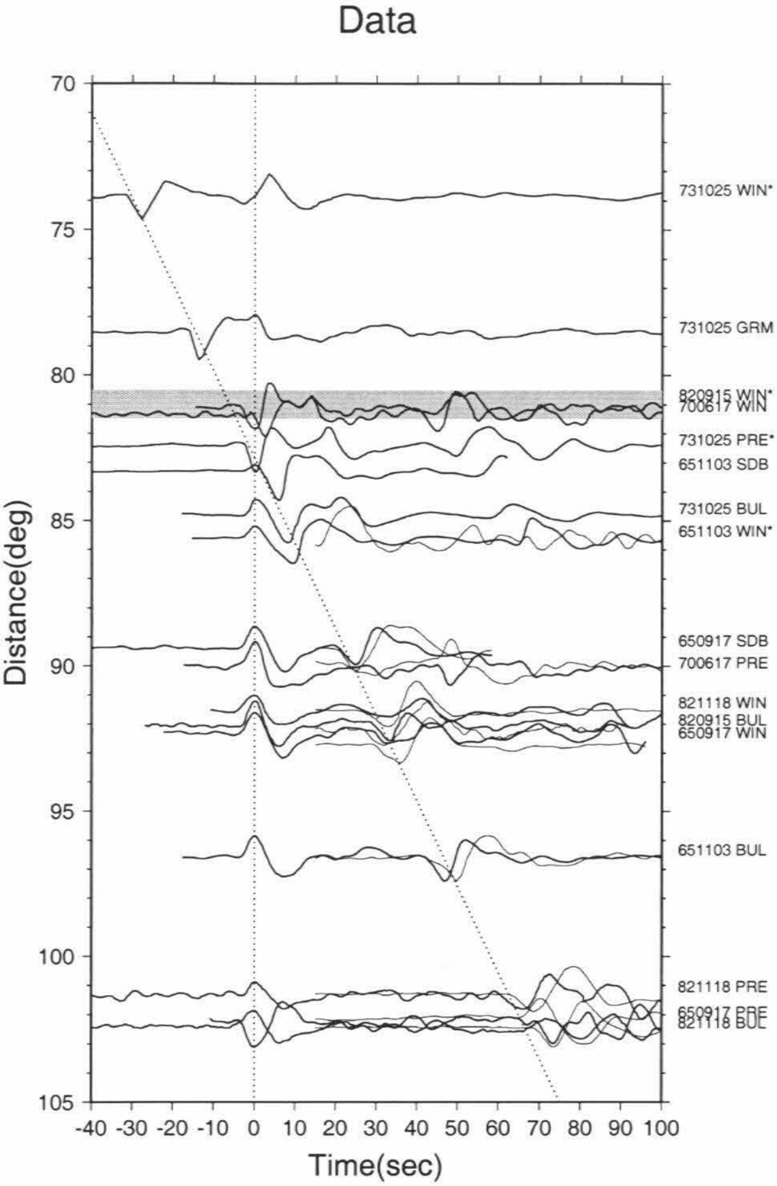

Figure 3.4: Composite record section of Long-period WWSSN observations displaying the S to SKS crossover. The observations are aligned on SKS (vertical line) which does not become a clear first arrival until 84°. The small up-swing occurring before S in the top traces is the well-known S to P phase (Moho conversion) which is easily identified by its lack of strength on the short-period traces. The traces marked with the star will be modeled later. The gray strip across the figure near 81° indicates the expected crossover range for PREM.

base line shifted essentially following the procedure used earlier [*Lay and Helmberger*, 1983], and others. Note that after these corrections, the solid and open symbols appear to form one population although with a large scatter. The scatter in this plot is relatively large and real since most of the picks are probably accurate to a sec. Since the S arrivals (solid dots) are recorded on a stable plateau, they average a few sec early relative to PREM. They change their behavior abruptly near 90° where they rapidly develop delays. SKS arrivals are consistently late except for a few isolated points.

To explain these travel-times, we processed 2D synthetics (figure 3.3) in a similar fashion. That is, we picked the travel-times for S and SKS on synthetics as if they were observations and constructed travel time curves as displayed in figure 3.6. Curves derived for two of these models are included in figure 3.6 for comparison. Grand's model fits the S travel-times well where they arrive early until their rays sample the slow basal layer near 90°, as displayed in figure 3.2. At this distance, a problem in the tomographic approximation develops where the first-arrival no longer travels in the slow basal layer as it would, assuming the ray path is appropriate for PREM reference model assumed in the tomographic methodology. Thus, to slow down the S-phase at the larger distance, we had to further reduce the velocities as in the ALVS model. The Grand model predicts SKS delays caused by crossing the slow basal layer which are compensated by the South African fast upper mantle yielding travel-times compatible with PREM. To fit the data better, we adopted a simple strategy. We keep Grand's global model and alter only velocities in the rectangular column indicated in figure 3.1, which extends upward for 10 layers (1600 km). For example, the synthetics displayed in figure 3.3 (SBL) were produced by allowing only the bottom layer to be anomalous (uniformly 4%). The best fitting modification contains an ad hoc mapping of Grand's block velocities; if the velocity anomaly is less than 4%, it remains the same, whereas, if the anomaly is over 4%, it is increased to 4%. Model ALVS was produced with these, obviously, non-unique changes. However, such a model fits the average travel-times quite well and it predicts reasonable waveform fits as addressed next.

Earlier we discussed 2D record sections (figure 3.3) at the ranges involving crossover from S to SKS. In figure 3.7, we display the synthetics appropriate for Grand's model and ours (ALVS) against observations from the same event (731025). The recordings at WIN and GRM do not show $(S_cS)_{sv}$ but have strong S and SKS. The S_cS is clear on other recordings on both the SV and SH components as discussed earlier in figure 3.5a, and the dotted line indicates their approximate separation with S. The top two records, PRE and BUL, are aligned on S and the bottom two on S_cS. The synthetics are plotted as a record section with reducing time of 8.3 (seconds/degree) and aligned on GRM. Note that the crossover for Grand's model occurs before 82° while it is shifted well past 82° in the data and in the ALVS model. Note that the two stations, BUL and PRE, are close together such that their ray paths are quite similar, providing a definitive 2D measure of crossover distance. Thus, our model does well in explaining the crossover data where S is fast and SKS is slow.

The waveform fits at larger ranges becomes more problematic since the data are rather erratic (figure 3.4), suggesting strong 3D effects. While our model predicts reasonable fits to the timing separations between SKS, SKKS, and S_{diff} [*Ding*, 1997], the waveform fits to S_{diff} are not very convincing and will be addressed in future efforts.

3.4 Discussion and Summary

The African anomaly discussed above is associated with a large-scale feature ($\sim$ 3000 km), e.g., *Su et al.* [1992], and is sometimes referred to as super-plume. The long wavelength lower mantle structure is revealed both in slow direct S-waves [*Masters et al.*, 1996] and in differential times [*Masters and Shearer*, 1992]. This structure is similar to the central Pacific anomaly with a 2 to 4% drop in shear velocity in the lower mantle according to these studies. The preferred shapes of these features are horizontally oriented pancakes [*Ritsema et al.*, 1998a] with broad horizontal dimensions compared to vertical scales. Such shapes do not allow the relatively sharp features in timing required here and in [*Ritsema et al.*, 1998a]. Part of the problem

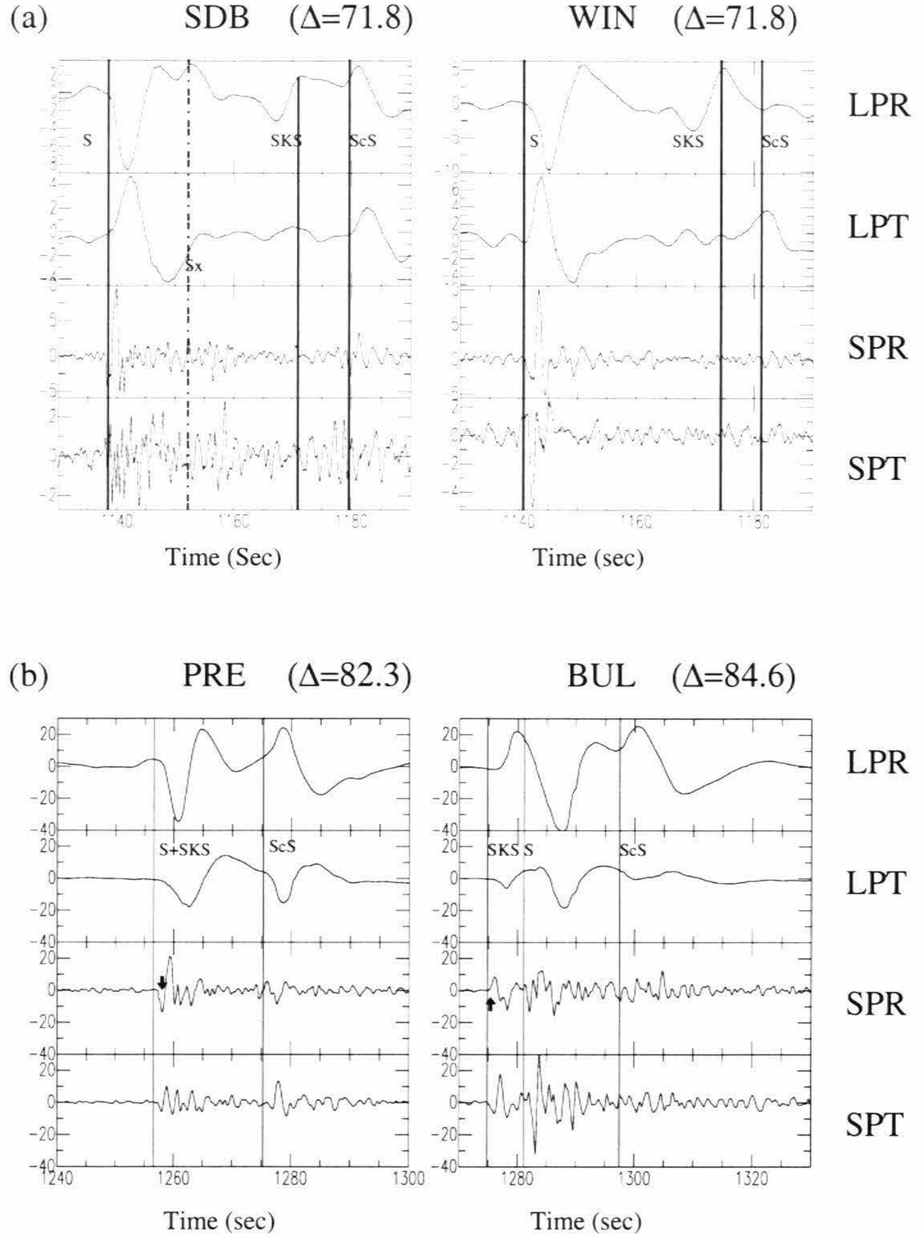

Figure 3.5: Comparison of short and long period WWSSN observations before crossover (a) and at crossover (b). The data in figure 3.5a are from the event (670117) and are aligned on direct S with vertical lines indicating the various arrivals. The data in figure 3.5b are from the special event (731025) indicated in figure 3.4 displaying crossover PRE (before) and BUL (after). Note the change in polarity on the SRP component marked by an arrow.

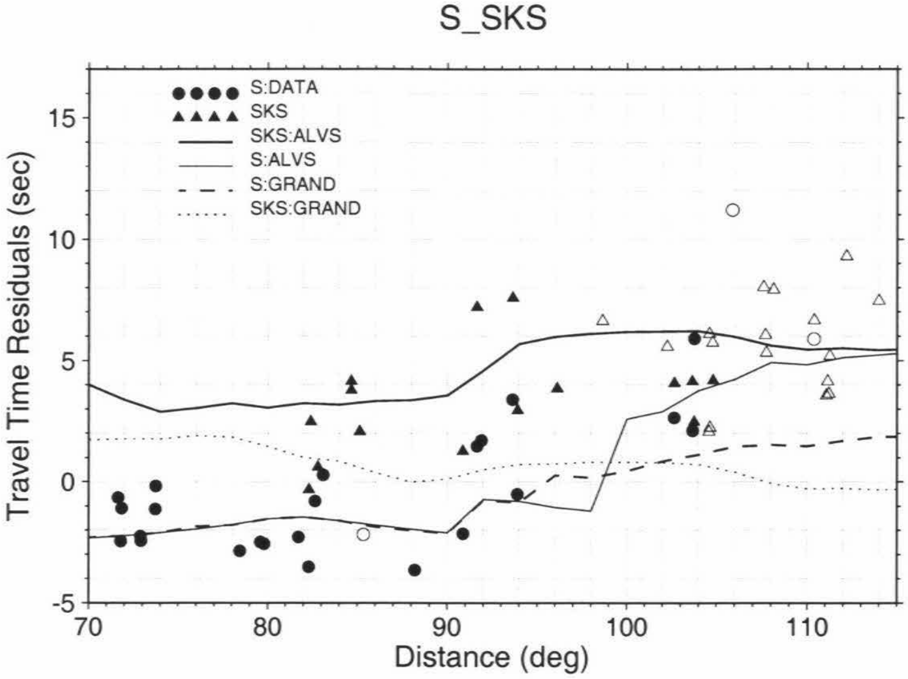

Figure 3.6: Travel-time picks relative to PREM for S and SKS (observed - PREM predictions). Open symbols are data from stations NAI and AAE while the solid symbols indicate anomalies from the South African stations. All data has been baseline shifted relative to BUL. Lines correspond to synthetic predictions from the two models presented earlier in figure 3.2.

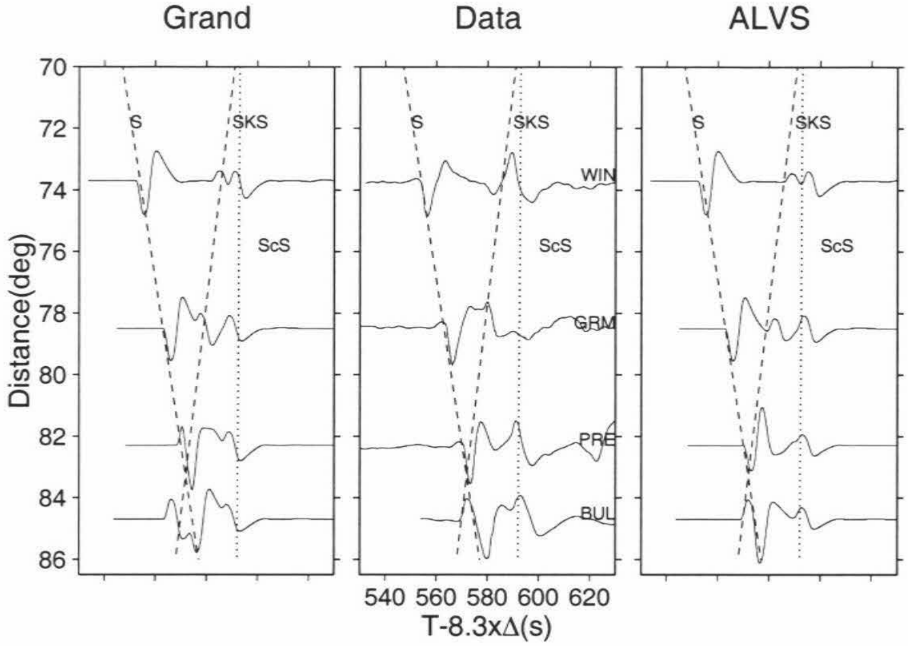

Figure 3.7: Comparison of observations from the event (731025) aligned on S along with synthetics predicted from the Grand model and ALVS. Dotted lines indicate the averaged observed S_cS (SH) relative times. The dashed lines are the same in all three panels indicating observed crossover.

is that most long-period models do not resolve the mid-African rift. Thus, trade-offs in mapping short wavelength shallow variations into deep structure can be quite serious. Grand's model does better in this situation because it resolves the fine-scale upper mantle as displayed in figure 3.8c. This cross section is appropriate for paths from Sandwich Island to AAE along the 2D cut indicated in figure 3.1. Travel-times predicted from synthetics generated by this model are given on the right along with the data after [*Ritsema et al.*, 1998a]. Note the spectacular increase in the observed travel times as the rays approach 70°, with about one-third of this feature caused by the upper mantle [*Ritsema et al.*, 1998b]. Prediction of S delays for the model proposed by [*Ritsema et al.*, 1998a] and our proposed modifications (ALVS) are given in figure 3.8b and 8a for comparison. As in figure 3.2b, we have simply inflated Grand's anomalies in the region above D" to 4% as discussed earlier to construct the ALVS feature displayed.

In Section B (figure 3.8), the global model has been removed and thus it produces PREM travel-times at ranges less than 65°. By applying a baseline shift downward a few seconds to correct for the shield structure appropriate at these ranges, we would under-predict the latest arrivals ($\Delta = 75°$) since they would lack the ridge effects. Consistent upper mantle corrections show that this model fits travel-times well [*Ritsema et al.*, 1998a]. Both models in figure 3.8A and 8C contain the weak slow velocity zone on the S descending path which produces nearly PREM travel-times (0 residuals), essentially a balance between this feature and the shield upper mantle beneath the stations. If we baseline shift the prediction in figure 3.8A down about 4 sec to fix this problem, we would get excellent fits. Thus, a modification of Grand's model of the type applied here produces a reasonable fit to this remarkable dataset.

In summary, these observations suggest fundamental constraints on the dynamics of the lower mantle: (1) the magnitude of the shear wave anomaly is probably substantial, ~-4%, extends over a 1000 km lateral scale while reaching a height 1600 km above the CMB, (2) the sides and top of the anomaly are 'relatively' sharp in comparison to tomography studies as it does not appear to be diffusive over 1000 km length scales, and (3) the slow tabular anomaly is either directly above or imme-

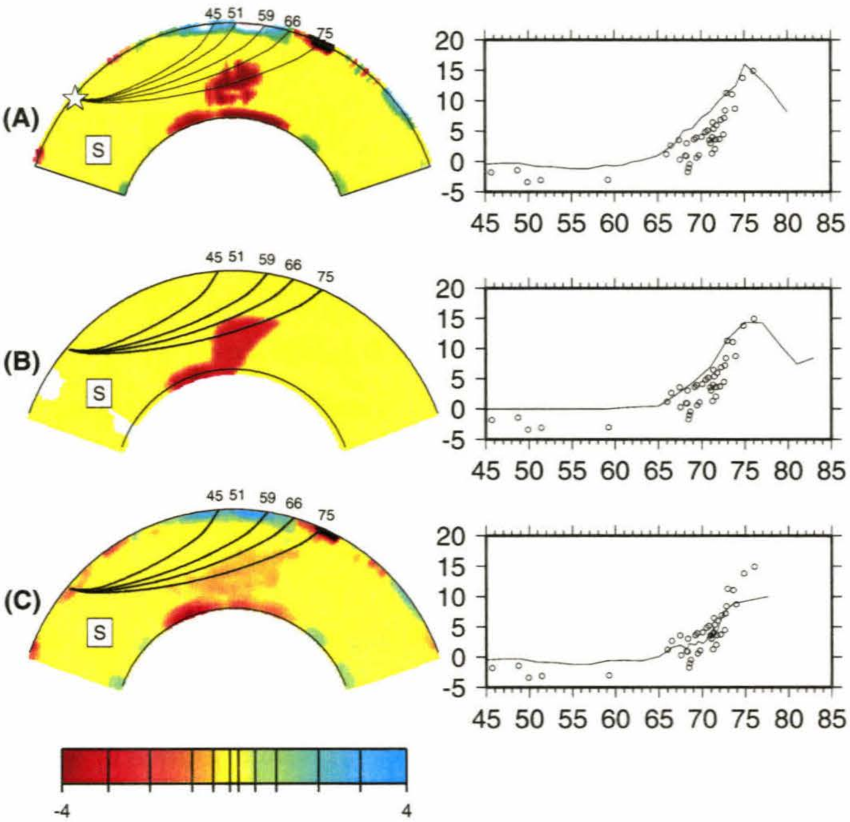

Figure 3.8: Comparison of three proposed cross sections along the path from Sandwich Island (star) to Hindu-Kush passing through AAE (figure 3.1). Travel-time predictions (residuals in sec, model-PREM) for these models, *A* (modified Grand), *B* (Ritsema *et al.*, 1999), and *C* (Grand's model), along with observations (in deg.) after Ritsema *et al.* (1999), are displayed on the right.

diately connected to a substantial, low shear velocity basal layer which appears to be a few hundred kilometers high. Together with the observation that the elevated part of the seismic anomaly is directly below topographically high southern Africa [*Lithgow-Bertelloni and Silver*, 1998], these observations give conflicting constraints on the dynamics. The long-standing interpretation of the African seismic anomaly is that it represents a long-lived, hot mantle upwelling [*Hager et al.*, 1985]. The high topography of Africa, which may be dynamic [*Lithgow-Bertelloni and Silver*, 1998; *Hager et al.*, 1985], probably increased rapidly over the last 20-30 Ma [*Partridge and Maud*, 1987; *Burke*, 1996]. Qualitatively, this is consistent with a large thermal plume which has recently erupted off the core-mantle boundary. However, thermal plumes in a temperature-dependent viscosity fluid, erupting off a hot base (Rayleigh number $>10^7$) will always draw nearly all of the hot boundary layer fluid into the plume before detaching from the base with only a very narrow plume tail [*Gurnis et al.*, 1999]. Thus, such small features would be difficult to resolve from seismology. The persistence of substantial, thick basal shear velocity anomaly (in our model ALVS) appears problematical for a large erupted thermal. Interconnection with the base can be maintained by a lower Rayleigh number, a negatively buoyant basal chemical layer which counteracts the thermal buoyancy [*Tackley*, 1998], or a thermal rising in a compressible mantle [*Thompson and Tackley*, 1998]. Lower Rayleigh number plumes are inconsistent with the relatively sharp edges of the seismic anomaly and the rapid Cenozoic uplift of southern Africa [*Partridge and Maud*, 1987; *Burke*, 1996]. If the anomaly is close to being neutrally buoyant, as recently suggested [*Kellogg et al.*, 1999], then it is difficult to understand how the anomaly can uplift southern Africa by about 500 m over the last 20-30 Ma. Preliminary models suggest that starting plumes in a compressible mantle can maintain connection to a robust basal layer while also having sharp edges [*Thompson and Tackley*, 1998]. Further refinements in the seismic structure of the African anomaly, especially when combined with dynamic models and geologic constraints, will hopefully resolve fundamental questions concerning the dynamics taking place beneath the African continent.

In conclusion, a detailed study of S-wave observations along a corridor from South

America to South Africa confirms the existence of a very anomalous structure beneath the southeastern Atlantic and South Africa. SKS delays of up to 8 sec are commonly observed which requires a vertically positioned structure whose shape has already been defined [*Loper and Lay*, 1995] but with increased velocity drops of up to 3 to 4%. The details are not resolved; however, at this stage of definition, it appears to be the most significant lower mantle structure on Earth.

Chapter 4 Horizontal Transition from Fast to Slow Structures at the Core-Mantle Boundary

4.1 Abstract

Recent Tomographic studies of the deep mantle have revealed large-scale low velocity zones beneath Africa and relatively fast velocity zones beneath South America. Here we conduct a concentrated core-mantle boundary (CMB) study across this transition zone from fast-to-slow beneath the South Atlantic. Deep South American earthquakes recorded in Africa provide S and ScS waveform data at core-grazing distances of 85 to 105°. The waveform interference pattern produced at these ranges provides an excellent sample of the CMB structure in the vicinity of the ScS bounce point which can be used to map out regions of low-velocity-zones (<5% reductions) and the more extreme ultra-low-velocity-zones (>10% reductions). The strongest anomalies occur at the western edge roughly beneath the Tristat Plateau with weaker structures to the east beneath the so-called "Great Africa Plume." These results agree with dynamic models where strong local upwellings develop at the edges of D" (fast) structures.

4.2 Introduction

Recent studies of the mantle have revealed large-scale low velocity zones beneath Africa that extends from the core-mantle boundary (CMB) to the African rift system [Grand *et al.*, 1997, and Ritsema *et al.*, 1999]. Most modern tomographic images of this region as displayed by the latter agree with this general picture. This feature is inferred to be upwelling based on models predicting uplifted topography [*Gur-*

nis et al., 2000] [Lithgow-Bertelloni and Silver (1998)]. In contrast, the structure beneath South America appears fast (Grand, 1994) and has been interpreted as subducted lithosphere (Richards and Engebretson, 1992). While the subducted material in dynamic models typically shows complex forms of folding and buckling at mid-mantle depths, it generally forms a flat-lying layer at the CMB. As the material heats up, it erupts into local plume-like structures. The most dramatic upwelling features are associated with models containing a phase-change, which tends to inhibit convection and allow higher temperatures to be reached before eruption (Sidorin *et al.*, 1999). The strongest eruptions nearly always emerge at the slab tip where advective thickening of thermal boundary layer occurs caused by horizontal creep of the cold slab as displayed in figure 4.1 (upper panel). Enticed by these dynamic predictions, we conducted a high-resolution study of seismic phases sampling the CMB at such a possible margin beneath the South Atlantic (lower panel of figure 4.1).

4.3 Data and Analysis

Deep South American earthquakes were used as sources rich in downward generated SH (tangential shear waves) seismic energy producing strong S and ScS (see Table 4.1). These phases propagate along separate paths at ranges less than 80° where they have been used extensively for studying D" (Lay and Helmberger (1983), Lay *et al.* (1998)). The source-side portions of the paths sample the relatively fast region relative to the receiver-side portion, which are located within slow velocities. At the largest ranges, these paths approach each other (figure 4.1b). Synthetics generated for 2D models similar to this are displayed in Ni *et al.* (1999). However, beyond 90°, S and ScS have nearly identical paths above D" (lowermost mantle), and 1D models with fine structure near the CMB produce nearly the same synthetics. Thus, for simplicity we will concentrate on a few 1D models (figure 4.2) that can explain many of the observed waveforms. We have included PREM as a reference model and a few recently proposed styles of CMB structure: a relatively thick low-velocity zone (LVZ, red), Ni *et al.* (1999), Ritsema *et al.* (1998)), and a thin ULVZ model (Garnero and

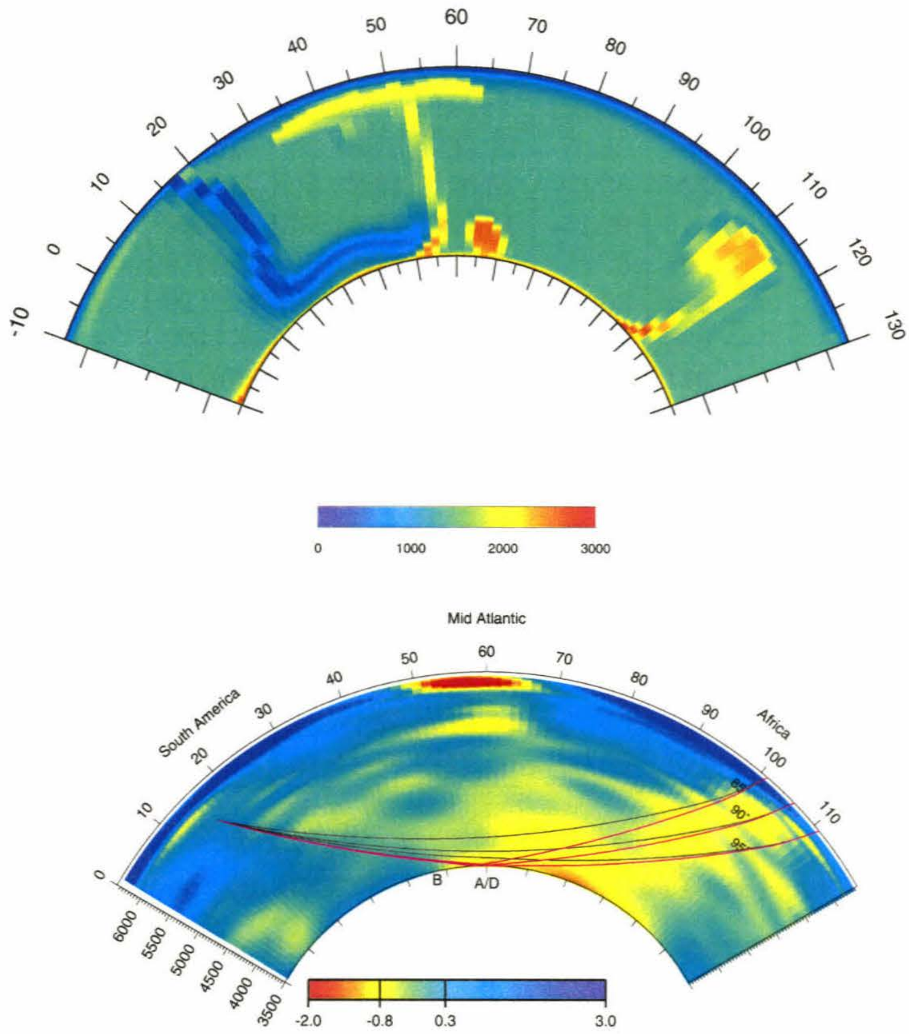

Figure 4.1: Upper panel displays a dynamic prediction (2D) of a relatively strong cold slab pushing aside a hot thermal boundary layer. Note the hot material (red) apparently forming at the leading edge of the downwelling. Such a feature with various shapes commonly occurs for a variety of parameters, Sidorin (1999). The lower panel displays a 2D crosssection of a tomographic study, Ritsema et al. (1999), indicating some similarity, but with weaker downwelling and stronger upwelling. Most tomographic models agree with the general pattern displayed here, Su et al. (1994), Li and Romanowicz (1996), Masters et al. (1996). The model by Grand (1994) is slightly different, containing weaker structures above D" and stronger features in D". It also displays a stronger downwelling structure. Included in the lower panel are some example ray paths of S and ScS at large ranges, 85 to 95°, showing the similarity of paths through the mantle at ranges beyond 95°. Thus, the interference of these two phases is controlled by the bottommost mantle structure.

Helmberger (1995)).

Table 4.1: South America Events used in this study

No	date	time	lat(○)	lon(○)	depth(km)
1	941020	01:15:16	-39.19	-70.80	164
2	940819	10:02:51	-26.65	-63.38	565
3	980729	07:14:24	-32.31	-71.29	51
4	970902	12:13:22	3.85	-75.75	199
5	971028	06:15:17	-4.37	-76.60	112
6	971128	22:53:41	-13.74	-68.79	586
7	981008	04:51:42	-16.12	-71.40	136
8	991130	04:01:53	-18.78	-69.05	127
9	970123	02:15:22	-22.00	-65.72	276
10	950923	22:31:58	-10.53	-78.70	73
11	950208	18:40:25	4.16	-76.64	69
12	971015	01:03:33	-30.93	-71.22	58
13	980403	22:01:48	-8.15	-74.24	164
14	990403	06:17:18	-16.66	-72.66	87
15	990525	16:42:05	-27.93	-66.93	169
16	950214	15:53:56	-23.29	-67.70	156
17	941212	07:41:55	-17.50	-69.65	151

Synthetics generated with GRT (Helmberger (1983)) for these three 1D models are presented in figure 4.3. Note that the S and ScS paths approach each other for PREM near 93°, which defines the beginning of the S-wave shadow zone. There is only a slight change in the rise-time of the S-wave (onset to the peak amplitude) for these PREM synthetics due to the slightly positive velocity gradient in the lower 200 km of the model. Adding a low-velocity gradient to D" has a strong effect on S causing the shadow to begin at shorter distances (i.e., beyond about 95°) as displayed in the second column. The reduced gradient also causes a delayed S-wave onset as indicated by the reference lines. The synthetics in the third column are for a model containing an ULVZ. These contain an S wave looking much like PREM but with a very late ScS arrival. The waveshapes in these three columns are diagnostic of their respective structures, while PREM synthetics are pulse-like at 93°. LVZ synthetics consist of two interfering pulses along with a gentle S-wave onset and ULVZ synthetics contain a late and strong secondary arrival (ScS). S-wave recording, at African stations shown

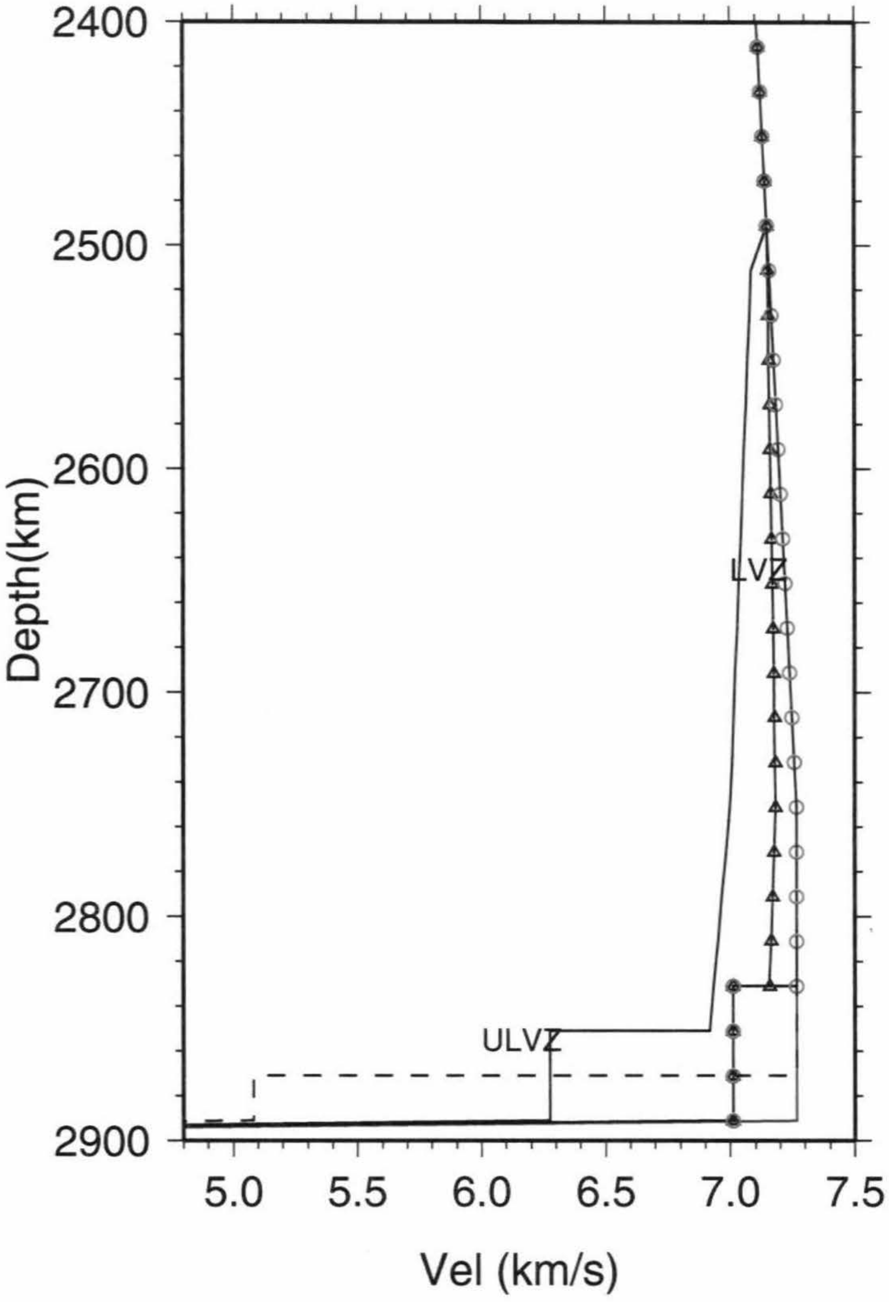

Figure 4.2: Four representative lowermost mantle models; PREM (Dziewonski and Anderson, 1995), two LVZ models in red and green, and an ULVZ model. The latter model contains a thin basal layer with a drop of 30% in shear velocity. The fourth model (solid black) is a combination of ULVZ and LVZ; it features a fairly smooth gradient from 400km down to 40km, there is 10% shear velocity drop within the basal 40km.

on the right in figure 4.3, displays a great deal of variation. The observations in red favor shapes produced by ULVZ-type models with strong secondary arrivals. Some of these also have gradual onsets diagnostic of an LVZ-type of structure above the ULVZ. The traces in gold resemble the LVZ-type synthetics.

Using these synthetics as a guide, we picked the travel time differentials (ScS-S) for a population of events along these cross sections. These data are presented in figure 4.4 along with picks from four sets of synthetics; the three presented in figure 4.3 plus an even thicker ULVZ of 30 km. The symbols correspond to those displayed on a map (figure 4.5) plotted at the ScS bounce point.

The upper panel of figure 4.5 displays D" tomographic results showing the transition from beneath South America (relatively fast velocity) to Western Africa (relatively slow velocity). The large blue dots are isolated samples of (ScS-S) recorded at IRIS stations located on Atlantic Islands, ASCN and SHEL. These records and differential times confirm this tomographic model with a relatively fast D". The diamonds indicate the samples obtained from individual African stations, and the triangles are the samples from the Tanzania array. The lower panel (figure 4.5) indicates the character of 1D models best fitting these observations. Red symbols indicate an ULVZ while orange and gold suggest an LVZ-type structure. These symbols are grouped in ellipsoids with variable line thickness indicating the relative thicknesses of the LVZ needed in the modeling. In general, neighboring paths produce similar waveforms and travel time differentials allowing these arbitrary shaped enclosures. Unfortunately, samples to the right of these enclosures are sparse due to station coverage. The few that do exist (Green traces observed at KMBO in figure 3) favor a model with a strong LVZ, and possibly an ULVZ to enhance late arriving energy. Note that these same events 6 and 7 are relatively narrow at other stations (BOSA 6 & 7). Moreover, SKS phases at KMBO (not displayed) look like the first pulse at BOSA. Thus, the broadening at KMBO at ranges 102 to 108° is probably a propagational effect caused by an ULVZ structure as interpreted above. Most of the red traces (figure 4.5) display delayed ScS pulses relative to S, ranging in delays of 5 to 10 sec. Adding a low velocity structure above the ULVZ tends to produce the gradual beginning of

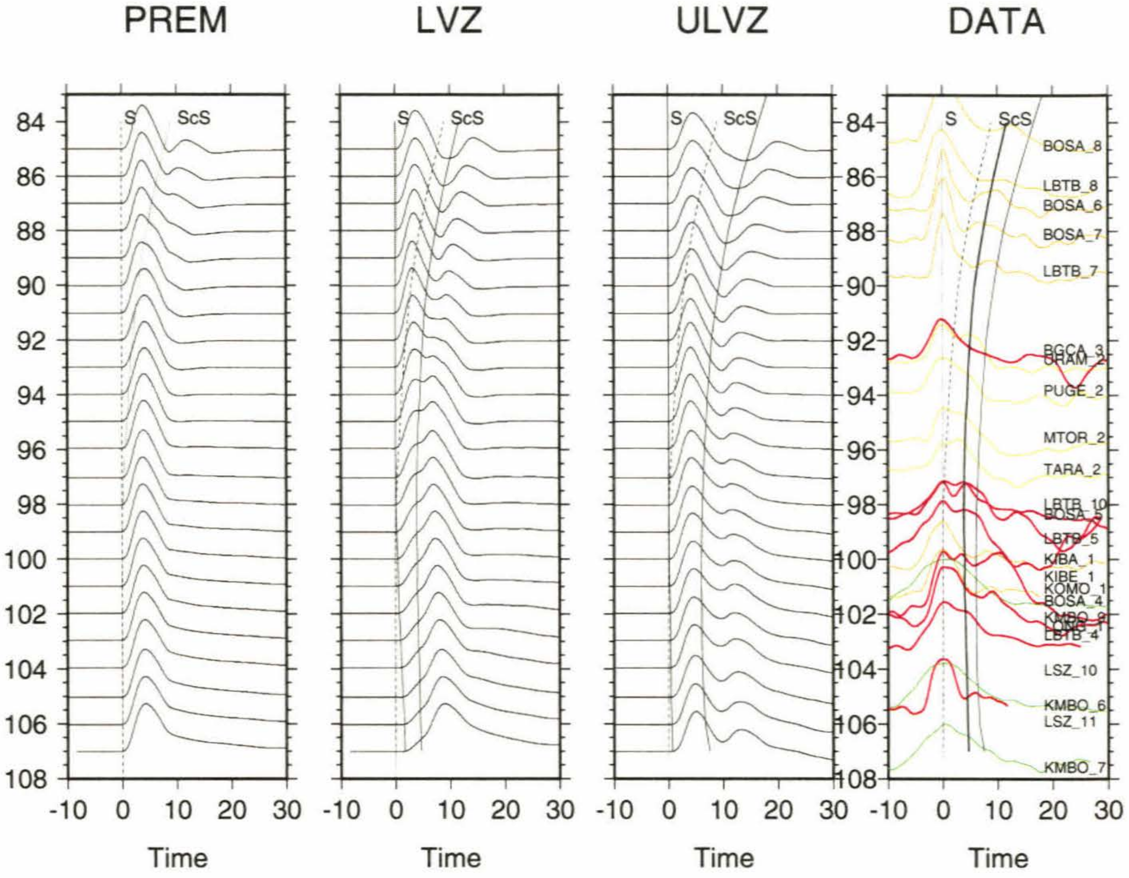

Figure 4.3: Synthetic seismograms for 1D models and data. Column (PREM) displays synthetics for PREM, note that beyond 90 degrees, S and ScS merge to form one pulse, waveforms are aligned on S, with onset marked by the vertical dashed line, and the dotted line indicates onset of ScS. Column (LVZ) displays synthetics for a model similar to PREM but with a 60 km layer of 4% slower shear velocity above the CMB along with a 300 km tapered gradient to match with PREM at the top (LVZ, red). The low velocity layer (LVZ) separates ScS from S for distances larger than 90, but from 100 degree on, S loses its strength due to diffraction caused by the 4% discontinuity as observed on KMBO (green in Data column) data, dashed lines indicating PREM S and ScS arrivals, and solid lines indicate S and ScS for the LVZ model. Column (ULVZ) shows synthetics for a model with a layer 20 km thick with 30% velocity reduction above CMB. The dashed lines indicate PREM S and ScS arrival and solid lines for S and ScS for ULVZ model. Column (Data) displays seismograms from IRIS stations and Tanzania Array. Data are aligned on the peak of the first arrival, dashed lines indicate PREM S and ScS arrivals, the thick curved solid line indicates ScS arrival for model LVZ (red) and the thin curved line indicates the ScS arrival for model ULVZ.

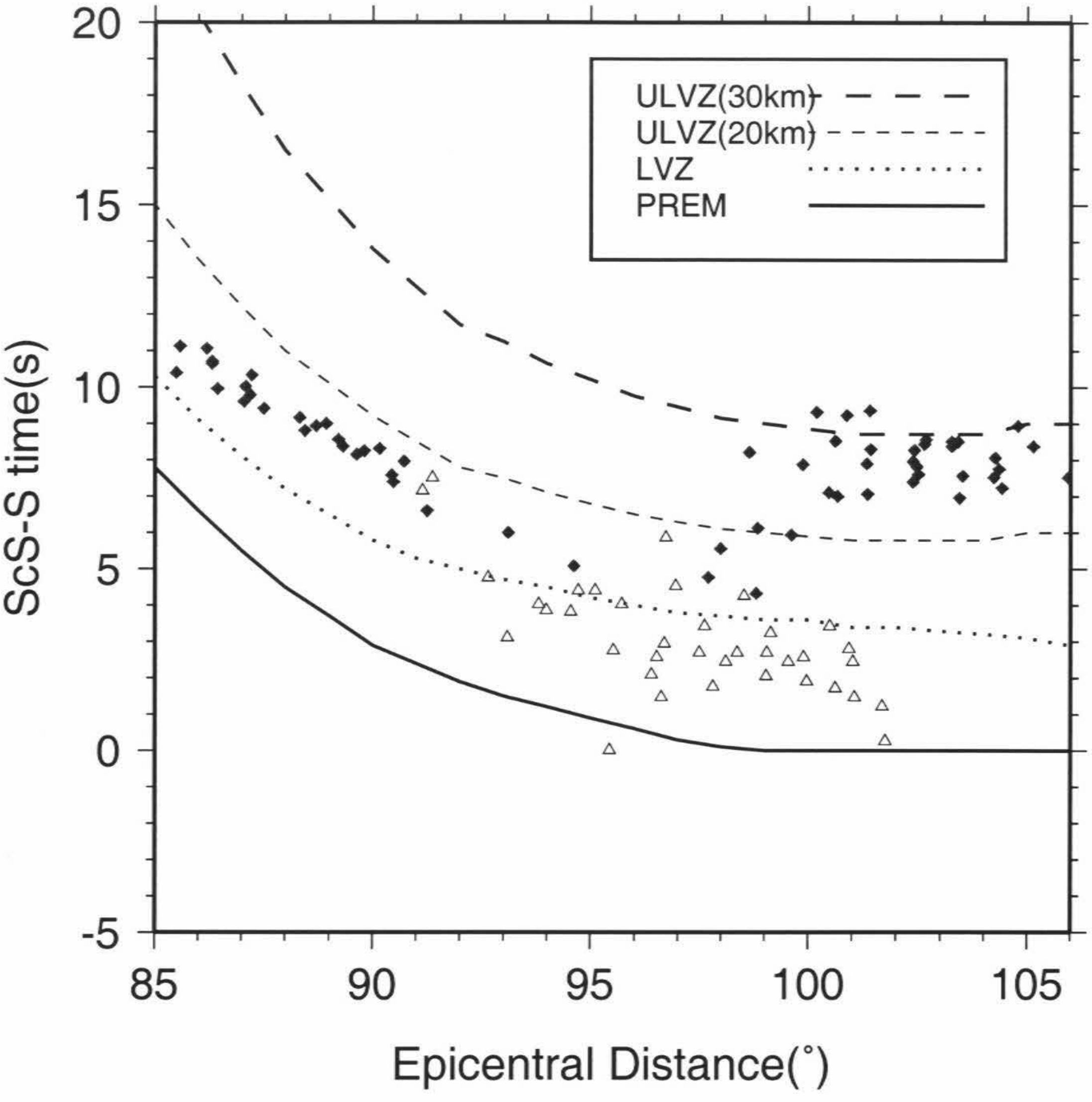

Figure 4.4: Plot of observed differential travel times (ScS-S) taken along the corridor from South America to South Africa along with theoretical predictions for the various models. The data read from the Tanzania Array are plotted as triangles while all others are given in diamonds. Those data nearest to PREM come from the Tanzania Array. The most anomalous points occur at the largest ranges where values as high as 10 secs are reached. The ScS bounce points for these extreme values occur at the fast-to-slow margin as presented in figure 4.5.

some of the observations. Event (4) displayed in figure 3 (LBTB) has been recorded by the African Array transect, Wen *et al.* (1998). This array of 55 stations brackets LBTB and BOSA, and a record section of this data clearly displays a move-out of ScS relative to S of about 8 sec at 102° similar to the observations displayed here. Their 2D model also contains an ULVZ which is a 300 km layer with 2% velocity reduction at the top and 12% velocity reduction at CMB.

In short, the CMB structure enclosed by the large ellipsoid in figure 4.5 is very complex and anomalous. Also included in figure 4.5 are a small number of isolated samples obtained from station BGCA indicated by the black diamonds. Corresponding S waveshapes are not PREM-like but appear to be more indicative of a LVZ structure than a ULVZ but are too sparse to be definitive. The level of fine-scale variability can be seen in samples of observations occurring in overlapping regions (D+A) for paths event 2 and 16 to TAN. These observations, compared against synthetics, are presented in figure 4.6. The dashed traces are taken from the LVZ column of synthetics discussed earlier along with a model containing only a LVZ (green) confined to the lower 60 km. While the synthetics are similar for these two models, the S and ScS phases are separated slightly more and the strengths of S relative to ScS have some range dependence. We examined many 1D models bracketed by the two discussed here. The main feature required for the separation of S and ScS is the bottom 60 km layer with reduced velocity. Reducing the velocity and thinning the layer works to some extent but causes the pulses beyond 100° to develop two peaks if the velocity drop becomes greater than about 5% unless the thickness reduces to less than 10 km. It appears that shear velocity plays the dominant role in these waveform experiments with some dependence on density and attenuation. Thus, there is a uniqueness problem even for 1D models similar to that found in Garnero and Helmberger (1998).

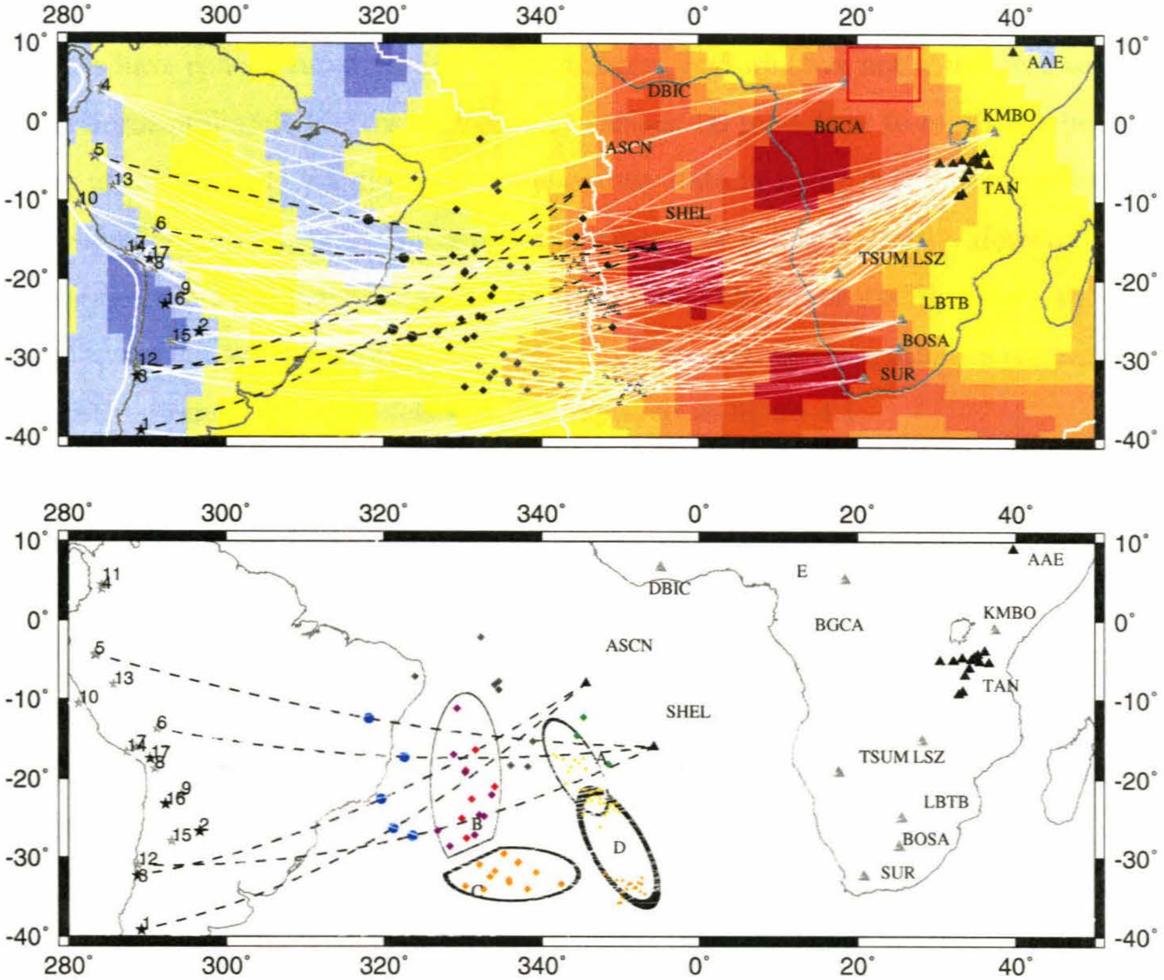

Figure 4.5: The top panel displays the CMB sampling area and earthquakes (stars) used in this study. The color background displays shear wave anomalies at the CMB (Ritsema et al., 1999) with blue indicating fast velocities and red slow (± 1.5%). The mid-Atlantic ridge is shown with gray thick lines. The symbols (diamonds, circles, and triangles) show the bounce points of ScS ray paths. Note that the bounce points covers regions from fast to slow velocities. In the bottom panel (B), the areas are grouped into regions with similar waveform characteristics. The enclosure line thickness indicates LVZ thickness (300 km for region D, 60 km for A, 140 km for region C, 20 km for region B). The different colors of the symbols indicate level of velocity drop. Red for 30% (ULVZ) reduction in shear velocity, orange for 4%, blue indicates fast anomaly, green diamonds also represent 4% anomaly but complex. Note that the red symbols are at the boundary between fast and slow tomographic anomalies as predicted by dynamic models. The box displayed in the upper panel near AAE indicates a possible ULVZ determined by SKS-SKPdS interference, Helmberger et al. (2000).

4.4 Discussion

Our analyses have concentrated on first order features, and we have not attempted to resolve the horizontal scale lengths between the various 1D models or to establish the uniqueness of each model. We did display some array data in figure 4.6 that suggests there are significant changes in D" across dimensions of a few degrees. However, these changes could be influenced by the 3D structure of the lower mantle. This is a difficult question but we can address it somewhat by generating 2D synthetics (figure 4.7) for existing tomographic models such as displayed in figure 4.1.

These synthetics were produced with a generalized ray code modified to treat 2D structures as discussed in Ni *et al.* (2000). The geometric ray paths for 85°, 90°, and 95° are displayed in figure 4.1b. Note that from 85 to 93°, the paths travel mostly in the fast structures, which explains why the S pulses arrive earlier than PREM and then fall behind at larger ranges when the paths sample the slow basal velocities. Overall, these synthetics are not that much different from those generated by PREM where ScS is not noted beyond 87°. Resolving ScS from S obviously becomes more difficult (figure 4.7) as one filters to long periods as done in most long-period (LP) tomography studies. The resolution of ScS remains difficult in LP synthetics even after adding an ULVZ. This difficulty in separating ScS from S probably prevents long-period analyses from detecting the extreme features discussed here or in helping much is the analysis of 3D structure in D". However, these LP results may explain why there are some basic differences in LP tomographic models and Grand's results, who used shorter-period analog data, consequently forces more extreme features into D". In particular, the LVZ models presented here are quite compatible with Grand's results, namely, a lower basal layer (200 km) with about a 3% reduction, Ritsema *et al.* (1998) and Ni *et al.* (1999). Thus, it appears that most of the well documented Great African Plume structure [Su *et al.* (1994)] is underlaid by a mild low velocity zone with a few known ULVZ situated at its edges. The one introduced here appears at the western margin. The width of the structure is probably less than 500 km based on how rapid the waveforms change with distance, which is compatible with

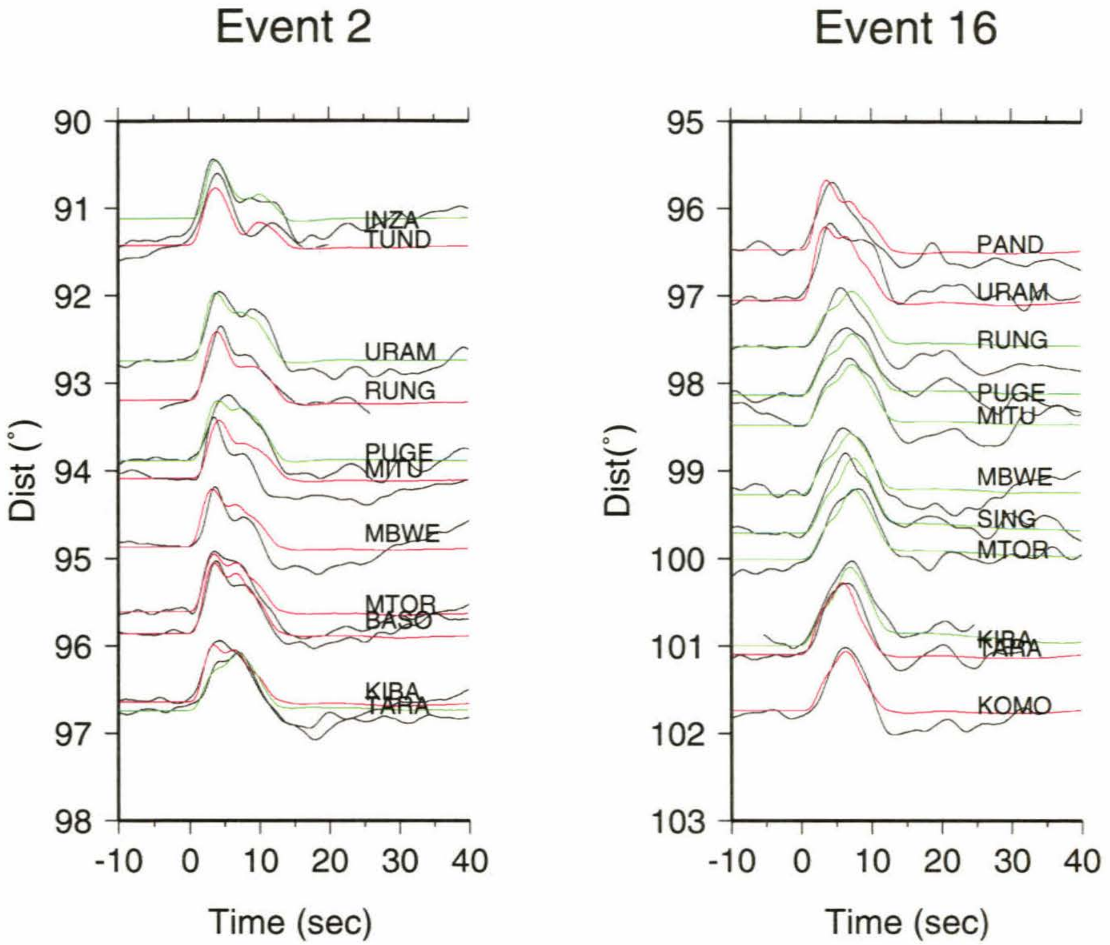

Figure 4.6: Comparison of synthetics from the two LVZ models (red containing a negative gradient, and green containing only a low velocity-based layer), against array data (Tanzania) for two neighboring events. Most observed waveforms fit one of these two models. Stations INZA and URAM are located at the northwest corner of the array while stations TUND and PAND are at the southern corner. These observations display the largest differences. Excluding these stations, the remaining observations sample a narrow corridor roughly 250 km long and less than 50 km across. These observations are quite compatible with each other as expected and show little signs of a late arriving ScS indicative of ULVZ synthetics.

the results of other methods used in studies of these anomalous structures in other regions, see review by Lay *et al.* (1998). Some of these studies suggest Gaussian or ridge-shaped ULVZ structures with horizontal dimensions of a few hundred kms, Helmberger *et al.* (2000). One of these zones occurs under Iceland and another occurs at the northeastern edge of the African upwelling as displayed in figure 4.5.

In summary, it appears that an ULVZ or some type of very anomalous structure occurs at the western edge of the subducted material between the fast-to-slow margins as predicted by some dynamic models. This structure with a reduction in shear velocity of 30% favors some melting as suggested by *Williams and Garnero* [1996] and in dynamic models involving viscous heating [*Steinbach and Yuen*, 1999]. The structure to the east beneath the upwelling appears to be complex but with fewer signs of ULVZ's. These observations favor models with thick (200 km) LVZ zones of about 3 to 4% reduction compatible with some tomographic studies. Thus, the relationship between historic slab subduction and possible upwelling near their margins, as predicted by dynamic models, is becoming more apparent in deep mantle velocity structure.

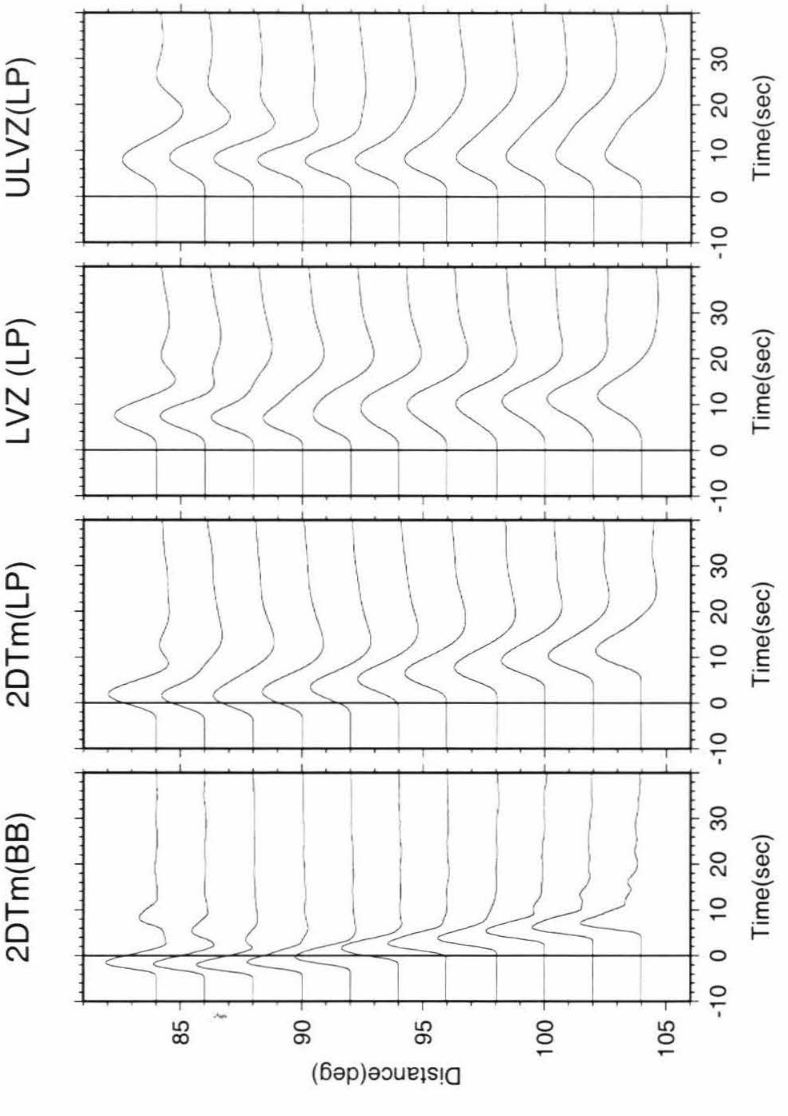

Figure 4.7: Synthetic seismograms generated from a cross section through a Tomographic model (Ritsema *et al.* (1991) as displayed in figure 4.1) labeled 2DT$_m$ (BB) for broadband and LP for long-period along with LP results from the LVZ and ULVZ models. The LP is that used in the above tomographic modeling, namely, the removal of all periods less than 15 sec. A reference line of travel times relative to PREM is included in each profile. The first two columns indicate the relative shifts of arrivals caused by the 2D structure, where the signals start about 5 secs early at near-in ranges, and then gradually become late at larger ranges. Adding the LP filter makes it difficult to resolve ScS, which is probably why most LP studies do not detect such features at these ranges, but are able to map-out the larger features.

Chapter 5 The Low Velocity Structure beneath Africa and Atlantic from Waveform and Travel Time Modeling

5.1 Abstract

A major difficulty encountered in lower mantle tomography studies is isolating the S phase from its core phases, SKS and ScS. Fortunately, the interference from 75 to 105 degrees produced by these combined arrivals is distinct, since ScSsv and ScSsh have opposite polarity. We developed a simple algorithm to decipher and determine the arrival times of these phases by matching simulated synthetics to the observed waveforms. This is achieved by computing the various arrivals separately using the GRT method for PREM. The arrivals are allowed to shift in relative timings to match the data. Tomographic model can then be constructed or existing tomographic models can be altered to match these data and new 2D synthetics constructed to better fit the waveforms. These updated synthetics can again be decomposed and re-assembled and the process repeated. This algorithm is applied to a combination of analog and digital data along a corridor from South America to Africa and a high resolution 2D model is constructed. The cross section begins with a relative fast basal layer beneath South America which abuts against an ULVZ with normal mantle above it. The fast structure transitions into a D" layer with reduced S-wave velocity by 3% which is about 180 km thick and 2000 km long. The layer grows rapidly in thickness, reaching at least 1500 km above CMB beneath Africa.

5.2 Introduction

The large scale low velocity structure beneath Africa is revealed in various shear velocity tomographic models ([*Masters et al.*, 1996], [*Su et al.*, 1992],[*Grand*, 1994],[*Ritsema et al.*, 1999]). Improved resolution of this low velocity structure has been achieved by array analysis of SKS, S, ScS travel times (*Ritsema et al.* [1998a]). They find that S is progressively delayed up to 10 seconds with respect to PREM for a South Sandwich Island earthquake recorded by Tanzania array with epicentral distances from 60 to 76 degrees, and ScS-S from the dataset is about 12 seconds larger than PREM predictions. This differential travel time anomaly can be explained by introducing a 2D structure where S samples a longer portion of the slow paths relative to ScS. Combined with SKS and S travel time from a Drake Passage earthquake, they were able to explain, with a forward model featuring a steep and sharp eastern edge (figure 3.8), how SKS around 86 degrees is delayed up to 10 seconds and becomes normal approaching 92 degrees. As for the western edge of the African low velocity structure (ALVS), *Ni et al.* [1999] have studied SKS-S crossover distance to constrain the western side of ALVS. The preliminary result from the variation of crossover distance and S, SKS travel time for epicentral distance between 83 and 105 shows that there is a low velocity layer (240 km thick or less, with shear velocity reduction about 3%) beneath the Atlantic ocean and the AVLS seems to transition sharply into an upwelling beneath western Africa.

However, the more detailed picture of the transition and the low velocity layer beneath the Atlantic can not be obtained with the data mentioned above for two reasons. On one hand, to model the low velocity layer, the differential time between S and ScS for epicentral distances larger than 87 degrees (where S raypath begins to sample the lower 300 km of the mantle) is crucial. But to measure the separation between S and ScS for the range of epicentral distances is very difficult because S and ScS approach each other and interference makes hand-picking of S and ScS arrival difficult (figure 5.1). On the other hand, to model the transition of the low velocity layer into ALVS, SKS-S differential times before crossover distances (82 degrees, figure

5.1) would be helpful since SKS and S raypaths are closer in the upper mantle, thus more sensitive to lateral variation in D". But this is difficult too, because of the interference between SKS and S around the cross-over distance. For distances of a few degrees before the crossover distance, SKS is sufficiently after S, but then it begins to interfere with ScS.

Because of difficulties mentioned above, many tomographic studies do not use the SKS data before 90 degrees and ScS+S data between 87 and 102 degrees. This is especially true for those tomographics studies that determine specific arrivals by correlating a seismic phase from data with seismic arrivals on reference synthetic seismograms because such correlation method does not provide correct result when two seismic phases interfere, just like the case of the SKS,S cross over and the emerging ScS,S. Moreover, when the epicentral distances are too large (larger than 95 degrees), the S waveform can be affected due to velocity structures (Fig 5.1b); in this case, the differential travel time itself is not sufficient to study the structure, instead, whole waveform of S and ScS modeling is necessary.

In this paper, we propose an algorithm to overcome the difficulty discussed above, and then apply the algorithm to seismograms from earthquakes in South America recorded in South Africa to compute the differential travel times. We conduct some forward modeling that fits the travel time data as well as ScS and S waveforms recorded by the South Africa Array ([*Wen*, 2001]) for epicentral distances between 84 and 95 degrees along the South America-African corridor.

5.3 Algorithm and Differential Travel Time Analysis

The interference of seismic arrivals are more common in crustal studies where different seismic arrivals are very close in timing. *Song and Helmberger* [1998] proposed a hybrid simulation method to study lateral variation in crustal velocities beneath southern California. Basically they assume unperturbed seismic raypaths from a 1D

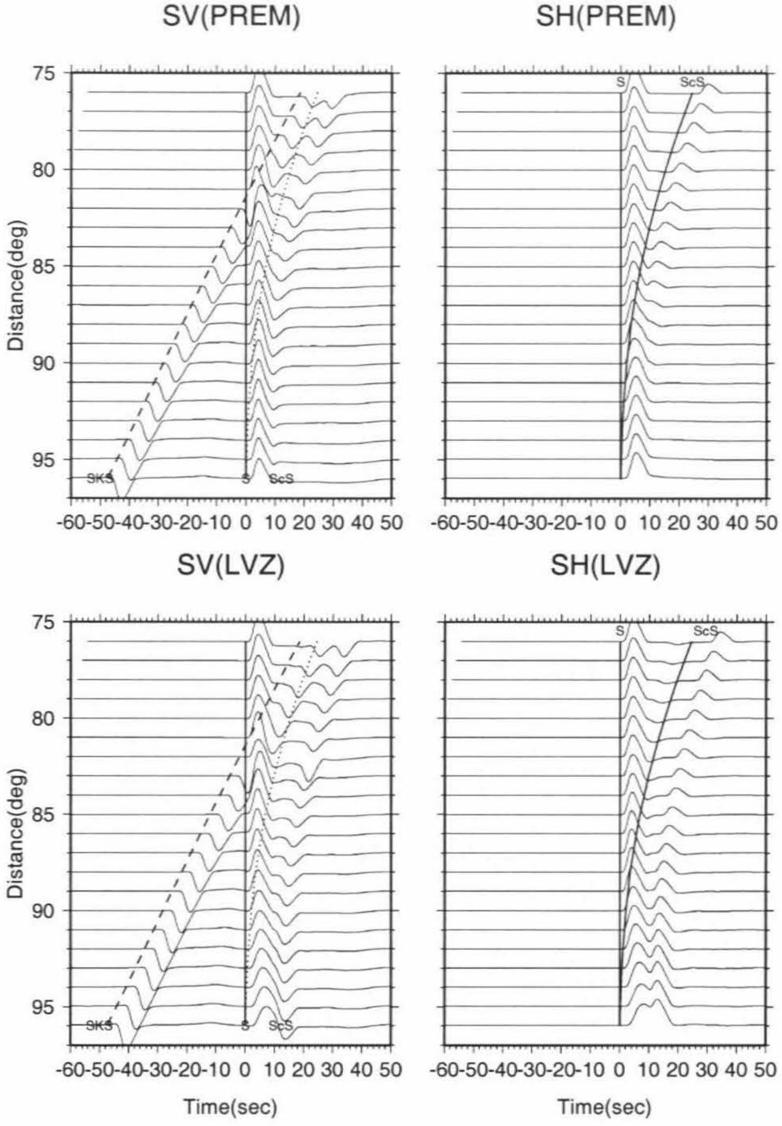

Figure 5.1: Generalized ray (GRT) Synthetic seismograms for PREM and a model with low velocity layer (LVZ) above CMB. The low velocity layer is 180 km thick, with 3% lower S velocity. (TOP) PREM synthetics. SV components are on the left, on this component SKS,S and ScS are present. Notice that SKS and ScS have opposite polarity than S. For SH component S and ScS have the same polarity. For PREM S and ScS are very close from 87 degrees on, and essentially one pulse beyond 90 degrees. SKS overruns S around 82 degrees, and becomes the first arrival. Around this distance, it hard to measure the differential time between SKS and ScS. (Bottom) LVZ synthetics. S and ScS are separated obviously up to 95 degrees. The crossover distance of SKS and S is about 2 degrees later than that of PREM. S is longer period like beyond 93 degrees due to the diffraction from the negative discontinuity of the LVZ. Diffractions effect also make S smaller than ScS for large epicentral distances.

model, apply travel time corrections or shifts for the seismic phases, then sum the shifted responses of each seismic phase to get the simulated seismogram. Observed waveforms along similar paths can then be matched and the shifts determined by simulated annealing to construct a 2D tomography model ([*Helmberger et al.*, 2001]). For small velocity perturbations, this technique works quite well when compared to regenerated synthetics and has been applied to crustal studies of Southern California. Such concepts can be directly applied to teleseismic studies where interference of different arrivals are prominent (e.g., for the case of SKS and S crossover, and S and ScS emerging) because S, SKS and ScS are associated with distinct generalized raypath: S is defined by all the rays in the mantle, not including the ray reflected from CMB, SKS is defined by all rays in the core, and ScS is defined by the ray reflected from CMB. To implement the hybrid-simulation technique, S, SKS and ScS groups are computed with GRT with their sum displayed in figure 5.1. Then each phase is shifted so as to obtain an optimal match with data. The procedure is displayed in figure 5.2. In order to compute the differential time for a seismogram at 90 degrees taken from the bottom panel of figure 5.1, first the SKS and S (both SV and SH component), ScS (both SV and SH component) are computed for a reference 1D model (PREM, in this case). Note the ScS and S have the same polarity for SH component, and SKS, ScS have opposite polarity than S on SV component. There is no SKS on SH component because of decoupling of P-SV and SH system. By delaying SKS for 2.3 seconds, ScS for 4.7 seconds, the hybrid-simulated (referred to as approximate seismogram hereafter) seismogram (light traces) matches the exact seismograms (heavy traces) quite well.

In figure 5.3, the exact seismograms from GRT are compared to approximate seismograms. Most of the exact seismograms are well matched by the approximated ones except for S and ScS phases beyond 94 degrees where the S raypath begin to sample the discontinuity of the low velocity layer, and the diffraction effect becomes more prominent and the waveforms need to be modeled directly. The differential times derived from this algorithm fits the theoretical calculation of differential times for the LVZ model quite well(figure 5.3). Thus this match argues that the hybrid-

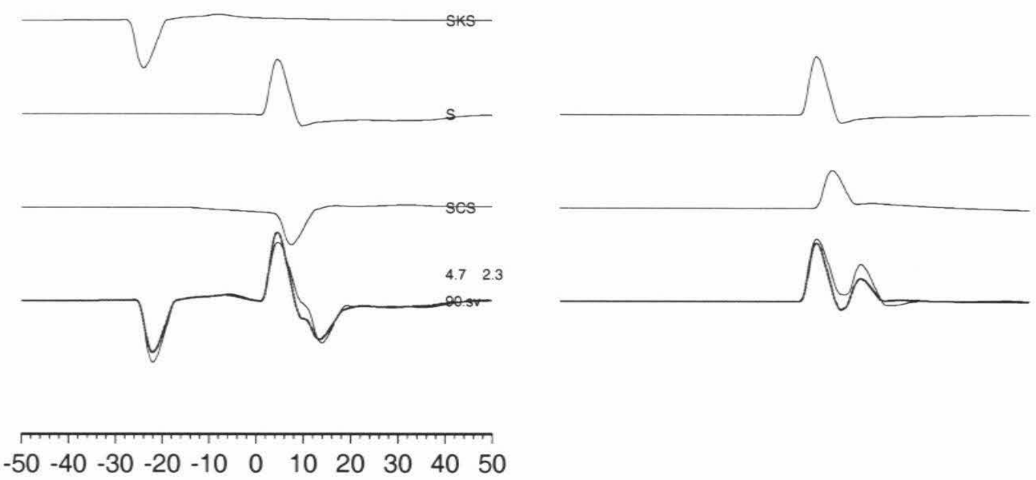

Figure 5.2: The algorithm of calculating differential time of SKS-S, ScS-S. First, synthetic seismograms for SKS, S, ScS are calculated for a 1D reference model (PREM). From the GRT point of view these phases can be calculated separately by summing up responses of outer core rays, mantle rays and ray reflected from CMB respectively. Then SKS synthetic and ScS synthetic are shifted (also with appropriate amplitude adjustment) with respect to S so as to get an optimal matching with an observed seismogram (bottom light traces). The numbers are time shifts of ScS and SKS. For this specific example, SKS is delayed 2.3 seconds and ScS is delayed 4.7 seconds.

simulation technique works well for the small velocity perturbation. In figure 5.4, we show the match between data and approximate seismograms for an earthquake recorded at station LSZ in southern Africa. The epicentral distance for the event is 89.3 degrees, where S and ScS are very close together in PREM; however, the S and ScS in this data are well separated by 12 seconds (6 seconds larger than PREM values).

The simple waveform of S, SKS, and ScS which are well matched by approximated seismograms suggests that our technique can be applied to the analysis of data routinely. The procedure works particularly well for arrays as displayed in figure 5.5, where a record section of an earthquake recorded by Namibia project (GEOFON) is modeled with the techniques. The SKS, S and ScS are very clear on each seismogram. Such a record section analysis of data helps exclude the possibility of wrong identification of seismic phases. The technique is also very useful for processing WWSSNLP seismograms where the long period instrument response makes onsets of seismic arrival less sharp and difficult to pick (figure 5.6); for example, on GRM trace (epicentral distance is 78.4 degrees), the SKS phase is matched by the approximate seismogram and would be difficult to pick the onset. This is especially true for PRE trace, where S and SKS are very close. Since WWSSN (including DWWSSN) had a long recording history (1965 upto 1988), the application of this technique will be possible for many event-station pairs and thus help to constrain the lower mantle velocity structure better.

We applied this technique to study the differential time between SKS and S, ScS-S for epicentral distances between 75 to 105 degrees. The events (Table 6.1) and the stations we used are displayed in figure 5.7. Most of the earthquakes are deep focus events (depth larger than 100km) in south America so that surface reflection phases would not contaminate the seismic phases we are interested in, and we only used southern Africa stations (both IRIS broadband stations and WWSSN stations) to study a corridor of the ALVS. The South Africa PASSCAL array which has very good coverages and recorded some high quality seismic data, that are very important in constraining the lowermost mantle velocity structure, are also included in this

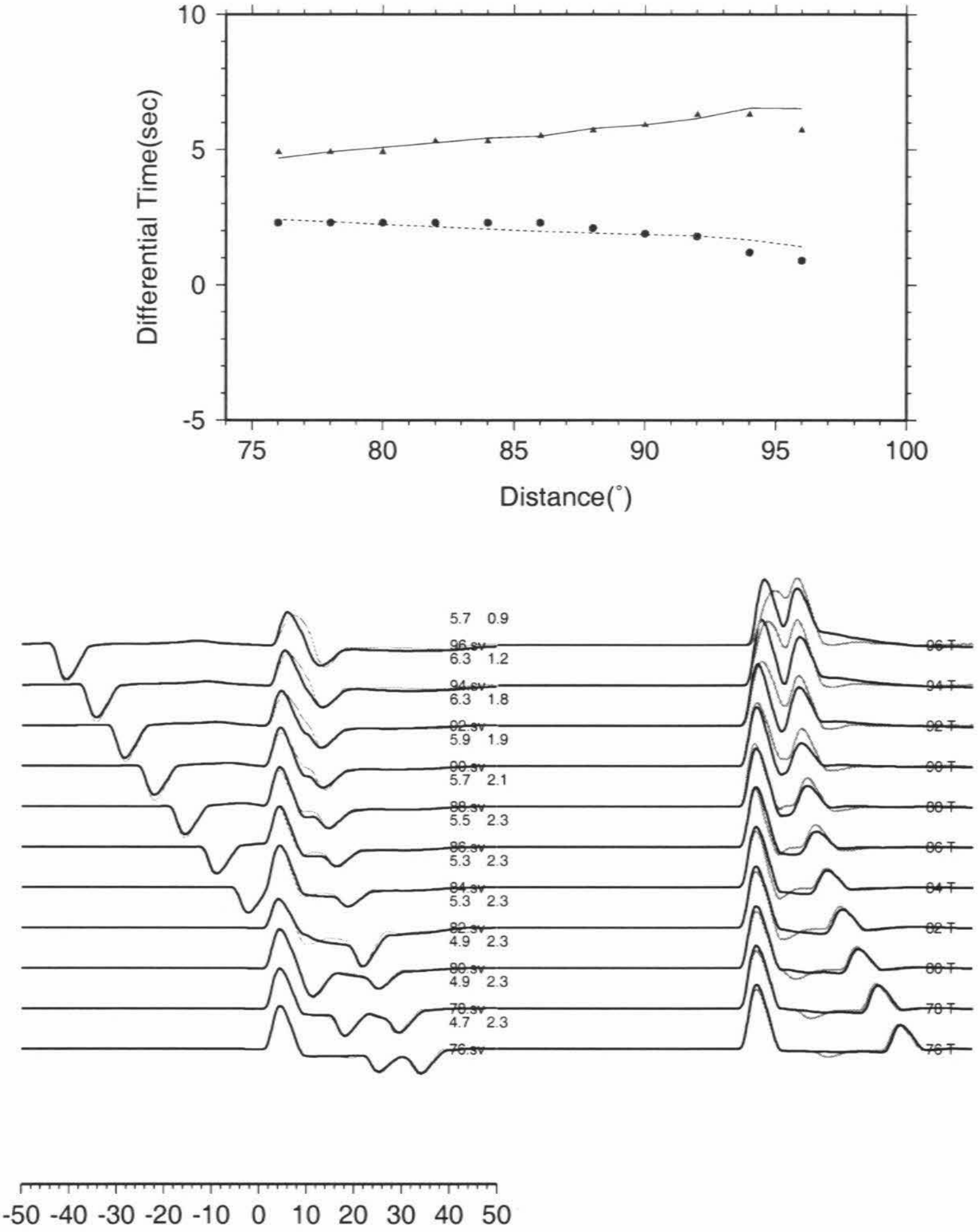

Figure 5.3: (TOP) Differential time of SKS-S and ScS obtained from approximated seismograms are plotted as dots (SKS-S) and triangles(ScS-S). They agree well with theoretical differential SKS-S (broken line) and ScS-S (solid line). Beyond 90 degrees differential time of SKS-S and ScS-S decreases because S begins to be delayed because of the LVZ. (BOTTOM) Comparison of exact seismograms (gray traces) with approximated seismograms (black traces) derived from the algorithm described in figure 5.2 . Typically they agree well except for distances larger than 92 degrees where diffraction effect is important.

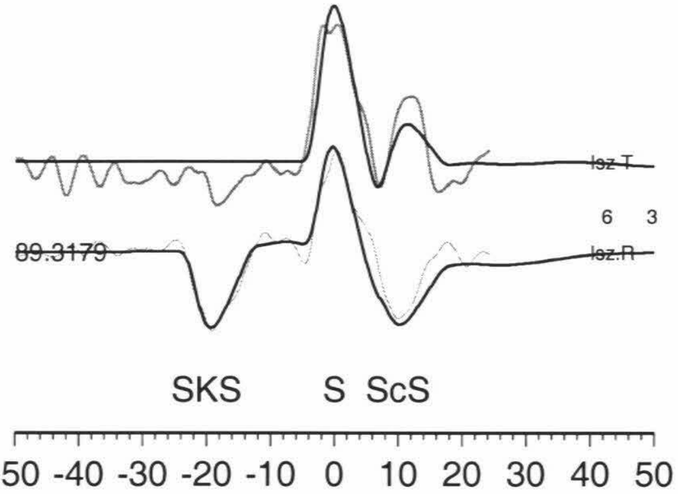

Figure 5.4: An example showing how well approximated seismogram fits data recorded at station LSZ (lsz.T is the tangential component, lsz.R is the radial component). The epicentral distance is 89.3 degrees where S and ScS would be very close together in PREM. The first arrival is SKS, the second arrival is S, and the third arrival is ScS. Notice the polarity of each arrival. After SKS is shifted 3 seconds and ScS is shifted 5.3 seconds, the match between approximated seismogram with data is optimal. Lighter traces are data.

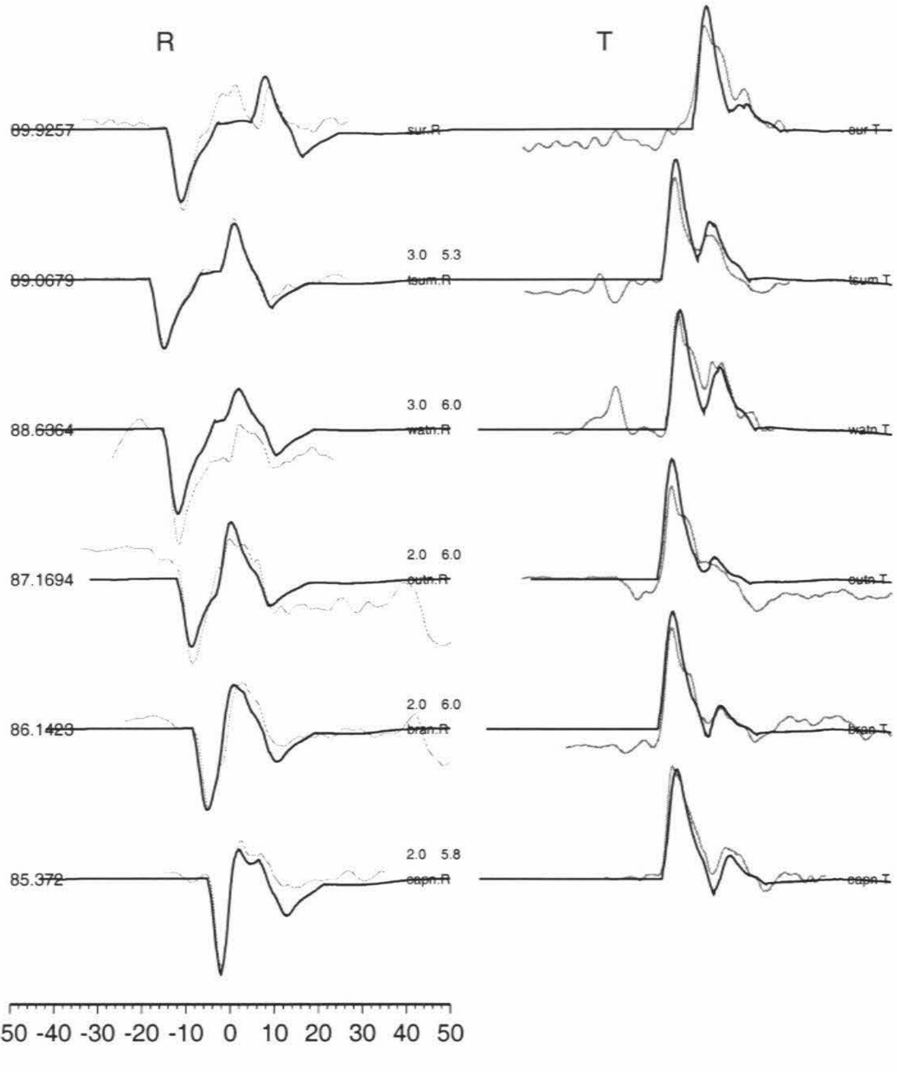

Figure 5.5: Record section of approximated seismograms and S,SKS and ScS waveforms recorded by Namibia stations. Lighter traces are data (R and T are radial and tangential components respectively). Heavy traces are synthetics.

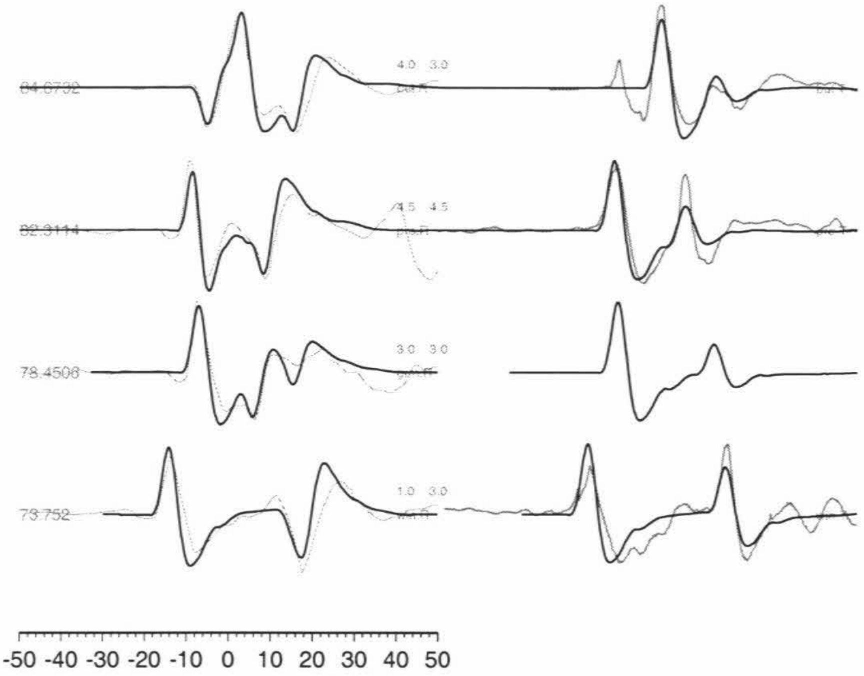

Figure 5.6: Application of approximated seismogram to analog long period seismograms (WWSSNLP). Seismograms recorded by long period instruments do not show sharp onset of seismic arrivals, thus it is difficult to pick the arrival. The problem is very severe around SKS,S crossover distances (e.g., station PRE, distance of 82 degrees).

study. We only worked on high signal to noise ratio data where S, SKS, ScS are clear and no other processing procedures are applied other than deconvolving the velocity seismograms into displacement seismograms. A typical record section of data is displayed in figure 5.8, the SKS and ScS has opposite polarity as compared to S on SV component (the heavy traces) while S and ScS have the same polarity on SH component (light traces), and this polarity relationship makes identification of these three phases quite straightforward. The obvious feature is that separation between SKS and S is a few seconds smaller than PREM predictions, and the separation between ScS and S is a few seconds larger than PREM predictions. The smaller separation between SKS and S is due to slower SKS ([*Ni et al.*, 1999]), and the larger separation between S and ScS is due to slower ScS ([*Ni and Helmberger*, 2001]). Such a technique applied to high quality data typically yields a precision about 0.3 seconds; it is hard to discern the difference between data and approximated seismogram if the specific phases are shifted by an amount smaller than 0.3 seconds. One complication might come from anisotropy in the upper mantle where SV seismograms have to be shifted to be aligned on SH phases. For the dataset we processed, the misalignment of SV and SH components due to upper mantle anisotropy is up to 1 second. But upper mantle anisotropy should not change the differential time much since on either component, each phase is affected identically due to the closeness of raypath in the upper mantle. However, the anisotropy in the D" region should affect the differential time between ScS and S. *Thomas et al.* [2000] showed that anisotropy is present in some fast D" region. Since the lowermost mantle we are studying is a low velocity layer, anisotropy might not be important. As for the differential time between ScS and S on SV component and the differential time of ScS and S on SH component that we measured in our study, they are almost identical, so we just use ScS-S to denote the differential time between ScS and S. This result is in agreement with recent studies beneath the Atlantic ([*Fuchs et al.*, 1999]).

The differential times for these earthquakes are obtained with the procedure discussed above, and can be classified into 3 groups: group 1 for station BOSA, LBTB, PRE (SLR) (figure 5.9); group 2, TSUM and WIN; group 3, LSZ, this grouping is

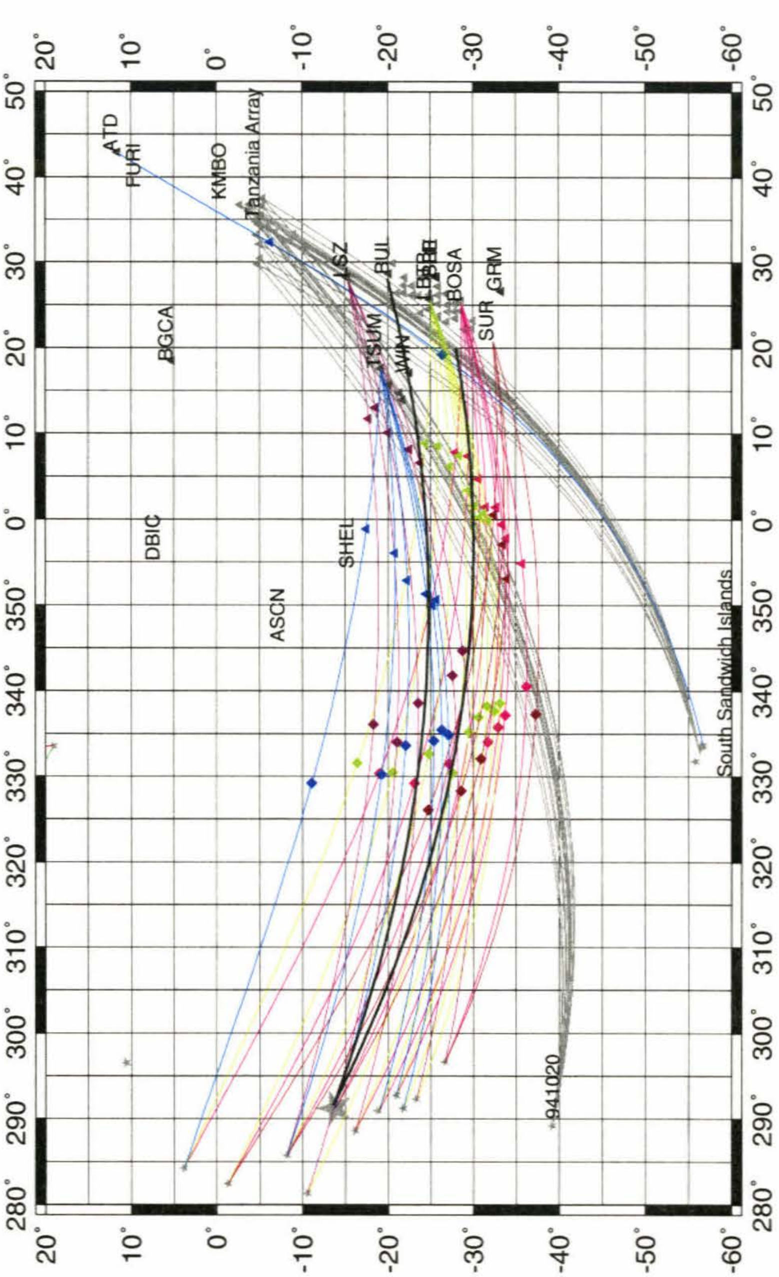

Figure 5.7: A map showing earthquakes and stations that are used in this study. The diamonds denote the bounce points of ScS on CMB along the great circle path connecting source and receiver. Triangles denote the SKS exit point on the receiver side. The data used by Ritsema et al. [1998] is also displayed to show that a different cross sections is studied in this paper. Bold lines brackets great circle paths for two events recorded by the South African array. The Tanzania and southern Africa array are plotted as gray triangles.

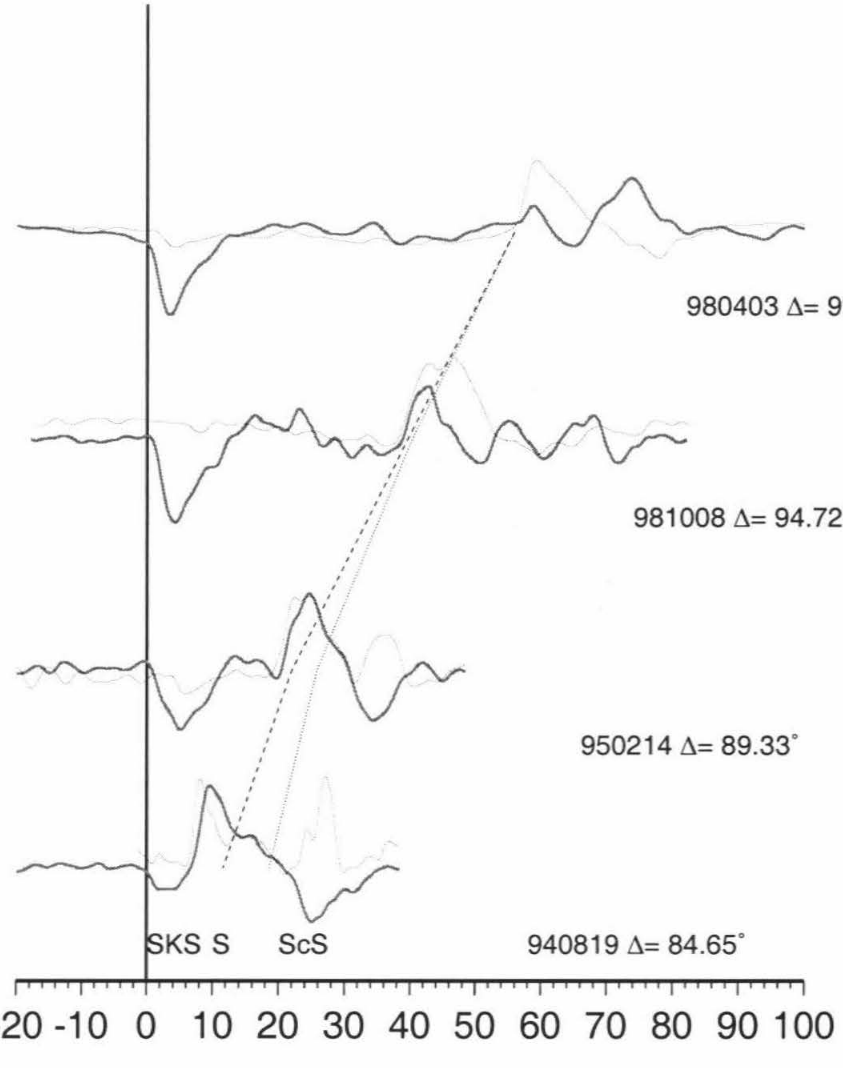

Figure 5.8: A record section of S waveforms recorded at station LSZ. Light traces are radial components, and heavy traces are tangential components. All traces are aligned on SKS arrival; and the separation between S and S is smaller than PREM predicted (dashed line), and separation between ScS and S is greater than PREM predicted (dotted lines).

based on the different behavior of differential time versus epicentral distances. Although there are some scatter in the differential time measurements (about 2 seconds), the different trends can be observed on different groups. Very few high quality data are available for station SUR and GRM, thus the data from SUR and GRM are not included in constraining forward models. As expected from SKS and S crossover studies, for group 1 and group 2, SKS-S and ScS-S vary from 1 second to 7 seconds, with 3-4 seconds as average. For group 1, SKS-S reaches 7 seconds for epicentral distances up to 102 degrees, and the SKS-S time shows some rapid increase (from 4 seconds to 7 seconds) from distance of 87 to 94 degrees. This rapid increase of differential time may suggest some rapid variation of velocity structures in the lower mantle. Assuming the low velocity structure is closer to South Africa (receiver side), it implies that the SKS raypath samples a larger portion of the ALVS for larger epicentral distance (steeper SKS raypath, closer to receiver). Around 90 degrees, the SKS exit point at CMB is about 15 degrees from the receiver, so the rapid variation of ALVS takes place about 15 degrees from station BOSA(LBTB). While for group 2, the SKS-S and ScS-S behave quite smoothly. But for group 3, the SKS-S and ScS-S decreases with larger epicentral distances, the explanation is that station LSZ (BUL) is to the east of the western edge of the ALVS, and S raypaths begin to sample more of the ALVS with larger epicentral distances (steeper S raypaths), thus S is delayed more and more, causing smaller SKS-S and ScS-S times (figure 5.12). We will discuss this feature in the next section.

The ScS-S differential time measurements beyond 85 degrees that we obtained here have never been used in modeling the lower mantle beneath Atlantic and Africa. Only with the advent of broadband stations installed in Africa, it is possible to compute the differential time between ScS and S with such accuracy. WWSSN short period instruments did not record strong ScS for such ranges of epicentral distances as discussed in chapter 2, while long period instruments recorded S and ScS as one pulse since the separation between ScS and S is about 3-5 seconds which is shorter than predominant period of WWSSNLP instruments. The low velocity layer beneath the Atlantic also separates ScS and S enough to be measured. It would be not possible

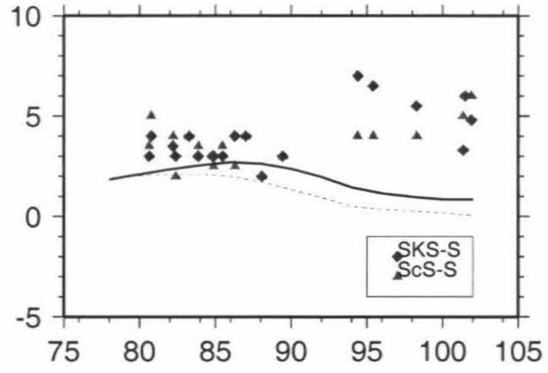

(A) BOSA,LBTB PRE

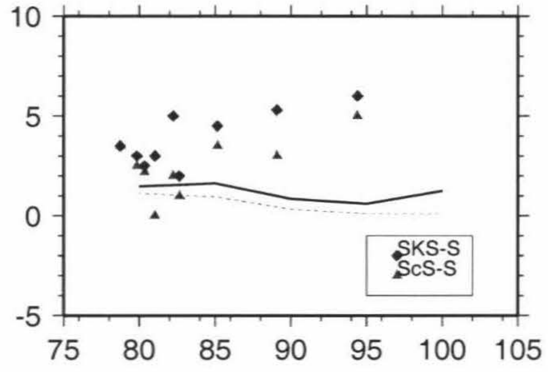

(B) TSUM and WIN

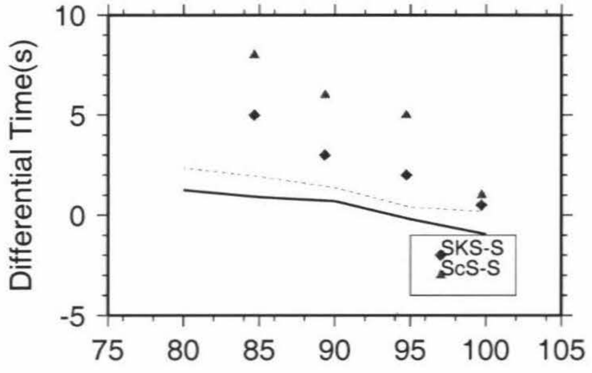

(C)LSZ . Distance(°)

Figure 5.9: The three groups of differential time measurements (SKS-S, ScS-S). Solid line is predicted SKS-S differential time from Ritsema's tomographics model, and broken line is the predicted ScS-S model. The typical SKS-S time is about 3-7 seconds, and ScS-S is about 3-5 seconds. (A) result for station BOSA, LBTB, PRE (B) station TSUM,WIN (C) station LSZ. Notice that SKS-S time increases from 3 seconds to 7 seconds with larger distances for group (A) while the trend is opposite for group (C).

to model ScS in this distance range for faster or normal D" region where S and ScS are interfering. For ScS to be robust, the velocity structure close to the ScS bounce points must not contain substantial scatterers which tend to diminish ScS ([*Cormier et al.*, 2000]). With the installation of broadband seismic array in southern Africa, the unique opportunity of studying the lowermost mantle beneath the Atlantic in detail becomes possible.

We also calculated SKS-S and ScS-S time for a tomographic model ([*Ritsema et al.*, 1999]) and attempt to fit these observed data (figure 5.9). This tomographic model predicts SKS-S and ScS-S differential time with a maximum of 3 seconds and 1.5 seconds average delay, substantially smaller than observed value, but with similar trend. This suggests that the tomographic studies may reflect the same velocity structures as that control the SKS-S and ScS-S trends. However, tomographic inversion tend to diffuse sharp structures given the long period data used in such studies ([*Ni and Helmberger*, 2001]). Thus one does not have good constraints on rapid lateral variation in tomographic model Since such studies do not include differential time of SKS and S around cross-over distance and of ScS and S for emerging distances (larger than 90 degrees).

5.4 Waveform Constraints

While the differential times assembled above are quite important in establishing a reliable model, they prove insufficient in number to generate a useful tomographic models. Thus we examined the synthetic predictions from a number of existing tomographic models to generate a working 2D section. An example of such a tangential profile generated from the model by *Ritsema et al.* [1999] is displayed in figure 5.10, labeled as SH(Tomo). The maximum delay of ScS relative to PREM is only 3 seconds which is obviously insufficient to fit the data. However, the S-arrival delay with distance observed on synthetics shows the same general trend with S becoming delayed with range, roughly by 6 seconds as observed on data. Thus we will simply start increasing the velocity contrast until we improve the waveform predictions. Then, we

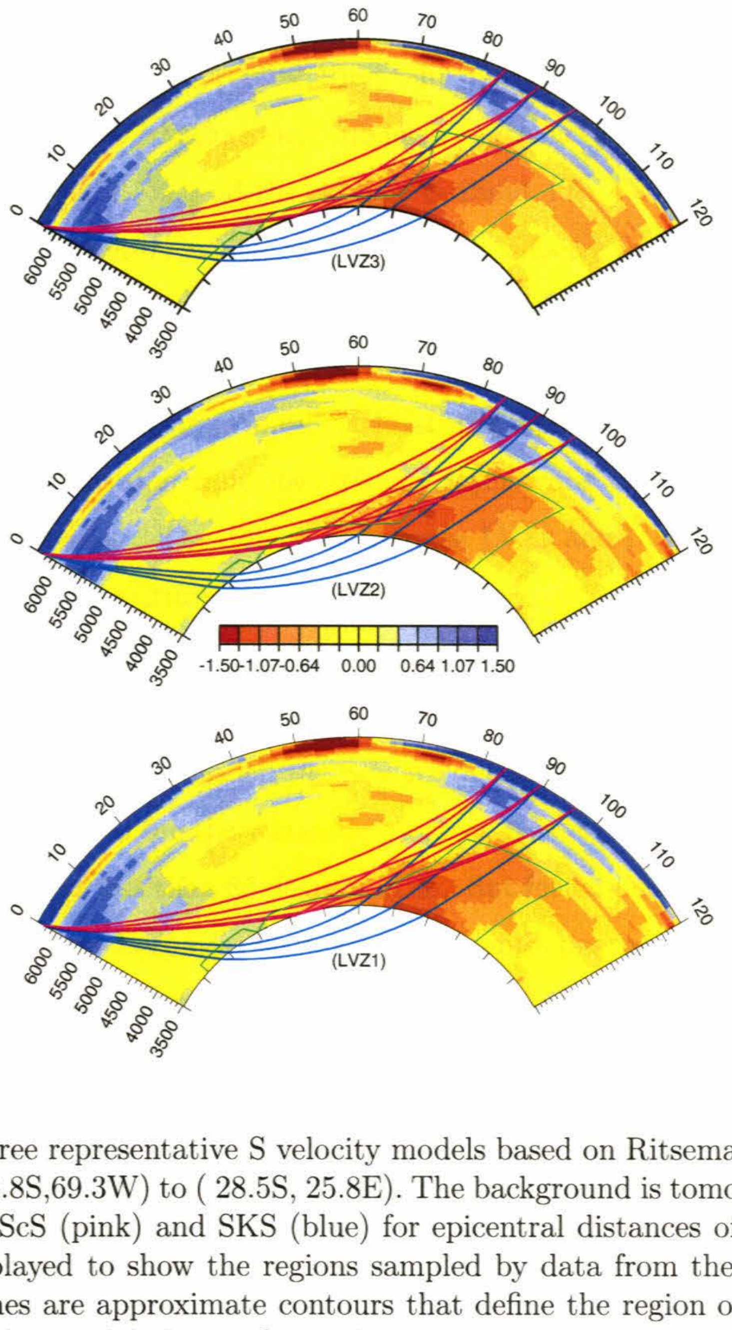

Figure 5.10: Three representative S velocity models based on Ritsema's tomographic models from (13.8S,69.3W) to (28.5S, 25.8E). The background is tomographic model. Raypaths of S, ScS (pink) and SKS (blue) for epicentral distances of 84, 89 and 94 degrees are displayed to show the regions sampled by data from the South African array. Green lines are approximate contours that define the region of slow anomaly in the tomographic model. In our forward modeling, we set the velocity anomaly to -3% in the region enclosed by green lines. LVZ1 features slow transition from slow velocity layer to African upwelling while the transition in LVZ2 and LVZ3 are quite sharp. LVZ3 features a plume head structure. The typical velocity anomaly is about -1% in this cross section of the tomographic model.

will go back and use this new model to check the differential time data.

The method of modifying tomographic models is very similar to those used in previous chapters, which is basically to inflate velocity perturbation in certain region so as to explain the large differential time. In figure 5.10, three velocity models are displayed. The colored background model is Ritsemas's model, with maximum velocity anomaly about 1.5%, and the average is about 1%. We developed the three models by drawing a contour which defines the low velocity region (the green line), and we set the velocity perturbation to be 3% slower in the region enclosed by the green lines. Given the diffused nature of the tomographic models, the edge of the low velocity region is not clear. We only tried three representative models; LVZ1 is a model with slow transition from low velocity layer while the transition in model LVZ2 and LVZ3 is sharper. The difference between LVZ2 and LVZ3 is that LVZ3 has more of a plume head structure.

We computed 2D synthetic seismograms for the original tomographic model and the three variant models. The synthetics were shown earlier in figure 5.11. For the unenhanced tomographic model, the ScS are delayed about 3 seconds around 85 degrees which is expected for the tomography since it is constrained with ScS data for epicentral distances less than 85 degrees or so. But for larger epicentral distances, the S and ScS essentially becomes one pulse on the synthetics, and this does not agree with the data which shows large separation between S and ScS up to 95 degrees. For the three enhanced models, ScS are always delayed due to the low velocity layers. However, for model LVZ1, because of the slow transition from low velocity layer to ALVS, the ScS for larger epicentral distances (larger than 92 degrees) samples an effectively thicker low velocity layer, thus ScS is delayed too much as compared to the data. With the sharp transition, synthetics for model LVZ2 and LVZ3 both fit the data quite well, and this is reasonable since the S and ScS raypaths in the upper mantle (where the plume head is) are very close.

The sharp transition is also favored by differential travel time data as displayed in figure 5.12, where the predicted differential travel times from model LVZ2 are overlaid with observed data, the increasing SKS-S in group (A) is fairly well fit. One noticeable

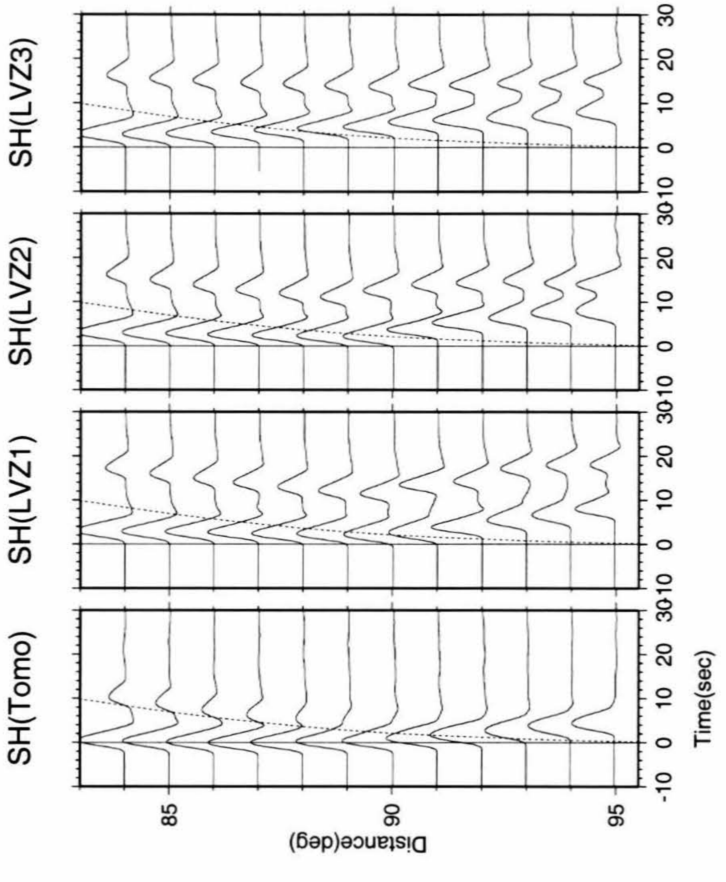

Figure 5.11: Data and 2D synthetics (Ni et al [2000]) for various models. Plots are aligned on the S arrival of PREM, and the broken line shows the predicted ScS arrival of PREM. (Tomo) Synthetics based on Ritsema's model. The ScS is delayed about 3 second around 85 degrees, but ScS and S are too close after 90 degrees. (LVZ1) Synthetics based on model LVZ1, ScS and S is too much separated as compared with the South Africa Array Data (Wen, 2001). The slow transition from low velocity layer to ALVS in model LVZ1 delayed ScS too much. (LVZ2 and LVZ3) Synthetics based on model LVZ2 and LVZ3. The separation between S and ScS are similar to that on data.

feature for group (C) (station LSZ) is that model LVZ2 predicts decreased SKS-S and ScS-S just as the data shows, and the predicted S travel time is increasingly delayed because the S raypath does not sample the ALVS for small epicentral distances, and S raypath samples a larger and larger portion of the ALVS with increasing distances. Events from Sandwich Island recorded at LSZ (epicentral distance about 60 degrees) show very delayed ScS (up to 12 seconds), and this also supports the idea that raypaths with small takeoff angle sample the bulk of the low velocity anomaly. A record section of synthetic seismograms for sources at different distances from station LSZ is compared to data observed at LSZ (figure 5.14); the large separation of ScS and S at the distance of about 85 degrees and the diminishing separation around 100 degrees is reproduced by synthetics. So model LVZ2 can explain record section of data with fixed source and varying station as well as explain record section of data with fixed station and varying sources. The geometry of fixed stations provides the advantage of modeling the lateral variation of station side velocity structure with more details, if assuming receiver side is normal.

5.5 Discussion and Conclusion

We have developed an algorithm to measure the differential time between SKS and S around crossover distance as well as the time between ScS and S for large epicentral distances. For the earthquakes from South America recorded by southern African stations, SKS and ScS are 3-7 seconds later than S with respect to PREM, which suggests a large scale low velocity structure beneath Atlantic and Africa. Such low velocity structure may also be responsible for S waveform distortion beyond 90 degrees. The high quality broadband data, especially the dense array data used in this study, combined with the seismic phases in certain ranges of distances that are not available in other studies, provided much more constraints on the velocity structures. We developed a forward model that both explains the travel time variation and waveform anomalies. Our model features a relatively flat low velocity layer (3% slower in S velocity, 200 km thick) beneath Atlantic, and then it transitions into the African

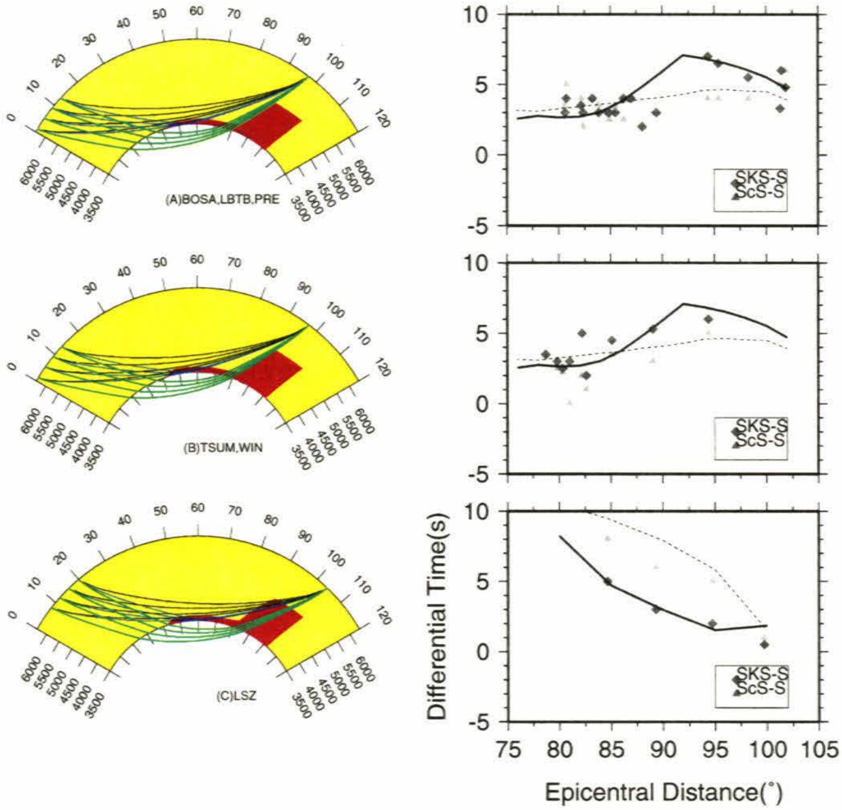

Figure 5.12: Predicted differential time from model LVZ2. Solid lines are SKS-S time; broken line, ScS-S. The stations (LSZ, TSUM and BOSA) are at different positions with respect to the structure (red region, 3% lower S velocity), thus sample different part of ALVS. For station LSZ, ScS and SKS are in the slow region for all distances, while S samples more of the anomaly with increasing distances, leading to smaller SKS-S and ScS-S. ScS samples both the bulk of ALVS and the low velocity layer, thus ScS-S is very large (6 seconds) around 85 degrees. For station TSUM and BOSA, S raypaths are not in the anomalous region , while SKS raypaths samples more of the slow anomaly with increasing distances, thus leading to increasing SKS-S. For these two groups of stations, ScS only sample the low velocity layer, thus is only moderately delayed 3-4 seconds.

upwelling (1500 km high above CMB, also with 3% lower S velocity). The transition is relatively sharp, which is required by S and ScS waveforms recorded by the south Africa array. Such a sharp transition agrees with previous studies ([*Ritsema et al.*, 1998a; *Ni et al.*, 1999]) based on data from other azimuth or different dataset, and some geodynamical modeling also predicts relatively sharp transition ([*Sidorin et al.*, 1999; *Bergeron et al.*, 2000]). The flat low velocity layer beneath Altantic is also present in Grand's model([*Grand*, 1994]) which is derived from shorter period data than other tomographic studies.

As the velocity structure (velocity jump) of the fast D" causes S triplication, the low velocity layer can produce diffraction effects on S waveform. Either the triplication or the diffraction makes waveform modeling an important technique in studying the radial gradient of the velocity structure in the lower most mantle which is less sensitive to travel time modeling. It seems that the low velocity layer, or a negative gradient just above CMB, also make CMB-diffracted waves (Pdiff, Sdiff) propagates to longer distances than PREM would predict ([*Wysession et al.*, 1995]). A recent survey of PcP precursors from stacking of the dense JARRAY short period data for Fiji events ([*Kito and Krueger*, 2001]) also requires negative discontinuity (-1% lower P velocity, 240 km above CMB) beneath Pacific. If we adopt *Berryman* [2000]'s theory of 3 to 1 ratio of S and P velocity perturbation from mineralogical considerations, our models of 3% S velocity reduction will agree their P velocity models.

The eastern edge of ALVS is not well modeled in this study due to lack of coverage of seismic rays sampling the edge. Previous studies based on S and S-SKS travel times show that the eastern edge is sharp ([*Ritsema et al.*, 1998a]). Waveform data and SKKS-SKS travels time also provide more evidence to support this feature. For the event 941020 recorded by Tanzania array, S-SKS is up to 15 seconds later (compared with PREM), and SKKS-S is late up to 7 seconds (figure 5.14). The interesting feature is the large S-SKS and SKKS-SKS differential travel time beyond 98 degrees, the interpretation is that SKS raypath begin to miss ALVS beyond 98 degrees which leads to larger S-SKS and SKKS-SKS time. SKKS and SKS raypaths are very close, the 7 seconds separation argues for rapid variation of velocity structure. Such sharp

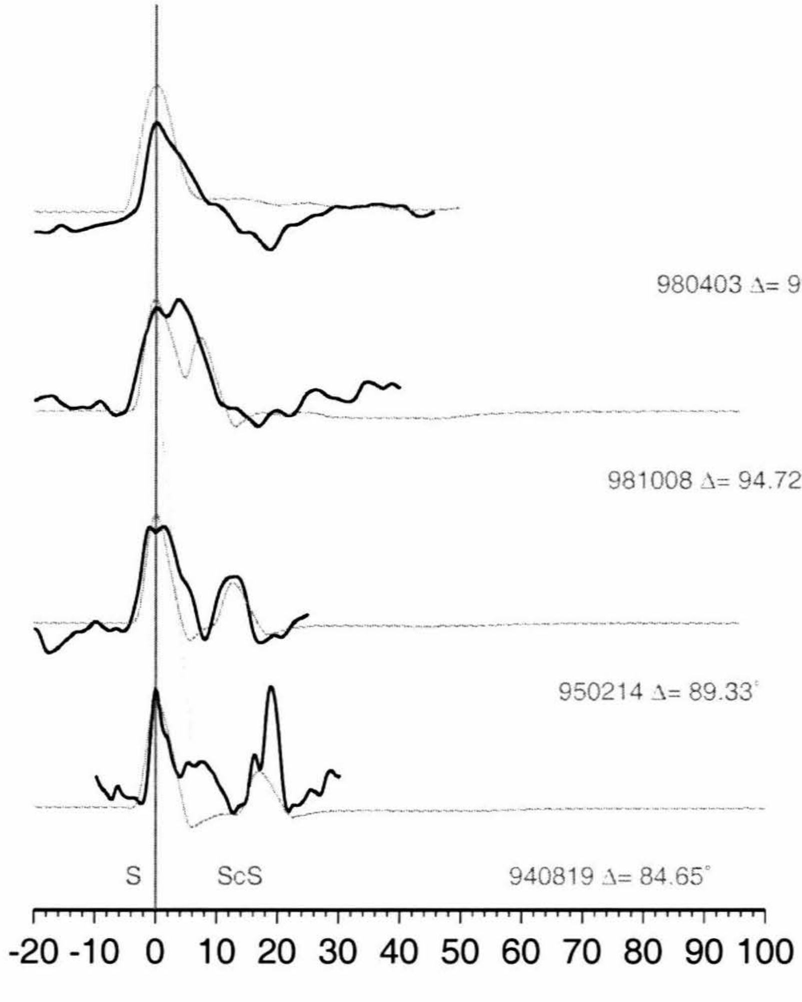

Figure 5.13: Comparison of data (light traces) at LSZ and synthetics (heavy traces). All traces are aligned on S arrival; the curve denotes ScS-S differential time for PREM. It is obvious that ScS is very delayed (with respect to S) around 85 degrees; but it is close to S around 100 degrees. The synthetics based on model LVZ2 reproduce this trend.

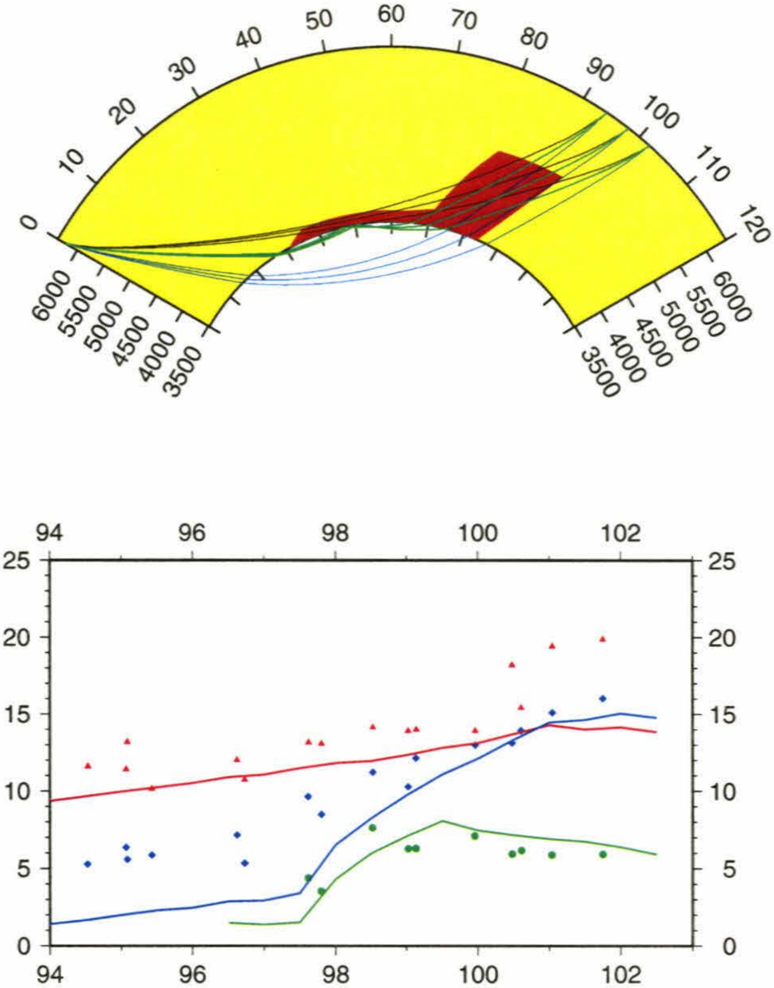

Figure 5.14: The travel time constraints on the eastern edge of ALVS from S, SKS and SKKS. (Top) Raypaths of S (black) , SKS (blue) and SKKS (green) and ALVS. The general feature is that S is delayed for the all range of distances, SKS begins to miss the structure around 98 degrees. (Bottom) Predicted travel times for the model. Red line is S travel time, Green line is SKKS-SKS time, and blue line is S-SKS time. Because SKS misses ALVS around 98 degrees, SKKS-SKS and S-SKS time begin to increase rapidly with distance. The triangles , diamonds and circles are observed S, S-SKS, SKKS-S time respectively.

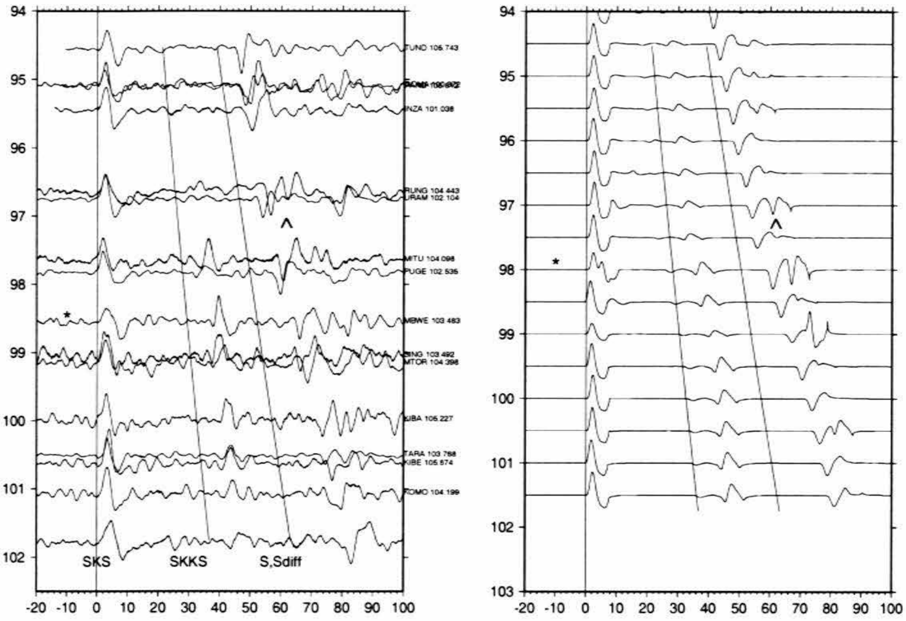

Figure 5.15: Observed waveform (left) and WKM synthetics (right) for the model displayed in figure 5.14. Note the complicated SKS waveform around 98 degrees as marked by (*) in data, this feature is somehow simulated with synthetics (also marked by *). The S waveforms in data also behave not consistently, some have two pulses (marked by $\hat{)}$, some only one pulse. This feature is also reflected in synthetics. This complicated waveforms suggest sharp boundaries.

edges would produce waveform anomalies too because WKM synthetics rely on summation of neighbouring raypaths some of which are in the anomalous region (leading to later arrival) while the others are outside of the region (thus earlier arrival), and this double peaks are observed on waveform data as displayed in figure 5.15. The SKS waveforms around 98 degrees are fatter or show double peaks, this is reproduced by synthetics based on the model in figure 5.14. This is only a preliminary result, more detailed forward modeling will be conducted in the feature combined with other array waveform data.

We have only studied a narrow corridor of the ALVS; much effort should be directed to study the 3D structure as suggested from various tomographic models. Data from north Africa also show strong azimuthal variation of SKS and S differential times (from -5s to 5s), but more stations are needed to address the 3D issue. The ongoing MIDSEA project ([*Van der Lee et al.*, 1999]) and XI PASSCAL project would produce much more valuable data in studying this problem. For Sandwich Island earthquakes, the epicentral distances to these two arrays are also around crossover distances or ScS,S emerging distances, our algorithm of dealing SKS, ScS and S for this range of distances would be directly applicable to the dataset.

In summary, with the availability of more broadband data from increasing numbers of digital stations in Africa, combined with our 2D WKM code, we will have much better understanding of the African velocity structure which, in turn, will help to unravel the dynamics and the evolution of our planet earth.

Chapter 6 Modeling PKP Precursor with WKM

6.1 Abstract

Recent studies of the core-mantle boundary (CMB) have revealed some very anomalous structures interpreted in terms of ultra low velocity zones (ULVZ). However, there remains considerable uncertainties about their physical descriptions or even if they occur above or below the CMB. They have only been detected in isolated situations using rather special techniques; these include: distortions in SKS with the development of SKPdS and SPdKS, broadband PKP precursors, distinct ScS and S beyond 100 degrees, and rapid changes in differential travel times of neighboring phases. Here we report on a situation where raypaths associated with PKP precursors and SKPdS sample the same ULVZ structure. The structure lies beneath central Africa and has been detected from WWSSN analog data (SKPdS) discussed previously. This data set has been enhanced with a collection of digital records sampling an elongated North-South zone roughly 800 km long. The entire SKPdS data set can be modeled with a ridge-shaped cross section with widths of 250 to 400 km and drops in P and S velocity of 10 and 30 percent. Fortunately, a new IRIS station (MSKU) located in Western Africa provided excellent PKP data from the New Britain Region events sampling the above structure. The PKP and strong precursors can be modeled by 2D synthetics generated from the same structure (used in modeling SKP_dS) which provides a strong constraint on the definition characteristics of this particular ULVZ.

6.2 Introduction

Ultra-low velocity zones (ULVZ) at the core-mantle-boundary (CMB) are probably the most anomalous structure in the mantle with S velocity reduced up to 30% and P wave velocity up to 10% [*Garnero and Helmberger*, 1998b] . The initial studies on the mid-Pacific structure involved the detection of precursors to PcP [*Mori and Helmberger*, 1995], followed by studies on the interference of the two diffracted P-phases (SP$_d$KS, source-side) and (SKP$_d$S, receiver-side) with the parent phase SKS near 110° as displayed in figure 6.1 [*Garnero and Helmberger*, 1996]. The relative strength and arrival time separation between SKS and SKP$_d$S are sensitive to the velocity structure near the CMB, and modeled with a slow thin layer. Subsequent efforts has allowed us to differentiate between SP$_d$KS and SKP$_d$S as the principal cause of the interference and 2D synthetics generated accordingly [*Wen and Helmberger*, 1998a]. In particular, ULVZ's beneath Iceland and Africa have been modeled with ridge-like structures with a cross section dimension of about 200 km and with heights from 40 to 60 km [*Helmberger et al.*, 2000]. *Wen and Helmberger* [1998b], *Thomas et al.* [1999] noted that some PKP precursors (figure 6.1) contain long-period energy which could be modeled by placing ULVZ at appropriate locations at the CMB. Again, 2D domes of comparable dimensions to the above proved effective. As for short period PKP precursors, *Vidale and Hedlin* [1998] interpreted the strong precursors recorded at NORSAR array from earthquakes around Fiji as scattering from localized partial melts above CMB, and the P velocity variation is about 13% which they interpreted as an ULVZ. Comparable results of strong scattering have been produced from numerical simulations by *Cormier* [1999]. Other small scale modeling techniques include PcP and ScS interference [*Revenaugh and Meyer*, 1997] [*Cormier*, 2000], SKS and S differential times [*Breger and Romanowicz*, 1998], and SV-SH polarization [*Lay and Garnero*, 1997]. Recently, *Ni and Helmberger* [2001] modeled the large separation (more than 5 seconds) between S and ScS for epicentral distances beyond 100 degrees; their model contains an ULVZ beneath the Southern Atlantic Ocean.

A global map containing a combination of ULVZ and LVZ regions has been at-

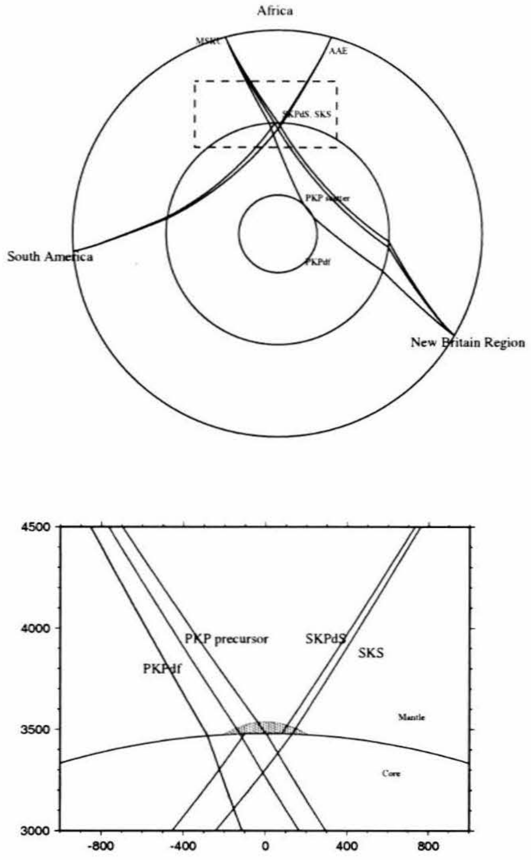

Figure 6.1: The upper plot displays the raypaths associated with studies of the ULVZ at the core-mantle-boundary (CMB). SKS phases from deep South American events to the African station AAE show distortions caused by the P-diffraction, SKP_dS, which travels along the CMB as indicated, [*Garnero et al.*, 1993]. The range where this interference occurs and the severity is controlled by the local CMB structure (lower plot). Note that the two raypaths propagating through the mantle are nearly identical, thus eliminating other complexities. Strong precursors to PKP have been successfully modeled with ULVZ's for path encountering the mid-Pacific upwelling. Here we examine paths from the New Britain Region to the African station MSKU which show such anomalous features.

tempted by *Garnero et al.* [1998]. However, each of these regions is modeled with only one technique; thus, considerable ambiguity exists between velocity reduction versus thickness. The introduction of horizonal dimensions (2D structures) produces still more ambiguity as discussed in *Helmberger et al.* [2000]. Unfortunately, these very localized features require the seismic stations and earthquakes to have precise geometries for sampling as displayed in figure 6.1. Fortunately, with increasing number of broadband stations, modeling of ULVZ with combined techniques is becoming possible. Here, we extend the earlier study of the ULVZ structure situated beneath central Africa by *Helmberger et al.* [2000] (included as appendix), referred to as Part 1 by adding more broadband SKP$_d$ S and PKP observations sampling the same region.

6.3 Waveform Data and Analysis

The IRIS stations and events used are displayed in figure 6.2a. The South American events produced the SKP$_d$S phases and the three PKP precursors were generated by the New Britain events. The raypath surface projections are indicated along with the CMB sampling segments; see Table 6.1 for source details. SKP$_d$S waveforms are presented in figure 6.2b with peaks aligned on SKS. The predicted SKP$_d$S (arrival time) by PREM [*Dziewonski and Anderson*, 1981] relative to SKS is indicated by the dotted line and that is expected from an ULVZ by the dashed line [*Garnero and Helmberger*, 1998b]. Note that we have color coded the observations associated with the particular station paths to emphasize the contrast in waveform differences. Essentially, the reduced P-wave velocity shifts the critical angle of the reflected S-to-P phase to shorter distances which moves the SKP$_d$S onset from 108° (PREM) to about 105° (ULVZ) as displayed [*Helmberger et al.*, 1996a]. The strength of the SKP$_d$S phase is strongly controlled by the shape and the precise ULVZ position [*Wen and Helmberger*, 1998a]. The black traces observed at KMBO are the simplest and align roughly along the PREM predictions, although the SKP$_d$S strength at 114.8° is anomalously strong. The observations at FURI (red) show a strong SKP$_d$S starting at 109° and remain prominent over all distances. The arrival time is about 2 secs late and agrees with the ULVZ timing prediction observed from Part 1. Note that we have included an analog AAE record (dotted red) at 112.3° from that study as a reference. The FURI waveforms show complexity about three degrees earlier than ATD waveforms (Green). The differential behavior of these waveforms at FURI relative to ATD requires very localized velocity structure. Since the western boundary of the ULVZ appears to be further away from ATD, perhaps the difference is caused by geometry. A schematic picture to explain the different waveform complexity at AAE and ATD is displayed in figure 6.2c. For FURI, the SKP$_d$S segments sample the ULVZ for distances from 109 to 115, while for ATD, which is about 5 degrees to the east of FURI, the SKP$_d$S path does not sample the ULVZ for epicentral distances less than about 109°. However, with increasing distances, the longer SKP$_d$S segments begin to sample the ULVZ and complicate the waveforms as displayed. From Part 1, this ULVZ is about 240 km across and 60 km high, with S velocity reductions of about 30% and P velocity drops of 10%. We have included the SKP$_d$S segments from Part 1 as dotted lines in figure 6.2d. Most of the analog data observed at AAE (same location as FURI) yield results similar to that seen at FURI in figure 6.2b. Note that AAE has been modeled in Part 1. Also included are segments appropriate for an array of stations in Tanzania. This data is a mixture of normal looking records (PREM-like) to anomalous for a few of the most western stations, which look similar to event 10 for KMBO. We have denoted these as dotted red as some mixture of LVZ and ULVZ structure, Part 1. If such ULVZ exists at this location as claimed above, it should produce obvious effects on the PKP precursor broadband waveforms [*Wen and Helmberger*, 1998b].

6.4 Modeling Broadband PKP Precursors

We chose two IRIS stations, MSKU and DBIC, in figure 6.2a to study the PKP core phases in the vicinity of the proposed ULVZ. The paths to DBIC are thought to be sampling PREM-like lower mantle conditions [*Ritsema et al.*, 1999] [*Ni et al.*, 1999] and can be used to establish the source characteristics. Station MSKU is at

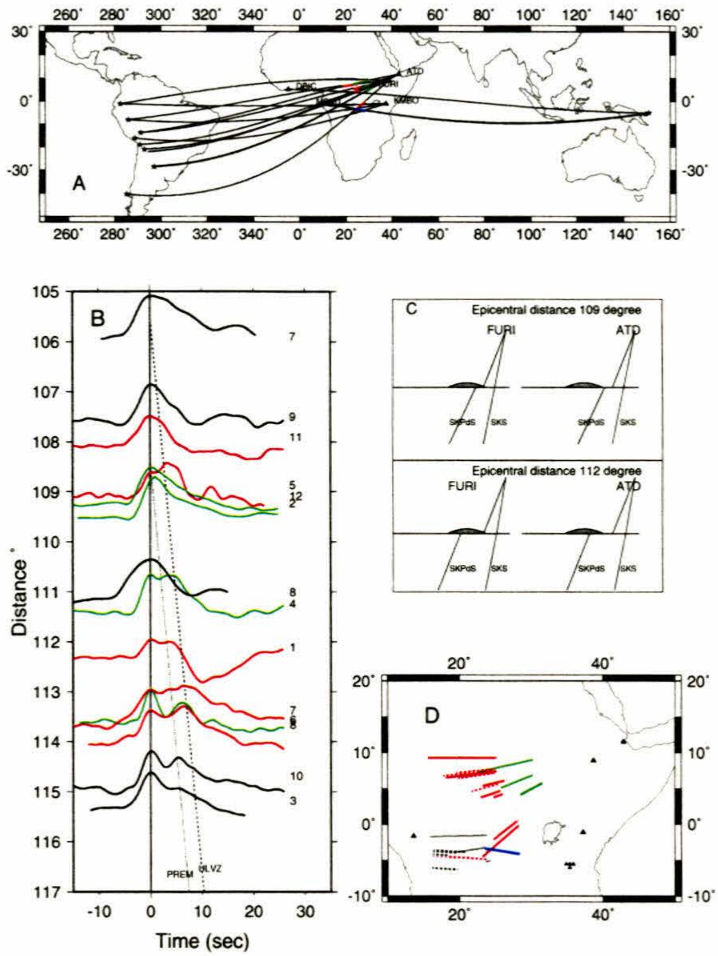

Figure 6.2: A map of the region sampled is given in (A) along with raypaths sampling the CMB. The SKS + SKP$_d$S observations (B); where black (KMBO) appears PREM-like falling on the PREM travel time predictions, red (FURI) displays a strong SKP$_d$S phase which is delayed in time (dotted, ULVZ), and ATD in green, which appears PREM-like at the ranges less than 110° and anomalous beyond. The dotted red is taken from Part 1 (AAE) where it was successfully modeled with an ULVZ structure. The numbers indicate the South American events producing these seismograms as listed in Table 6.1. The geometry in C appears to explain the delayed complexity of ATD with simple behaviors at the smaller ranges (109°). The map shown in D summarizes the anomalous CMB segments (red and green) and normal (black). The dotted traces are from Part 1. The blue segments are from PKP precursors sampling the elongated ULVZ structure (as roughly bracketed). The stenciled area is taken from *Hedlin and Shearer* [2000] indicating the position of strongest scatterers observed beneath the African region.

Table 6.1: Events used in this study

No	date	time	lat(○)	lon(○)	depth(km)
1	941020	01:15:16	-39.19	-70.80	164
2	940819	10:02:51	-26.65	-63.38	565
3	980729	07:14:24	-32.31	-71.29	51
4	970902	12:13:22	3.85	-75.75	199
5	971028	06:15:17	-4.37	-76.60	112
6	971128	22:53:41	-13.74	-68.79	586
7	981008	04:51:42	-16.12	-71.40	136
8	991130	04:01:53	-18.78	-69.05	127
9	970123	02:15:22	-22.00	-65.72	276
10	950923	22:31:58	-10.53	-78.70	73
11	950208	18:40:25	4.16	-76.64	69
12	971015	01:03:33	-30.93	-71.22	58
13	980403	22:01:48	-8.15	-74.24	164
14	990403	06:17:18	-16.66	-72.66	87
15	990525	16:42:05	-27.93	-66.93	169
16	950214	15:53:56	-23.29	-67.70	156
17	941212	07:41:55	-17.50	-69.65	151

the right geometry with epicentral distances between 134 to 137°, to observe PKP precursors as introduced in figure 6.1. With the source defined from modeling DBIC, we will attribute complexities at MSKU as caused by the CMB crossing zone at the receiver, and consider justification later. The broadband observations of three events are displayed in the upper portion of figure 6.3. The sources were chosen to be impulsive (simple) with parameters given in Table 6.1. At a distance of 155° (DBIC), the PKP branches are well separated into DF, BC, and AB denoting paths through the inner core, fluid core, and outer fluid core. The phase AB should be phase-shifted by 90° since it is a maximum arrival phase, whereas the DF and BC phases are expected to have similar waveforms with the pulse duration representing the source characteristics. This feature is particularly apparent in the middle column (990510). The synthetics were generated with a 2D WKM code [*Ni et al.*, 2000], and fit the data quite well. The observed pulses after AB are probably the surface reflections of pPKP which have not been included in the synthetics. Using these source determinations, we generated the DF predictions at MSKU ($\Delta = 136°$) where the two PKP branches, PKIKP and PkiKP, arrive with nearly identical times. The fits are excellent, but simple models will not generate precursors without adding scattering. The synthetic precursors displayed here are based on a 2D dome structure, 240 km across, 60 km, and 10% lower P velocity, and located where the SKS/SKP$_d$S modeling predicts; see figure 6.2D (blue lines).

A comparison of one of these synthetics with those from a PREM model is presented in figure 6.4 along with some of the details in their construction. As discussed in *Ni et al.* [2000] and *Helmberger et al.* [1996b], we can construct synthetics by summing generated rays (GRT) sampling various depths. We arbitrarily divided-up the core into 10 km layers and display the responses produced by summing these in groups of ten representing energy contributions from 100 km intervals, figure 6.4. The solid traces are appropriate for PREM and the dotted are from the 2D structure. Note that the various traces seem to produce only a smooth long-period diffraction in the PREM model, which is well known [*Cormier and Richards*, 1977]. The ULVZ model disrupts the delicate timing and produces the broadband precursor.

Record sections of synthetics based on PREM and dome like ULVZ model are displayed in figure 6.5 and 6.6 respectively. For PREM, the precursor (visible from 130 degrees on, until 144 degrees where PKP triplication begins) is very smooth. For the dome-like ULVZ model, the precursor has some structures in it, the waveshape anomaly approaches PKPdf for larger epicentral distances; and this is expected for scatterers on CMB *Cleary and Haddon* [1972]. These synthetics have been compared with those generated by an analytical-numerical interfacing code [*Wen and Helmberger*, 1998b], and found to be satisfactory. As modeled here, we would expect to see considerable complexity of B-diffraction in regions of rapidly varying CMB, which we will address in more detail in a subsequent paper.

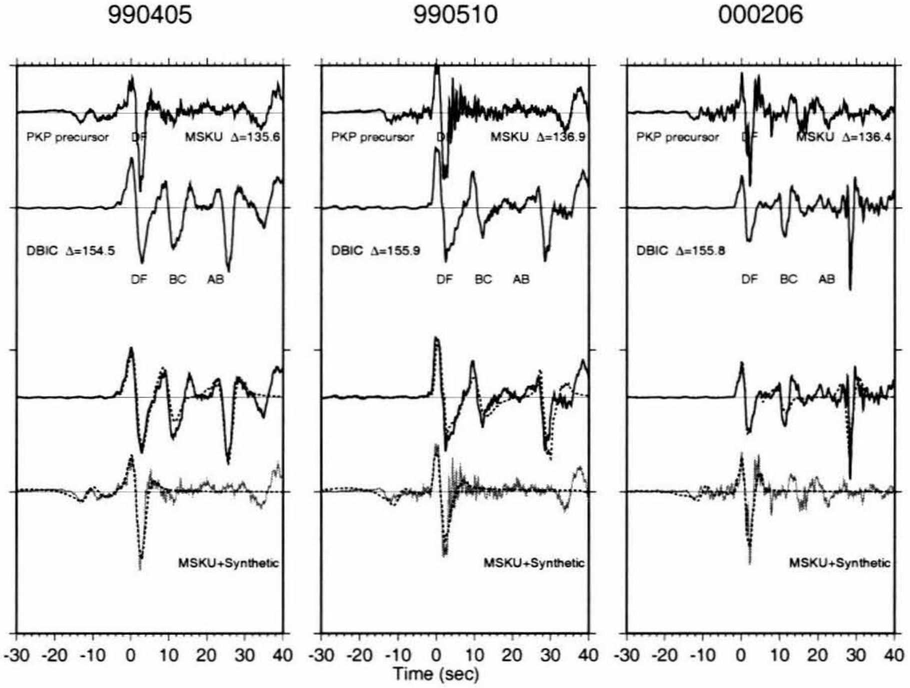

Figure 6.3: PKP observations from three events in the New Britain Region to Africa at stations DBIC and MSKU. The three branches of PKP containing DF (inner-core), BC (lowermost outer-core), and AB (outer-core) are well separated. These waveforms are modeled by PREM-like models as denoted by dotted synthetics displaying simple source characteristics. The 990405 event occurred at a depth of 150 km at Lat. (-5.65) and Long. (149.7°). Its CMT (Harvard's) orientation is strike = 248°, dip = 17°, and slip = 65° with a $M_W = 7.4$. The 990510 event occurred at a depth of 145 km with a similar location. Its CMT orientation is strike = 202°, dip = 47°, and slip = -126 with a $M_W = 7$. The third event is a shallower event occurring at an estimated depth of 33 km. Its CMT is strike = 219°, dip = 29°, and slip = 72° with a $M_W = 6.5$. The observed DF pulses were used for effective duration and normalized amplitudes. Predictions of the PKP phase before the 144° caustic are simple except for the precursors that are not produced by conventional earth models, and require local ULVZ's for their generation. Their separation in time from PKP indicates their approximate position. A shift in the ULVZ position of 50 km produces about a sec change in separation.

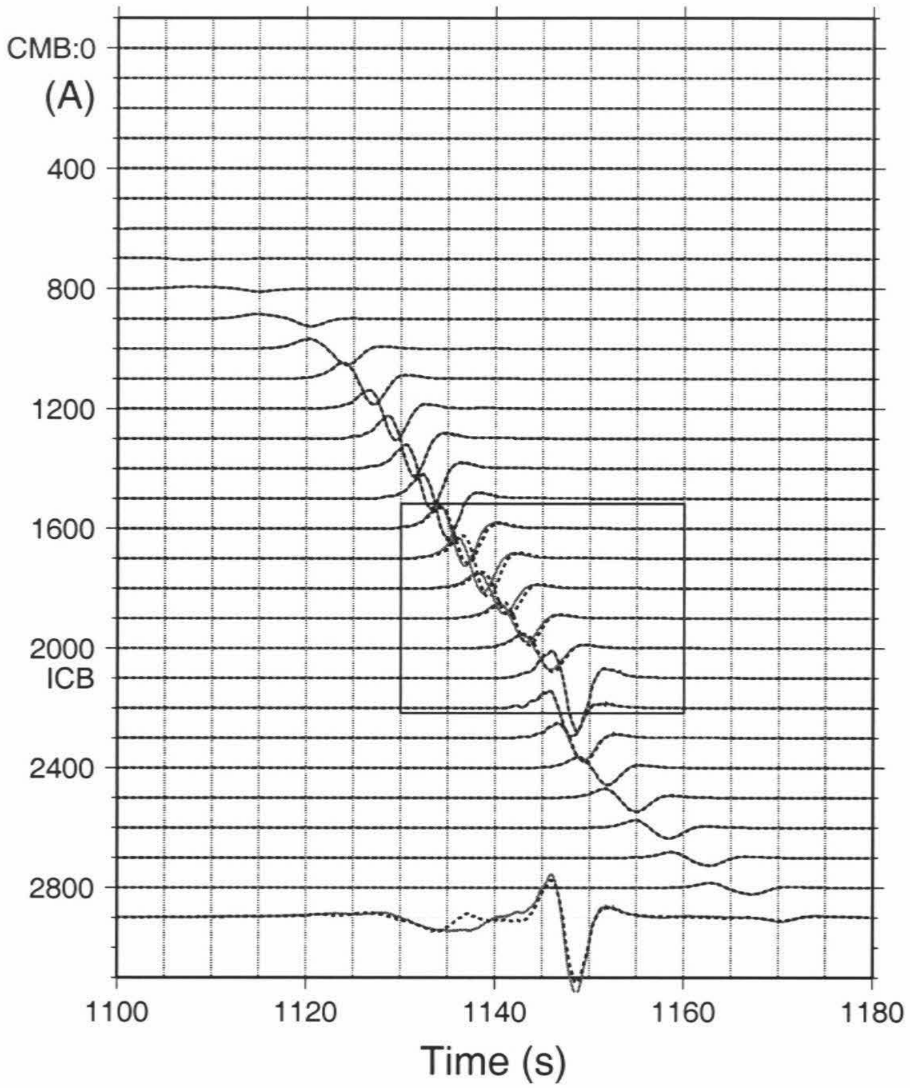

Figure 6.4: Comparison of broadband synthetics (bottom of A) for PREM (solid) with a model containing a dome-shaped low velocity zone (dashed). The geometry is that displayed in figure 6.1 where the dome is 240 km wide, 60 km high, and has a 10% reduction in P-wave velocity. Also included are the various GRT contributions showing the response construction as an interference phenomenon for the two models.

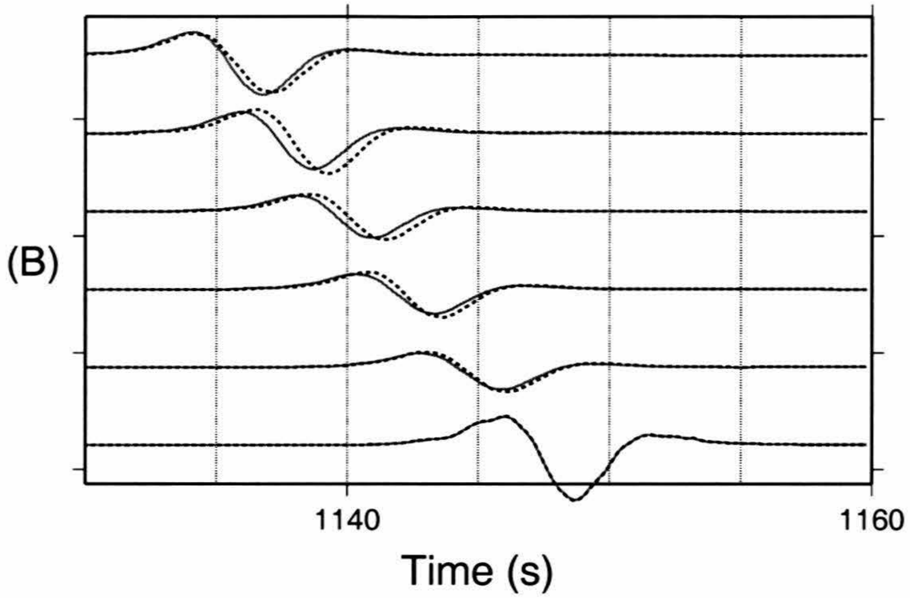

Figure 6.5: A blow-up of the depth zone between 1600 to 2200 km from figure 6.4 is displayed in B showing the shift required to complicate the normally long-period B-čaustic diffraction. The sum of the upper contributions yields the synthetics. The PKIKP (inner-core) and the PKiKP (inner-core boundary reflection) are not separated in this calculation because of coarse-layering; see *Song and Helmberger* [1992] for finer resolution and a comparison of synthetics from other methods (1D).

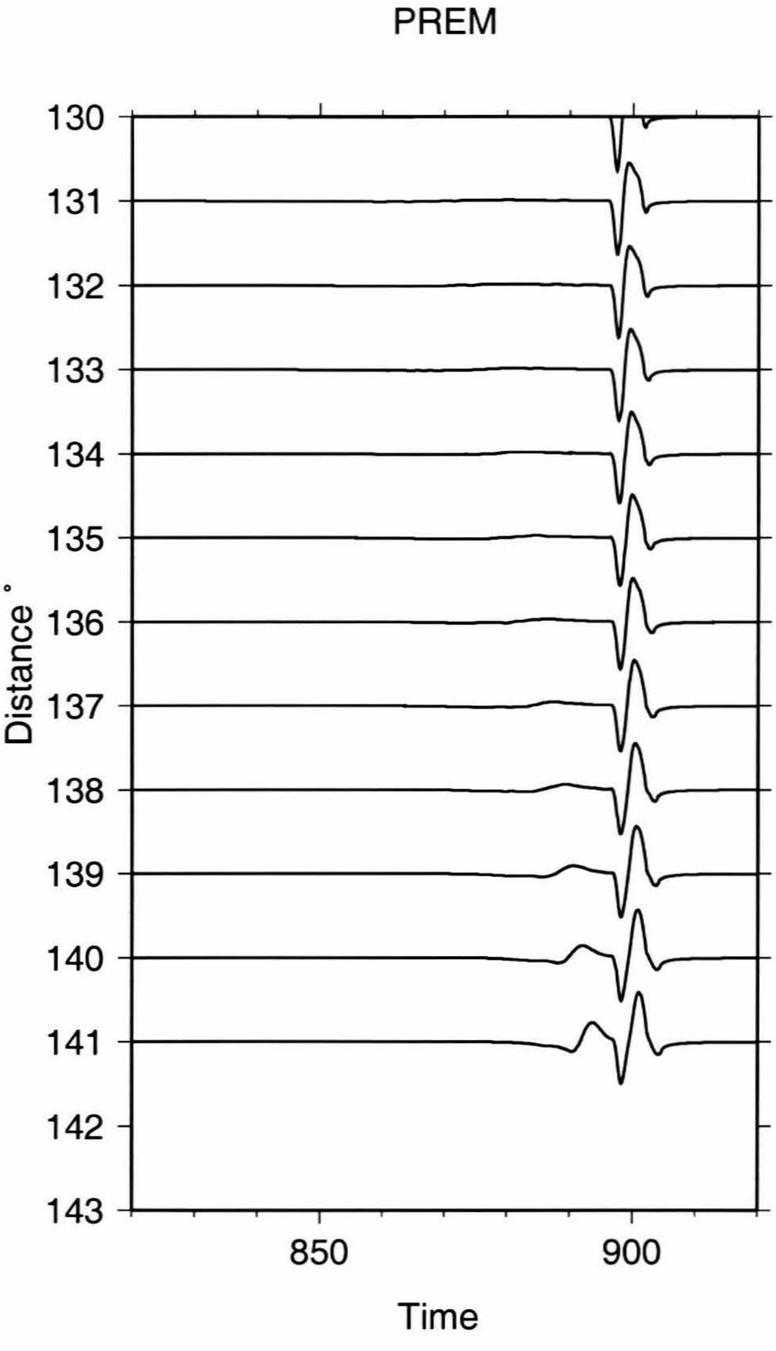

Figure 6.6: 1D GRT synthetic seismograms show smooth PKP precursor. PKP precursor is stronger with increasing distances, and eventually becomes B caustic (around 144 degrees), then triplicates into PKPab, PKPbc.

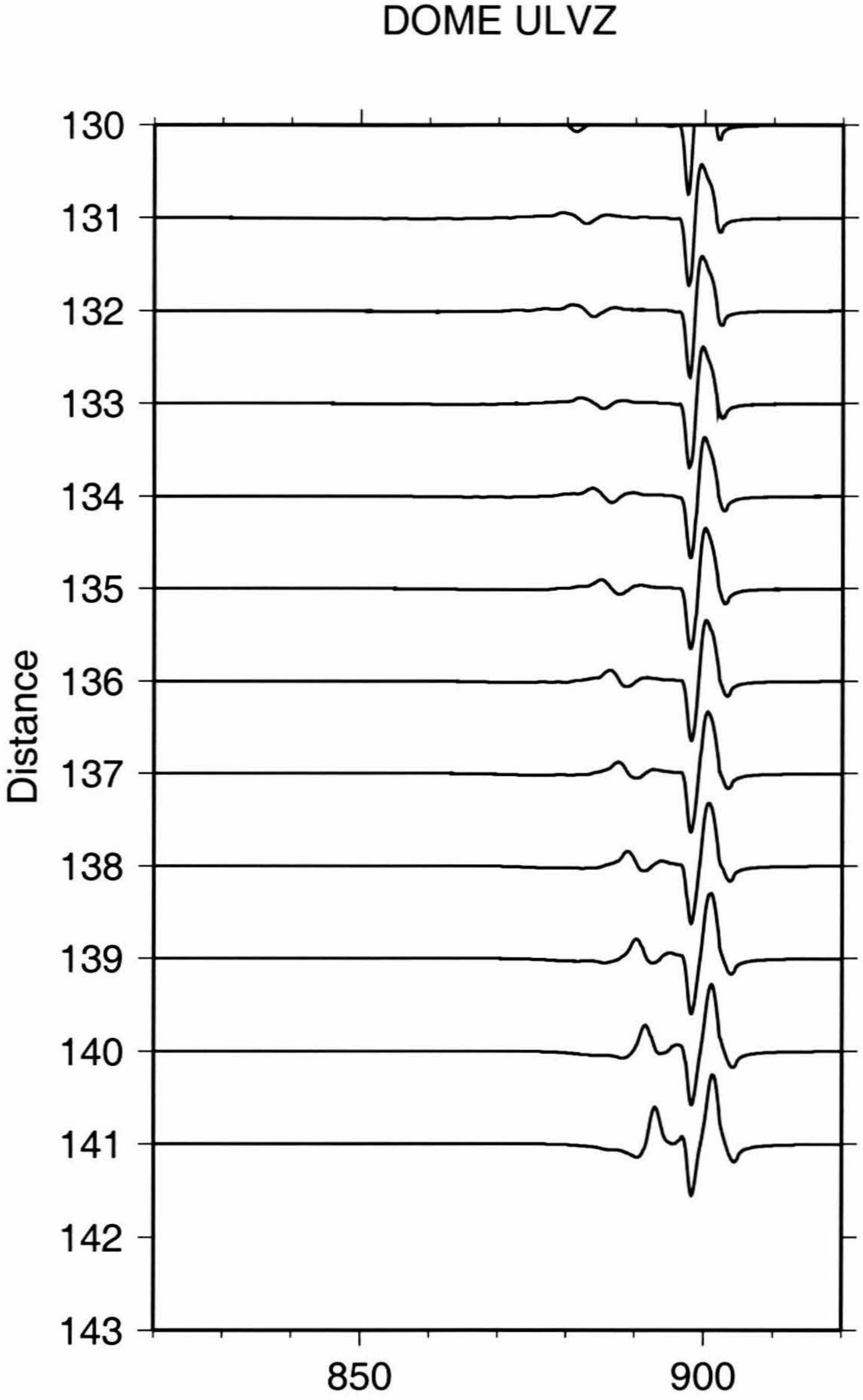

Figure 6.7: 1D GRT synthetic seismograms show anomalous PKP precursor.

6.5 Discussion

A variety of geometric shapes of anomalous structures were considered in *Wen and Helmberger* [1998a], and arguments for their existence at the CMB as opposed to the mantle apply equally here. Essentially, the only portion of the earth where the DF path is separated significantly from scattering paths (figure 6.1) is in the lowermost mantle. The issue of receiver-side versus source-side remains problematic. However, if there were a significant anomaly at the source-side, we would expect to see some distortions in the DBIC observations since the CMB crossings are quite close to those of MSKU. Secondly, moving the source about 100 km does not affect the precursor's position, again supporting the receiver-side interpretation. Moreover, the position of the proposed ULVZ as outlined in figure 6.2d is in agreement with strong short-period scattering as reported recently by *Hedlin and Shearer* [2000]. This relationship between broadband and intense short-period scattering observed here was also observed beneath the mid-Pacific [*Vidale and Hedlin*, 1998]. Thus, it appears that ULVZ's can have a broad range of scale lengths and complexity. This result is in general agreement with local small-scale mantle convection caused by instability of the thermal boundary layer [*Olson et al.*, 1987].

In conclusion, we have delineated a ULVZ extending at least 800 km along the eastern boundary of the Great African upwelling. Its shape is roughly that of a ridge structure with a strong reduction of both S and P velocities of up to 30 and 10%, respectively, as estimated from a combination of SKP_dS and PKP precursors.

Appendix A Seismic Evidence for Ultra Low Velocity Zones Beneath Africa and Eastern Atlantic

A.1 Abstract

. SKS waveforms recorded at distances of about 110° are extremely useful to constrain seismic velocity structure at the base of the mantle. SKS waves near this distance develop a complicated interference pattern with the phases SP$_d$KS and SKP$_d$S. We report anomalous behavior of this interference in a number of recordings of deep earthquakes beneath South America from stations in Europe and Africa. We model these data with two-dimensional dome-like structures at the base of the mantle which extend laterally by a few hundred km and in which the shear velocity is up to 30% lower than in PREM. The spatial extent of these structures, their position with respect to the SKS core exit points, and their seismic characteristics can not be uniquely determined. However, the presence of a dipping or a concaved upper interface is a key attribute of successful models. Models that invoke flat layers are insufficiently complex to explain the most erratic waveform behavior. The most anomalous data correspond to sampling regions at the base of the mantle beneath the East African Rift and beneath the Iceland, where possibly, whole-mantle upwellings form.

A.2 Introduction

The lowermost 300 km of the mantle (termed D" in this paper) is a complex region according to seismological observations and geodynamic models. It contains a thermal boundary layer at its base which transmits about 10 to 15% of the Earth's heat flow

[*Davies*, 1980]; it is highly heterogeneous, and it may well influence convection in the core and mantle [*Lay et al.*, 1998].

Seismic models of D" are derived using a variety of data. Tomographic maps of D" [e.g., *Li and Romanowicz*, 1996; *Masters et al.*, 1996; *Grand et al.*, 1997; *Ritzwoller and Lavely*, 1995] are primarily based on body wave travel times. They show regions with relatively high seismic velocity (compared to PREM [*Dziewonski and Anderson*, 1981]) beneath the circum-Pacific which possibly represent the seismic signatures of downwelling slabs [e.g., *Engebretson et al.,* 1992]. Broad low seismic velocity anomalies, which may represent large-scale upwellings, are present beneath Africa and the central Pacific where subduction has not occurred since the Mesozoic [e.g., *Chase and Shrowl*, 1983]. These low velocity regions contain many of the world's hot spots [*Crough and Jurdy*, 1980], and they correlate with the long-wavelength geoid highs as expected for a convecting mantle [*Hager et al.*, 1985]. Additional seismological constraints on the spatial extent, seismic velocity gradients, and shear velocity anisotropy within these large-scale anomalies have come from the modeling of PcP precursors [*Mori and Helmberger*, 1995; *Revenaugh and Meyer*, 1997], broadband SKS and SP_dKS waveforms [*Garnero and Helmberger*, 1996], differential travel times [*Breger and Romanowicz*, 1998], broadband precursors to PKP [*Wen and Helmberger*, 1998a], and SV-SH polarization [*Lay et al.*, 1998]. Most of these body wave modeling efforts focussed primarily on the Pacific anomaly which is well sampled by seismic waves that propagate from deep earthquakes in the western Pacific to stations in North America.

Recently, high-quality broadband data has been provided by the 1994-1995 PASSCAL experiment in Tanzania [*Nyblade et al.*, 1996; *Ritsema et al.*, 1998a] which enables us to study the deep mantle beneath Africa by waveform modeling. In particular, recordings of earthquakes in the southwestern Atlantic Ocean at the Tanzania array show large shear wave travel time delays that indicate the presence of anomalous structure in the lower mantle beneath Africa (figure A.1).
figure A.1a shows S and ScS travel time delays (with respect to PREM) of an event in the Sandwich Islands while figure A.1b shows S and SKS delays by an event in

the Drake Passage. The S, ScS, and SKS waves propagate through the same mantle corridor between the Drake Passage and central Asia (figure A.2). Note that the delay of S, generated by the Sandwich Island event, increases systematically from about zero at 65° to about 10 s at 75°. ScS phases are delayed by about 12 s over the entire distance range. The Tanzania array was installed on the boundary between the Tanzania Craton and the East African Rift. *Ritsema et al.* [1998b] estimate that about 3-4 s of the S delay is caused by anomalously low seismic velocity structure beneath the rift. The most compelling evidence that the remaining 6-8 s of the delay of S and ScS is caused by low velocity structure in the lower mantle beneath Africa is provided by the SKS data from the Drake Passage event shown in figure A.1b. The trend of SKS delays is opposite from the trend of S and ScS of the Sandwich Island earthquake even though the paths through the upper mantle are virtually identical. These data have been modeled by *Ritsema et al.* [1998b] with a continuous 2D structure that extends 1500 km into the mantle and which contains a uniform 3% drop in shear velocity relative to PREM. The model displayed in figure A.1, however, was obtained by adopting the tomographic model of *Grand* [1994] in which the shear velocity anomalies in the mid-mantle (1500-2600 km depth) have been enhanced [*Ni et al.*, 2000]. This model explains the data of figure A.1 as well as S-SKS differential travel times from South American events recorded in Africa. We introduce this model to define the shear velocity anomaly above the D" region as the African Low Velocity Zone (ALVZ), but we do not imply that the ALVZ is necessarily detached from the D" although it is in Grand's [1994] tomographic results. Dynamic models can reproduce ALVZ-type structures by invoking strong depth-dependent viscosity [*Thompson and Tackley*, 1998; *Zhang and Yuen*, 1997]. However, broad upwellings tend to efficiently remove the CMB thermal boundary layer, leading us to question what this slow D" structure beneath the ALVZ is, whether it contains ULVZ's at its base, and how it relates to whole-mantle upwellings in general.

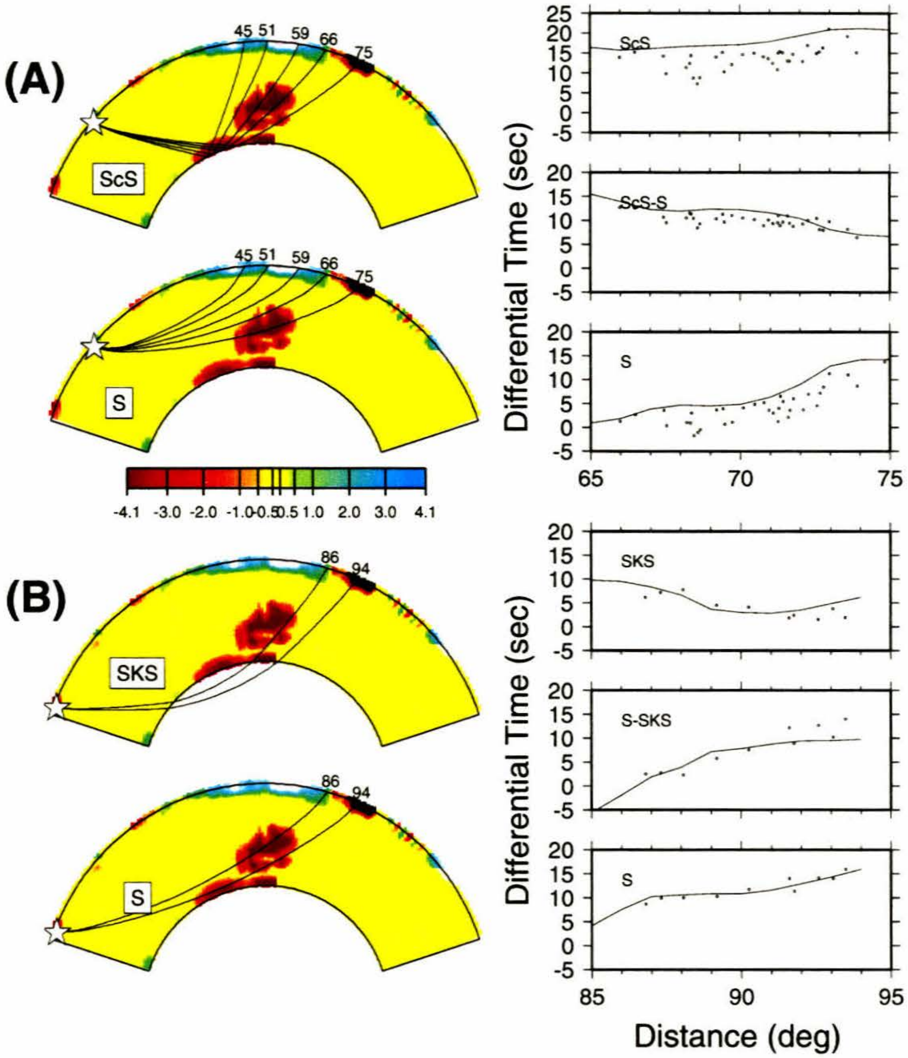

Figure A.1: Cross sections of velocity structure connecting Sandwich Island to the Tanzania array (Grey lines in figure 2) along with raypaths appropriate for S_cS and S in (A) and SKS and S in (B). The corresponding travel times on the right were computed from synthetics generated for these 2D sections (solid lines) along with observed picks from the array as discussed in Ritsema *et al.* (1998b) reduced by PREM. The velocity model was derived from the tomographic images of Grand (1994) by applying an ad hoc enhancement scheme proposed by Ni *et al.* (1999) for other profiles.

A.3 Analysis

The seismic phases SP_dKS and SKP_dS are most clearly observed in radial component seismograms recorded at epicentral distances larger than 105°-110°. These phases arrive just behind the seismic phase SKS and are produced when S impinges upon the CMB at the critical S-to-P conversion angle [*Kind and Müller*, 1975]. The paths of SKS, SP_dKS and SKP_dS are very similar in the core and mantle. However, SP_dKS and SKP_dS also contains short P diffractions along the base of the mantle (figure A.3). By analyzing the interference of SP_dKS and SKP_dS with the SKS, we can constrain the fine-scale seismic velocity and density structure at the base of the mantle with relatively high resolution.

The PREM model predicts that SP_dKS and SKP_dS separate from SKS near 110°. The bifurcation of SKS can be seen in PREM synthetics shown on the right in figure A.4 as SP_dKS and SKP_dS form a single pulse (both phases have identical travel time) that is well separated from SKS beyond about 114°. If the P-velocity at the base of the mantle is lower than in PREM, the bifurcation shifts to shorter distances [*Garnero et al.*, 1993]. Thus, identifying this bifurcation point becomes an excellent tool for constraining the P-velocity structure at localized regions just above the CMB, although still ambiguous with respect to SKS entry and exit points.

A.3.1 a) Anomalous Waveform Data Sampling the Base of the Mantle Beneath Iceland and Africa

The study of SP_dKS and SKP_dS waveforms requires recordings of relatively deep earthquakes in order to avoid interference with the surface reflections of pSKS and sSKS. We selected WWSSN recordings of 16 deep focus earthquakes (Table A.1) beneath South America and Tanzania array recordings for an earthquake beneath Colombia. The Colombia event was at a depth of 70 km and the phase sSKS arrives well after SKS and SKKS (figure A.4). The waveform data shown in figure A.4 are anomalous in several aspects. First, the travel time of SKS is delayed by about 5-10 s. The SKS delay is particularly large at stations AMBA and PUGE, apparently due

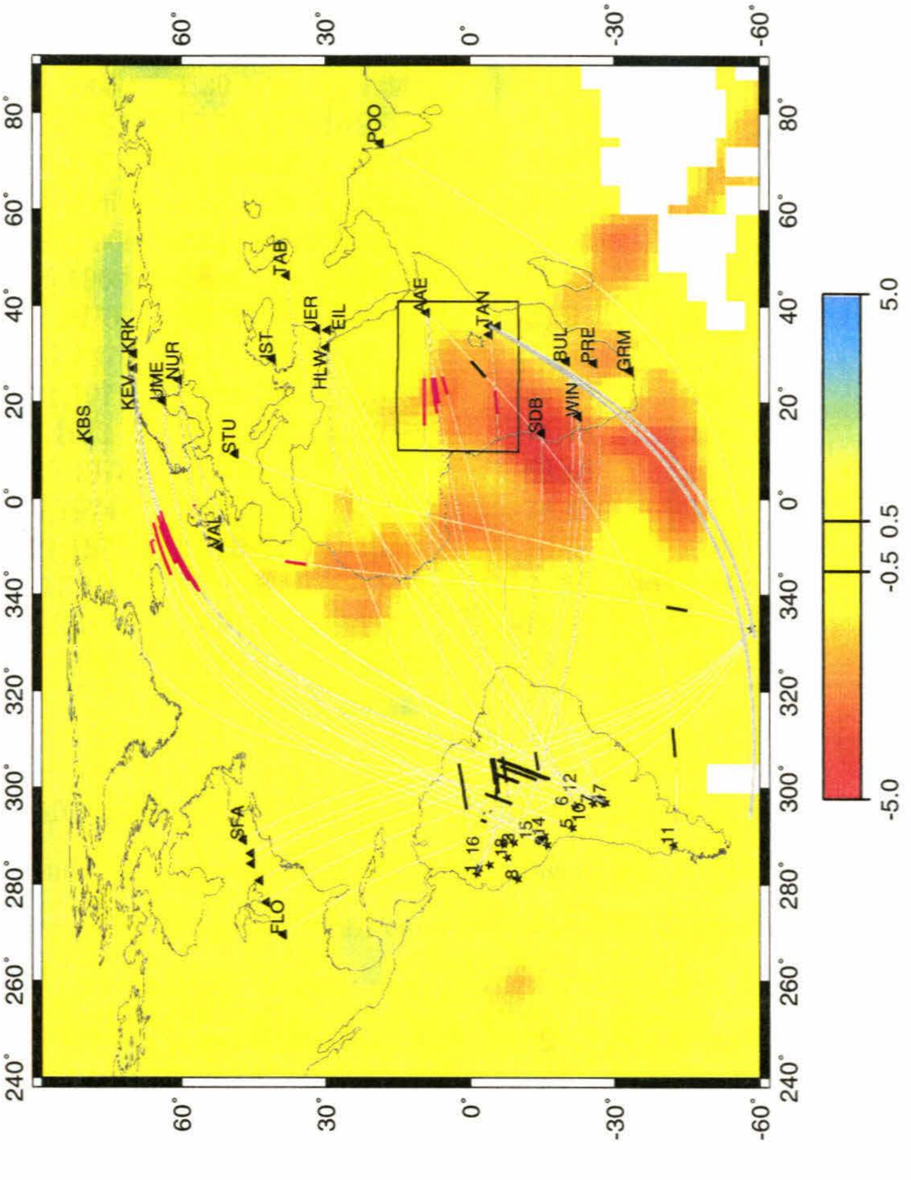

Figure A.2: Tomographic map of the bottom-most mantle velocity (modified from Grand (1994) by Ni *et al.* (1999) along with raypaths indicating sampled structures. Stars denote event locations with triangles indicating WWSSN stations and TAN, the position of the Tanzania array. The heavy line segments indicate the short paths of diffracted P (SP_dKS and SKP_dS) along the CMB. Segments corresponding to anomalous waveforms are rose-colored. The heavy grey lines indicate the position of the 2D cross-sections displayed in figure A.1.

Table A.1: South American events list

No.	Date	Time, UT	Lat (Deg)	Lon (Deg)	Depth (km)
1	Sept. 17,1965	11:13:53.5	-1.4	-77.7	161
2	Nov. 3,1965	1:39:3.20	-9.04	-71.32	587
3	Feb. 15,1967	16:11:11.5	-9.075	-71.38	595
4	Sept. 9,1967	10:6:44.5	-27.62	-63.15	577
5	Dec. 27,1967	8:53:51.4	-21.2	-68.3	135
6	Aug. 23,1968	22:36:49.8	-22	-63.64	513
7	July 25,1969	6:6:42.1	-25.49	-63.21	573
8	June 4,1970	4:9:25	-9.9	-78.9	57
9	June 17,1970	4:44:20.9	-16	-71.88	99
10	Feb. 21,1971	10:35:19.7	-23.8	-67.19	165.6
11	May 8,1971	0:49:45.0	-42.28	-71.78	146.2
12	Oct. 25,1973	14:8:58.5	-21.96	-63.65	517
13	Dec. 5,1974	11:57:31.1	-7.65	-74.45	156
14	May 21,1979	22:22:23.0	-15.44	-70.04	209
15	Sept. 15,1982	20:22:57.8	-14.53	-70.79	153
16	Nov. 18,1982	14:57:51.3	-1.73	-76.72	190
17	Dec. 12,1983	12:21:12:0	-28.13	-63.15	602

to the local rift structure [*Ritsema et al.*, 1998a]. Second, there is an abrupt change in the amplitude ratio of SKKS to SKS beginning at about 110° with a noticeable increase indicative of the interference caused by the SKS bifurcation. Third, several SKS pulses are anomalously broader than predicted by PREM, especially at stations MITU and SING. At larger distances, SKS and SKP_dS are obvious as two distinct pulses in the data. The differential travel time of SKS and SKP_dS is well predicted by PREM synthetics, but the amplitude of SKP_dS is anomalously large.

A sample of radial component WWSSN recordings is given in figure A.5 along with PREM synthetics on the left. These data are divided into three columns. The second column, labeled 'Normal', contains recordings that can, to a large extent, be explained by the PREM model. Recordings for distances smaller than 110° (UME 9 at 104° through UME 7 at 110°) show simple SKS pulses similar to the PREM synthetics. SKS and SKP_dS emerge as separate signals in the record EIL at 9 near 111°, as predicted by PREM. The P diffractions associated with the 'normal' data propagate

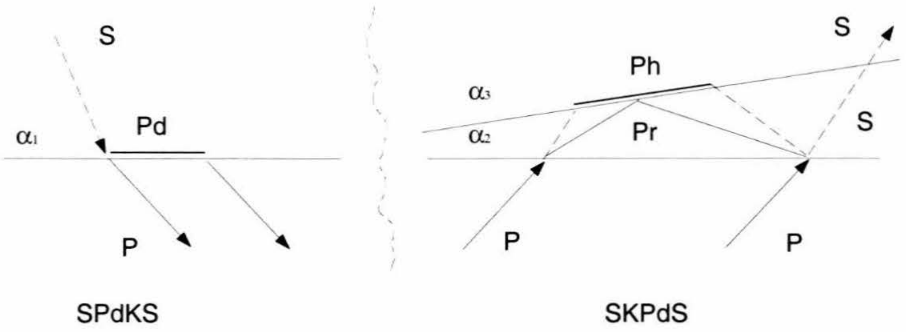

Figure A.3: Schematic ray plots displaying direct S entering the core as P along with a diffracted ray P_d on the left and P exiting the core as S and containing a P multiple in a slow layer on the right. The response can reach critical angle if $\alpha_3 > \alpha_2$ as indicated which can enhance or reduce amplitudes by locally dipping. We will refer to these two packets of rays as SP_dKS (a) and SKP_dS (b).

primarily through regions of D" where the average seismic wave velocity is PREM-like [*Garnero and Helmberger*, 1995; 1998]. The waveforms in the second column, labeled 'Iceland', yield strong secondary arrivals that develop at much shorter distances than in the 'normal' recordings. Compare, for example, the broad signals in recordings KEV 14 with the relatively narrow SKS signals in recordings NUR 14 inserted above it for direct comparison. This same feature occurs in KEV 14 when compared with UME 9. This implies that the path to KEV is anomalous near the CMB, since this broadness does not appear to be a source effect. The fourth column, labeled 'Africa', shows anomalous recordings at station AAE in eastern Africa. We emphasize recordings AAE 2, AAE 3, and AAE 9. The "shoulder" on AAE 14 is similar to that of KBS. Note that these types of features occur in the PREM synthetics and more normal type data at great distances, i.e., EIL 9. However, the recording of event AAE 11 does not show this feature even though it is at the same distance. The path corresponding to AAE 11 is located further to the south compared to the other recordings and could be a manifestation of lateral variation.

The great circle paths corresponding to the data of figure A.5 are shown in figure A.2. Heavy line segments represent the short P-wave diffracted path along the CMB boundary which are colored red if they are associated with anomalous waveform

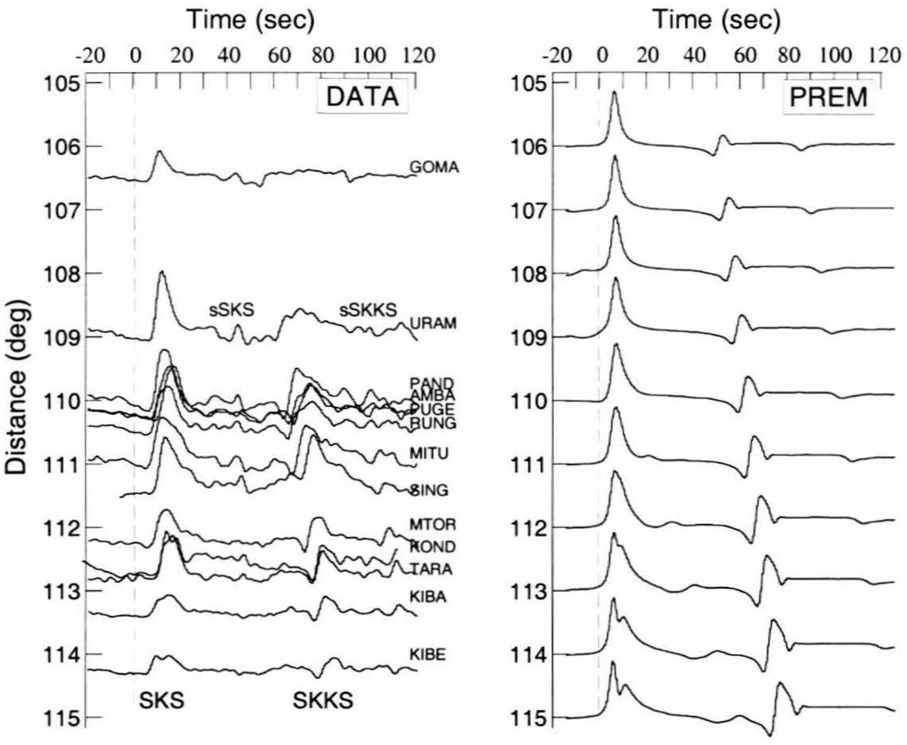

Figure A.4: Display of Tanzania array waveform data (radial displacement) containing SKS interference and corresponding synthetics generated with a reflectivity code. The event and path locations is given in figure A.2.

behavior. Note that the southern path segment associated with AAE 11 is normal (black) whenever AAE 14, AAE 2, 3, 9 are anomalous. Here we assume that D" structures causing the waveform complexity are located at the core-exit locations of SKS within or at the northern edge of the large-scale low shear velocity anomaly beneath Africa.

A.4 b) Modeling the SKS Waveform Bifurcation

To some extent, the waveform complexities seen in figure A.5 can be produced with 1D models which invoke reduced P-velocities at the base of the mantle. Such models are effective in producing the delays of SP_dKS and SKP_dS and enhancing their amplitudes with respect to SKS [*Garnero et al.*, 1993]. Synthetics for basal layers with thickness from 10 to 40 km and with P and S velocity reductions of 5% match the data well.

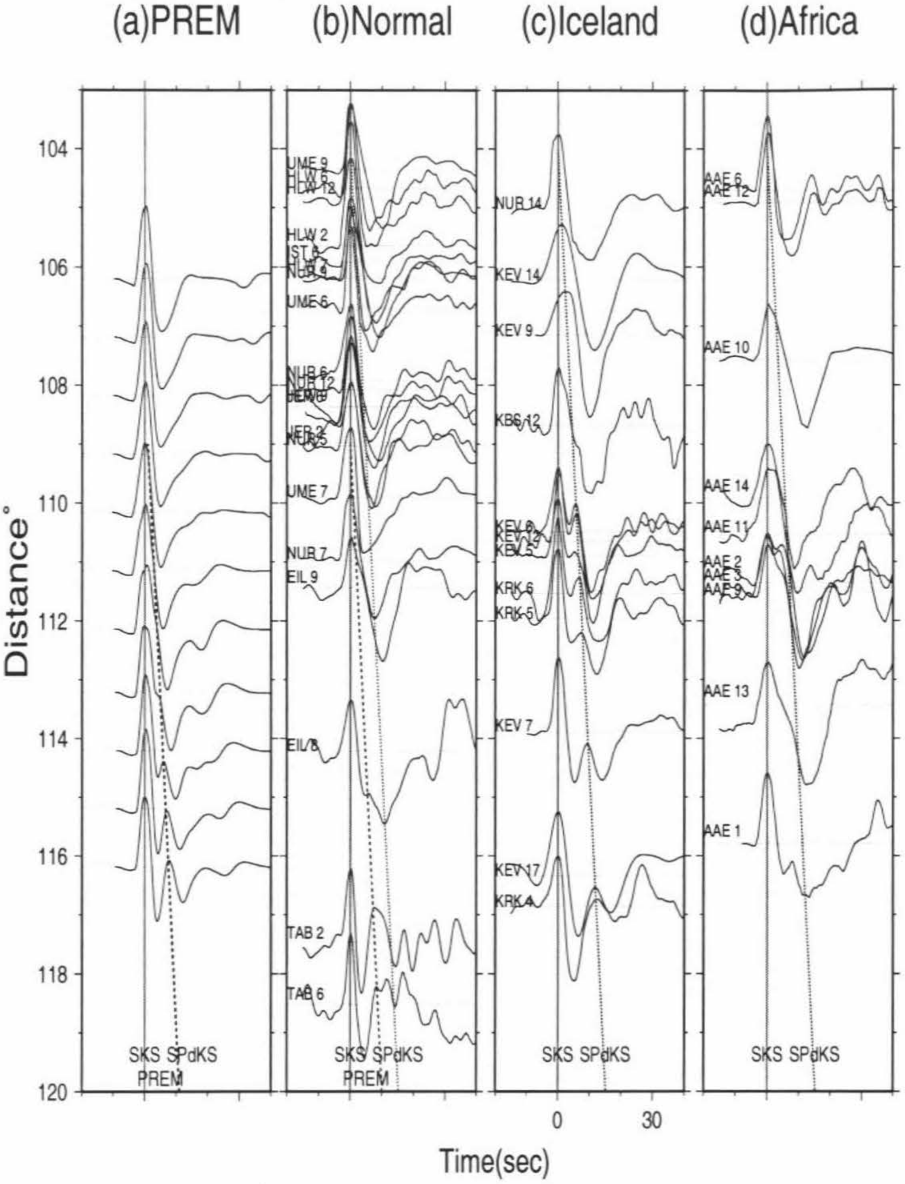

Figure A.5: Display of PREM synthetics on the left accompanied by three columns of analog WWSSN records (radial component) of SKS and diffractions displaying normal and anomalous waveforms (beneath Iceland and Africa). The numbers indicate events as identified in Table A.1. The stations are identified by their three latter codes with corresponding locations given in figure A.2. Timing lines appropriate for SKS, SP_dKS (PREM) and SKP_dS (anomalous with respect to Iceland data) are included. Note that events 5, 6, and 12 appear relatively simple at stations on the left while the recordings of these events at KEV and KRK are complex. The same feature occurs at AAE for events 2 and 9. Note also that the two traces of AAE that are not very anomalous, AAE11 and AAE1, correspond to the southern and northernmost paths.

If the anomaly is confined to either the core entry or core exit point of SKS, we need to increase the velocity anomalies to 10% [*Helmberger et al.*, 1996a]. Such one-sided structures with thickness variations ranging from 5-40 km fit are particularly useful to explain many anomalous mid-Pacific data [*Garnero and Helmberger*, 1995]. A sample of these observations is displayed in figure A.6a. Note that a secondary phase (SP$_d$KS) emerges at epicentral distances smaller than 110°, and several recordings yield high amplitude secondary pulses (denoted by the solid dots) that can not easily be explained with models that employ flat basal layers. Enhanced SP$_d$KS and SKP$_d$S amplitudes can be obtained when the shear velocity in basal layers is significantly reduced (figure A.7); however, an oscillatory wavetrain that follows SKS throughout the 110°-110° distance range has not been observed in the SKS coda. By reducing the thickness of the basal layer, the oscillatory wavetrain is suppressed [*Garnero and Helmberger*, 1998]. Nonetheless, strong SKS waveform distortions such as those shown in figure A.6 (dots) can not be modeled with a simple flat-layered model since the observed second arrival is anomalously strong and develops early relative to PREM.

High amplitude reflections are often recorded by stations located in sedimentary basins. These signals have been successfully modeled using dipping interfaces [*Helmberger et al.*, 1983]. Models with dipping interfaces lend themselves also to the study of teleseismic SKS waveform data. As illustrated in figure A.3, a structure dipping upward allows for the development of high amplitude SKP$_d$S signals at relatively short epicentral distances without introducing complex SKS coda. Synthetics for models with dipping interfaces can be computed using 1-D model by simply increasing the velocity contrast locally, where α_3 becomes the apparent velocity referred to as the 'local stretching approximation' in *Helmberger et al.* [1996b]. Another new method to compute more accurate synthetics for such extreme models was introduced by *Wen and Helmberger* [1998b]. In this approach, the interaction of SKS and SKP$_d$S with fine-scale CMB structure near the SKS core exit point is estimated using a finite-difference technique while the propagation of SKS and SP$_d$KS through the core and mantle is treated analytically. A comparison of the 'local dipping approximation' against the more exact solution is also made in figure A.8. The synthetics in the

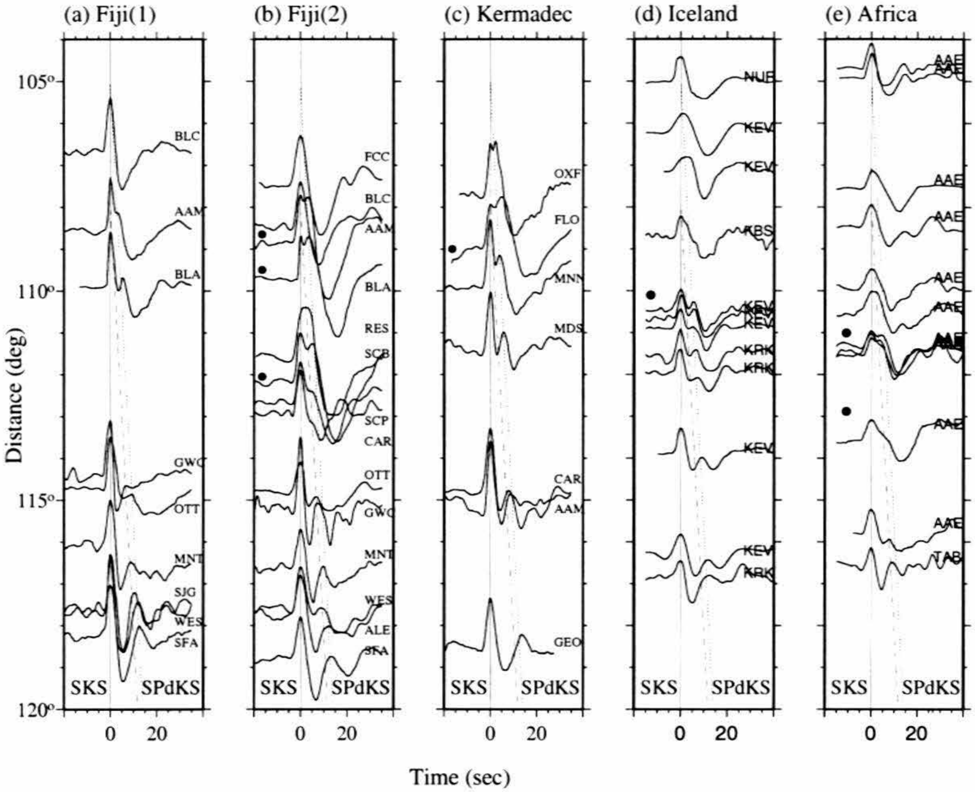

Figure A.6: Comparison of waveform observations from various anomalous regions; see Garnero and Helmberger (1998) for details about the Fiji and Kermadec events recorded in North America. The timing lines are the same in all columns indicating the SKS arrival relative to observed diffracted P (dotted) and theoretical PREM (dashed).

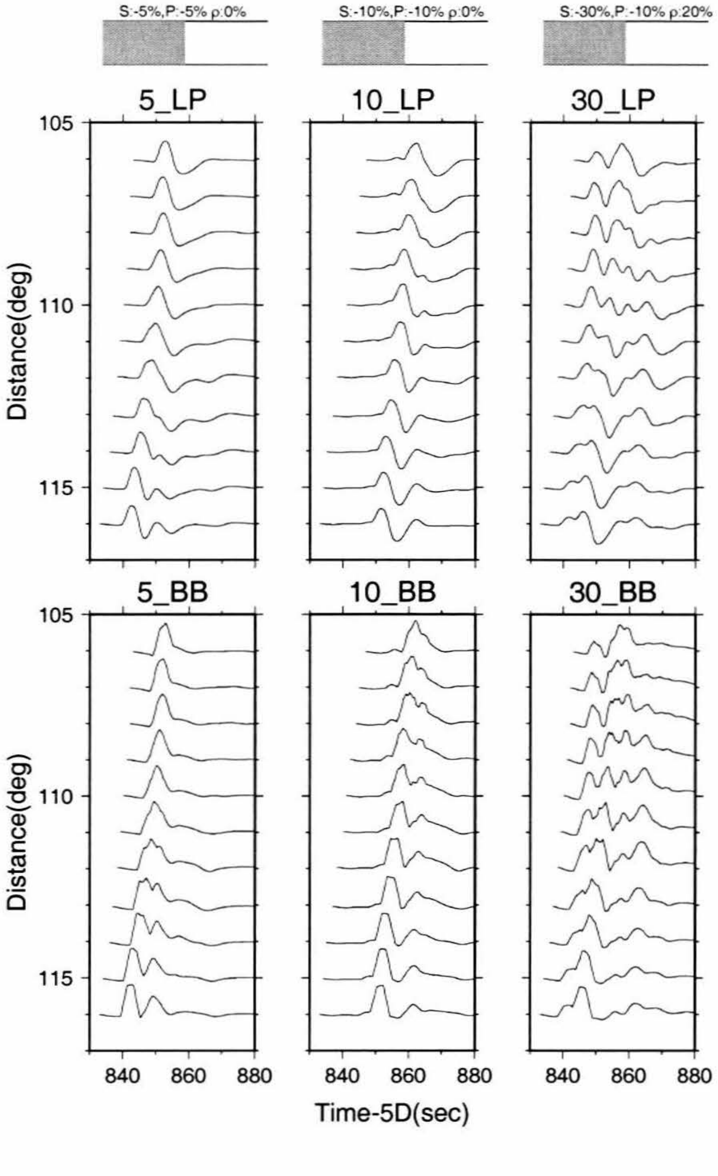

Figure A.7: The three columns of synthetics are appropriate for three models assuming various degrees of drops in P and S velocity indicated at the top. The layer thickness is 30 km. Mixed paths with a low velocity layer for SP_dKS and PREM for SKP_dS. Upper panel displays WWSSN (LP) simulation with broadband (BB) below assuming a (2, 2, 2); see trapezoidal time history. These synthetics are plotted as a record section with a reducing velocity. Note the complexity as the shear velocity drops and shift of the interference to shorter distances.

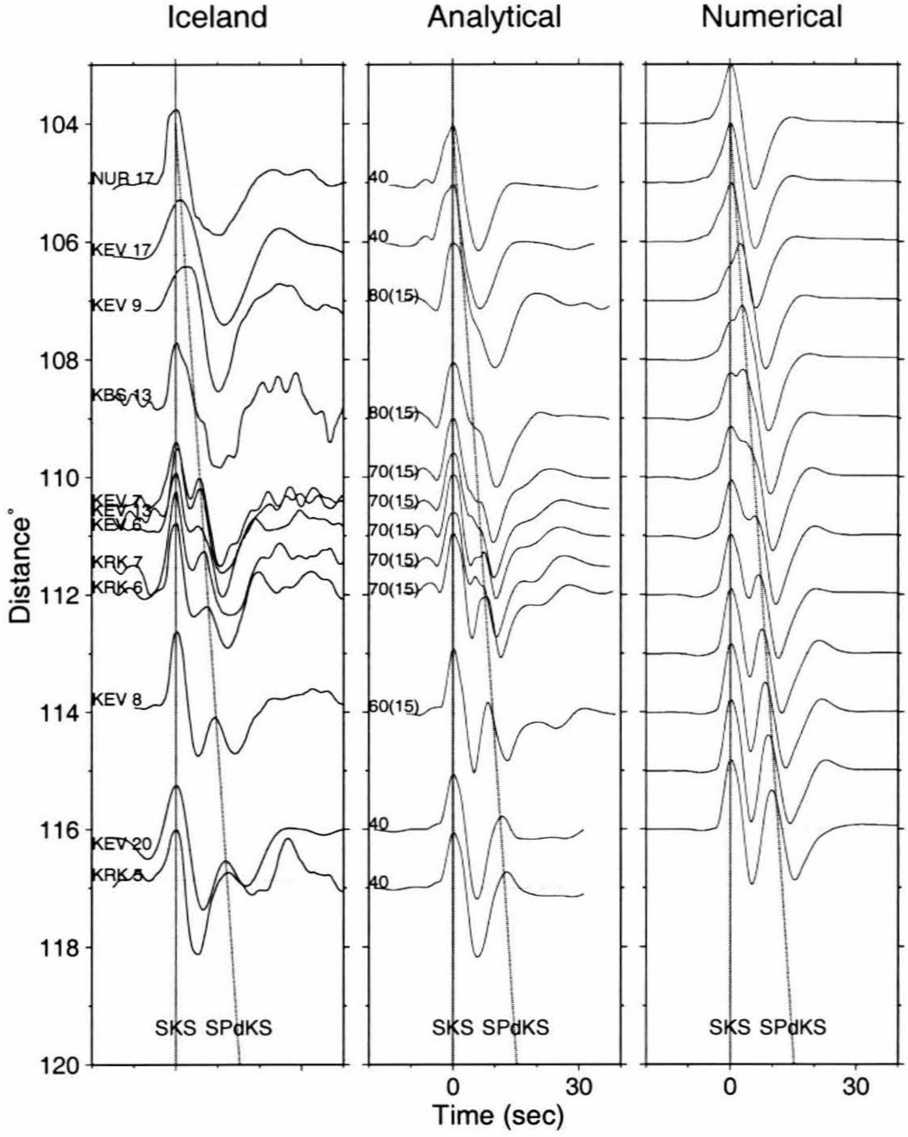

Figure A.8: Comparison of the Iceland observations against synthetics produced by an analytical approach (middle) and those generated by the hybrid method (Dome) on the right. The numbers above the synthetics indicates the ULVZ layer thickness relative to the SKS path with the numbers in parentheses indicating the percentage jump in α_3. The layer velocities and Dome velocities are 10% lower than PREM both in P and S with the same density. The dome height is 80 km and is situated relative to SKS to maximize the diffraction amplitude.

third column are computed for a dome that is 80 km high, 200 km wide, in which the P and S velocity is reduced by 10%. The dome is positioned with respect to the SKS core exit point to maximize the amplitude of the reflection from the upper boundary of the dome. Internal multiples within the dome while notable are not strong if the S velocity reduction is less than 10%, or if the height of the dome is less than 20 km (figure A.9). Synthetics for domes with a height of 40 km and with P and S velocity reductions of 10% and 30%, respectively, provide a good match to the 'Iceland' profile, capturing most of the strong interference near 111°. Only the average structure is sufficient for modeling these waveforms. The shape of the dome and the velocity gradient at its top affect the waveforms only marginally [*Wen and Helmberger*, 1998b].

The models are not only non-unique in terms of trade-off between structural shape and seismic parameters but also in terms of the position of the ULVZ dome with respect to SKS core exit points (figure A.10). If we place the dome such that the P-wave traveling upward within the dome is reflected back downward at the upper boundary of the dome and reflected back up at the core near critical angle S, we can generate a strong and delayed SKP_dS as displayed on the right. The amplitude of this converted P to S phase is large only over a few degrees as discussed in [*Helmberger et al.*, 1996a]. Thus, the geometry becomes extremely important. Small lateral shifts of the dome alter the amplitude of this phase and produce rapid changes in the SKS-SKP_dS interference pattern. For example, the recording at KBS near 109° in figure A.9 is obtained from a distinctly different path than those traveling to KEV and KRK (shown in figure A.11) and can be fit by synthetics for the 20D model and by synthetics for the 40D model which invokes a dome that is shifted slightly to the left (figure A.10c). Obviously, without a dense epicentral distance sampling of the SKS-SKP_dS, we can not constrain the shape and position of ULVZ domes completely, nor do present-day tomographic models help us to discriminate between viable models at this small scale.

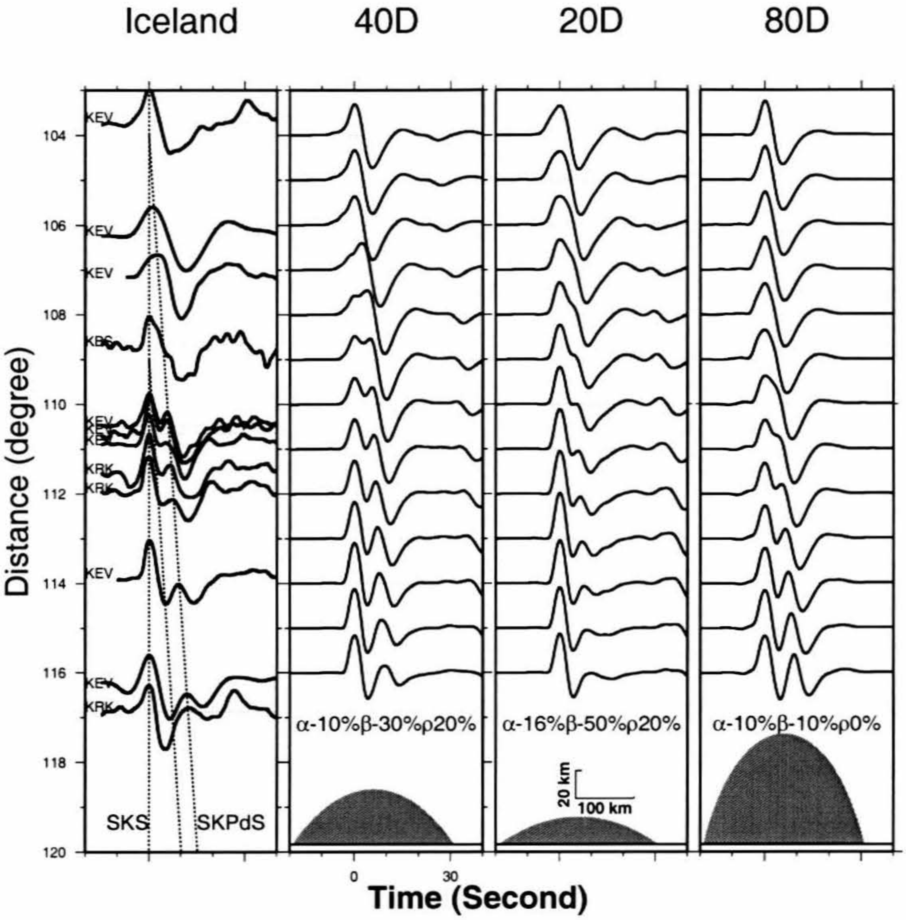

Figure A.9: Anomalous observations of South American events recorded at KEV and KRK along with three columns of synthetics. The observations are aligned on SKS with a line indicating the diffraction SKP$_d$S. The dome heights are 80, 40 and 20 km with reductions in velocity as indicated.

A.4.1 c) Modeling the African Waveform Data

A broad low shear velocity anomaly is located in D" beneath the eastern Atlantic and Africa (figure A.12, upper panel) which is far more anomalous than the shear velocity structure beneath Iceland. However, station AAE appears to be near the northern edge. *We would expect an Iceland-type geometry with the SKS points situated on the limb of the structure and SKS-bifurcation waveforms to sample more of the slow velocity.* In fact, most AAE waveforms can be modeled with synthetics taken from the middle columns of figure A.10. For these events, SKS emerges to the right of the structure. A comparison of the AAE observations against these synthetics (figure A.10c) is displayed in figure A.13, except for the two records denoted by stars, selected from slightly different geometries indicated in figure A.10. Waveform complexities such as a small shoulder in AAE 14 and perhaps the high amplitude SKP_dS pulse in AAE 9 are likely due to 3-D structure. Although the comparison between data and synthetics is not perfect, the 2-D synthetics do explain the very strong secondary arrival near 111° much better than synthetics computed for models with flat-layered structures.

The waveform corresponding to the southernmost path to AAE, denoted by the black segment in figure A.10, is not as anomalous, and neither are many of the Tanzania Array waveforms. This could mean that the ULVZ has pinched out or the geometry here is less favorable to SKP_dS. It would appear that the SKS exit points are near the maximum slowness, a situation not unlike that producing column (a) in figure A.10. For comparison, we added a column on the right containing our best fitting mixed 1D layered model. The path geometry appears to be in agreement with most of the observations (figure A.14) where the SKP_dS interference occurs at relatively larger distance than at AAE. These 2D synthetics were generated from column (a) and (d), with a time history adjusted to roughly match the GOMA observation assumed to be (SKS – SKP_dS) free of interference. This is relatively simple in the Mix 1D model since the synthetics reduce essentially to a delta function for distances less than 107°. The 2D structures with large seismic parameter drops remain somewhat complex at all

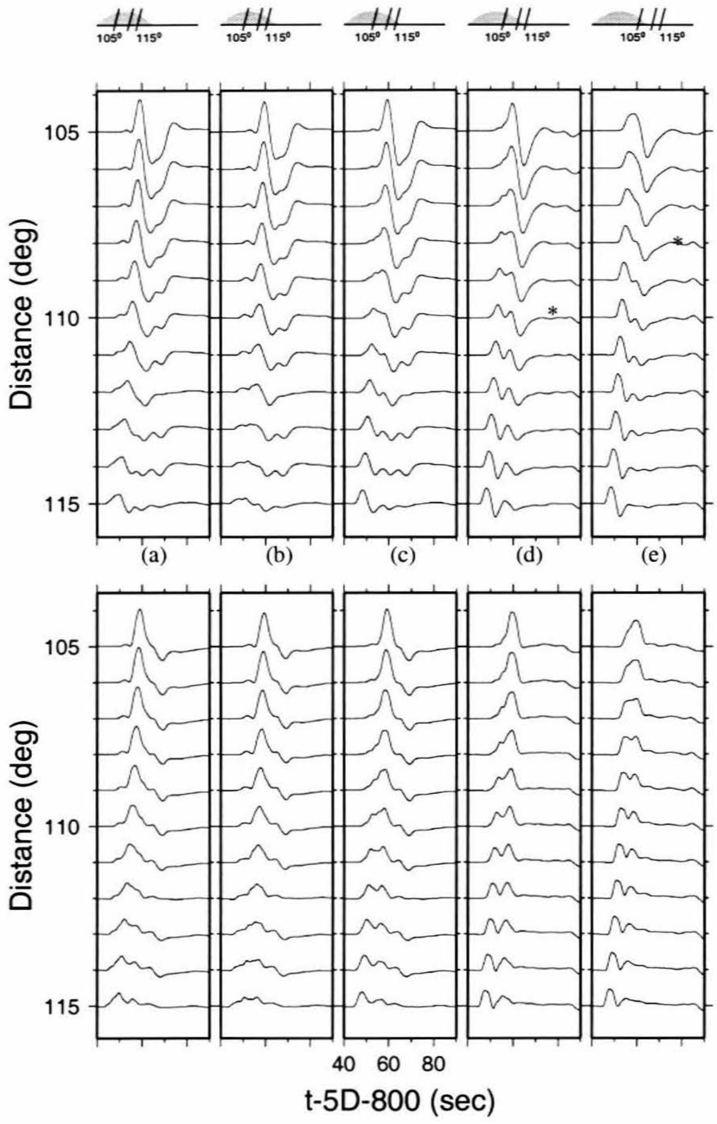

Figure A.10: Sensitivity tests showing the effect on dome position with respect to SKS, with lines indicating the range of CMB crossings. Thus, the dome is directly centered on the SKS paths on the left and shifting off the dome to the right where the diffracted effects are enhanced in the 108° to 112° window. The upper panel contains a WWSSN response while the lower panel displays displacement. The amplitudes are plotted relative to the top trace (105°). Note the small amplitudes in the second column at the larger ranges where SKS is being defocused by the strong curvature. These waveshapes will be used to model the African data.

ranges because of internal multiples, especially in SYN2D2. This column was included to show the expected behavior for the same dome positions used in modeling the AAE data set but without the long-period WWSSN filter. These waveforms (SYN2D2) do not fit the observations very well, especially at the shorter distances. The SYN2D1 synthetics fit the data quite well except at a few stations (SING and PUGE) which prefer a weak SKP$_d$S such as displayed in column Mix1D. The broadness of some of the southernmost paths, such as to RUNG and MITU, is quite pronounced in agreement with SYN2D1 synthetics. Allowing the geometry to vary slightly would obviously aid in the modeling process, i.e., the observations at KIBE looks like the average of SYN2D1 and SYN2D2. In short, it appears that the array data is sampling some complex structure on the northern edge of a strong anomaly, which is delaying the development of SKP$_d$S. Another possibility is that the ULVZ is pinching out into a LVZ such as modeled on the right. Either interpretation yields a picture with rapidly varying CMB structure beneath the northern edge of Grand's anomalous D" structure. Thus, it appears that the African structure is not unlike that occurring beneath the mid-Pacific: essentially a widespread low velocity zone with pockets of ULVZ's beneath some regions.

A.5 Discussion

It appears that an ULVZ exists under a portion of the ALVZ and may be associated with the upwelling process. The ALVZ can be seen in the upper panel of figure A.12 as a low shear velocity structure that extends from the CMB into the upper mantle, bracketed by SKS and SKKS. A much clearer expression of the ALVZ extending into the upper mantle is shown by *Ritsema et al.* [1999]. However, there appears to be some horizontal offsets along this path. This may indicate a change in the style of convection caused by chemistry [*Kellogg et al.* 1999] or the expected increase in viscosity at these depths. At shallower depths, receiver function analysis at the Tanzania array also suggest that shear velocities in the transition zone, the structure between the 410 and 660 km boundaries, are anomalously low [*Gurrola et al.*, 1999].

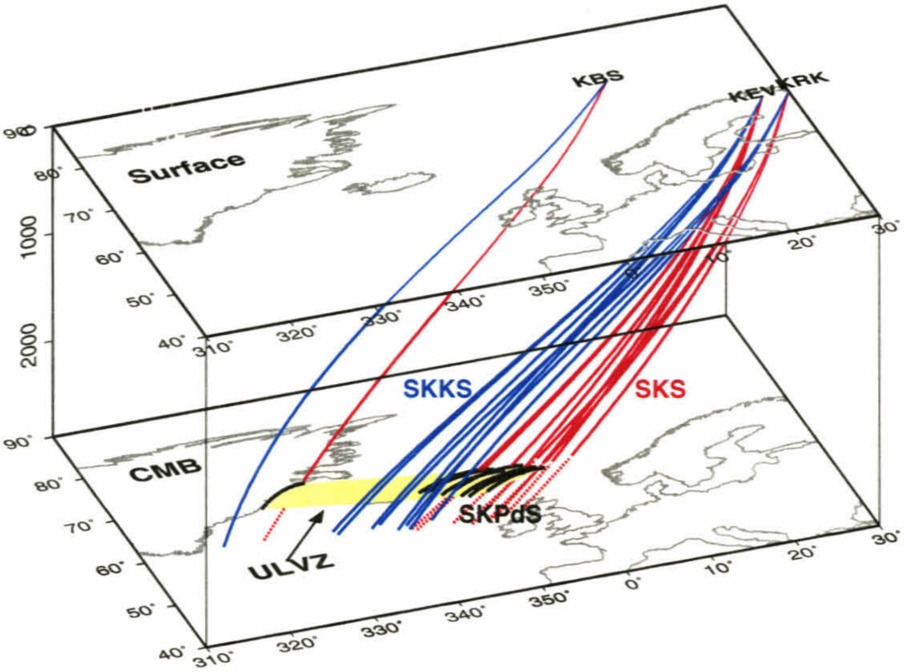

Figure A.11: Diagram of path geometry relative to anomalous structure. The surface panel contains a map with Iceland situated above a 2D-shaped dome in yellow. Mantle paths of SKKS (blue) and SKS (red) are indicated in solid with core paths (dotted).

They suggest lateral changes in the depths to these boundaries and conclude that the transition zone is about 25 km thinner than the global average of 250 km. A similar result has been reported earlier for the transition zone beneath Iceland [*Shen et al.*, 1996]. The P wave tomographic model by *Bijwaard et al.* [1998] also suggests that a continuous low velocity anomaly extend from the upper mantle beneath Iceland to the CMB. Africa and Iceland have both been classified as regions where volcanism may be related to mantle plumes [e.g., *Sleep*, 1990]. Thus, perhaps the correlation of mantle plumes with anomalous low velocity regions at the CMB, as proposed by *Williams et al.* [1998], has merit. Although the evidence is weaker than below Africa, there seems to be a vertical structure beneath the southern mid-Atlantic ridge, i.e., near 55° in the top panel of figure A.12.

There is direct evidence for an LVZ or perhaps an ULVZ beneath the north mid-Atlantic as discussed earlier, i.e., path from Sandwich Island to VAL in figure A.2. Thus, there appears to be some relationship between the downwelling beneath the Americas and the upwelling to the east. If the fast velocities is indicative of heavy material (cold), as suggested by Sidorin et al. (1999), it may push the thermal boundary layer away from the Americas towards Africa causing it to thicken, which could be the anomalous layer (D″) near the CMB beneath the ALVZ in figure A.1.

Another explanation is that the D″ structure beneath ALVZ is simply a manifestation of a small amount of melt. As suggested by *Knittle* [1998], we might expect some chemical differentiation assuming a hot lower-mantle *Holland and Ahrens* [1997]. Some melt would move upward fueling the upwelling directly and some would move downward forming a heavy slow D″, providing the CMB density anomaly proposed by *Ishii and Tromp* [1999]. In this context, the ULVZ's would just be a local concentration of particularly strong melt below a major upwelling.

In conclusion, we have reviewed existing SKS-bifurcation waveform data in comparison with observations sampling beneath Iceland and Pacific with new data from Africa. To model the extreme delays and strengths of $\mathrm{SKP_dS}$ relative to SKS in some observations requires ULVZ's containing short-wavelength structures on the CMB. Thus, we have examined the raypaths through Grand's tomography model for the

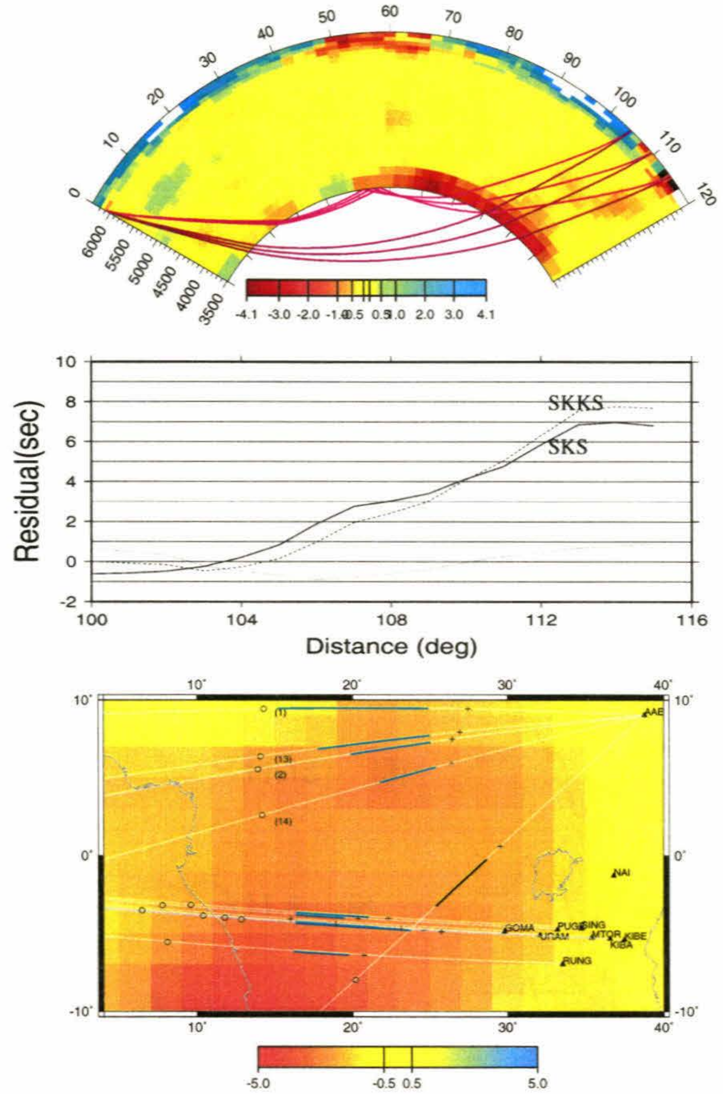

Figure A.12: Upper panel contains a 2D section of Grand's tomography model with SKKS (red) and SKS (brown) geometrical paths connecting the South American event to TAN. Middle panel contains predicted times relative to PREM, SKS (solid) with SKKS (dashed). Note that the differential times (dotted) are nearly zero as observed. Lower panel displays a detailed map of the CMB showing the piercing points, SKS (crosses) and SKKS (circles) along with P-diffraction segments. Also note that the TAN samples of SKS are already well into the slow structure relative to the geometry for AAE.

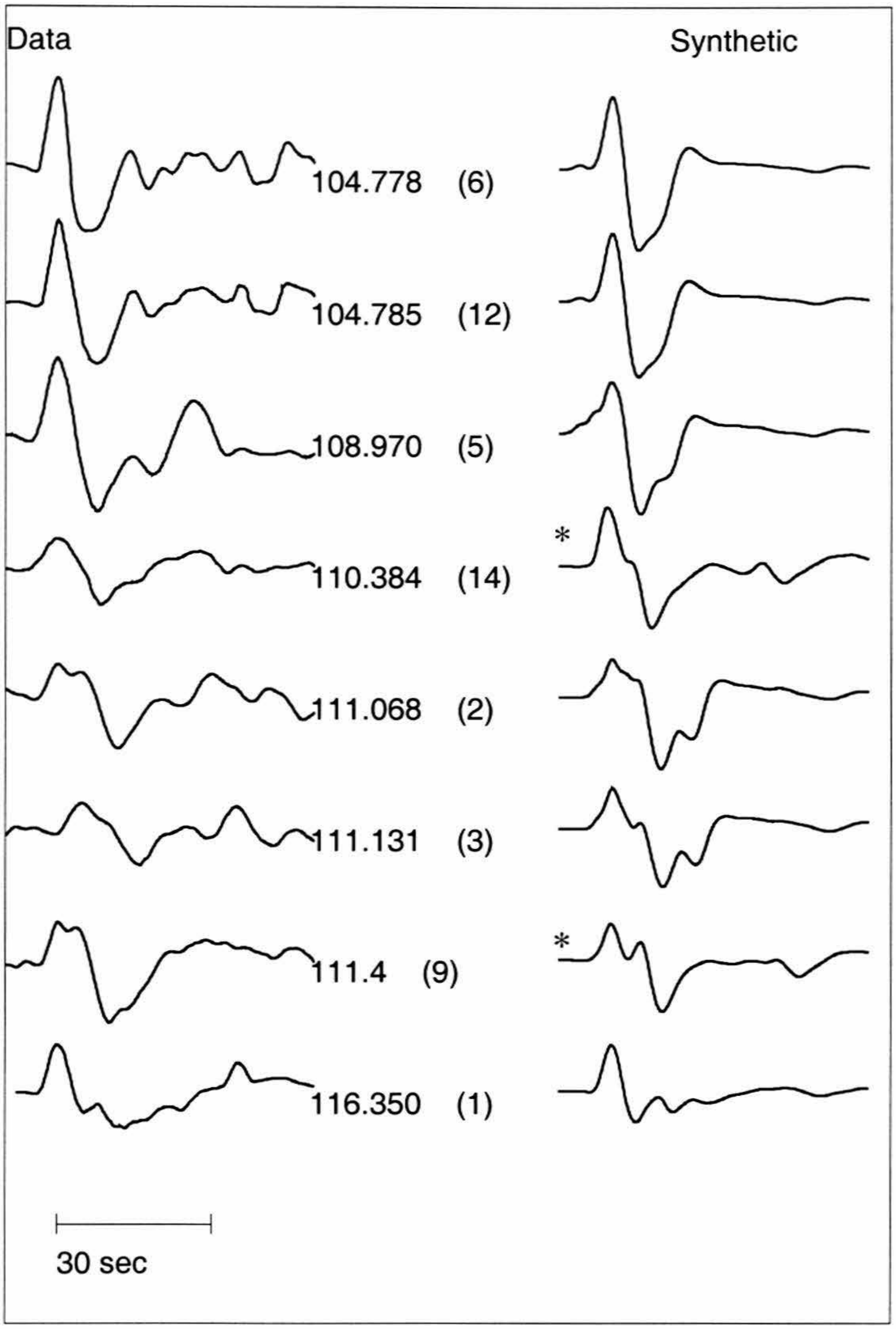

Figure A.13: Comparison of the AAE waveform observations with synthetics selected from figure A.11 (middle column), except for the two observations labeled (∗). Some of these synthetics have been shifted slightly in distance to correct for small changes in source depth, as in Garnero and Helmberger (1998). Note the strong interference observed for events (2), (3), and (9), which are well-modeled by this 2D structure.

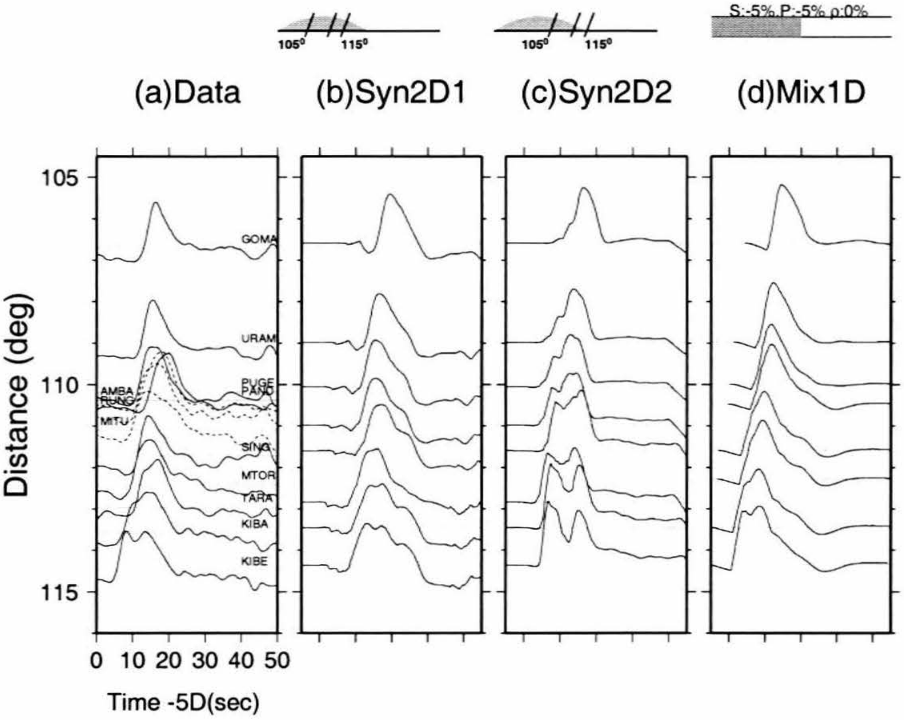

Figure A.14: assuming a Dome structure and a mixed path. The first two columns, Syn2D1 and Syn2D2, contain the Green's functions given in figure A.10 (a) and (d). The synthetic Mix 1D contains the layered approximation with PREM on the source-end, and a 5% drop in a layer 30 km thick beneath the array (see figure A.1c). The dotted traces correspond to the southernmost paths as displayed in figure A.12.

simplest situation (Iceland) and the most complex (Africa). Velocity drops in S of up to 30% and curvature of interfaces of 40 km over 300 km laterally proved effective in modeling efforts in both situations. However, these synthetics are 2D and the structure is obviously 3D. Thus, to resolve these detailed features of ULVZ's in relationship to surrounding structure will require very dense station coverage of the type proposed in the U. S. Array experiment along with 3D synthetics.

Bibliography

Bergeron, S., Y. D.A., and V. A.P., Capabilities of 3-d wavelet transforms to detect plume-like structures from seismic tomography, *Geoph. Res. Lett.*, *27*, 3433–3436, 2000.

Berryman, D., Ration of P and S velocity perturbation, *Geoph. Res. Lett.*, *27*, 421–424, 2000.

Breger, L., and B. Romanowicz, Three-dimensional structure at the base of the mantle beneath the central Pacific, *Science*, *282(5398)*, 718–720, 1998.

Burke, K., The African plate, *S. Afr. J. Geol*, *99*, 341–409, 1996.

Chapman, C., Exact and approximate ray theory in vertically inhomogeneous media, *Geophy. Journ. Roy. Aus. Soc.*, *46*, 201–233, 1976.

Cleary, J., and R. Haddon, Seismic wave scattering near the core mantle boundary: a new interpretation of precursors to PKP, *Nature*, *240*, 549–551, 1972.

Cormier, V. F., Anisotropy of heterogeneity scale lengths in the lower mantle from PKIKP precursors, *Geophys. J. Int.*, *136*, 373–384, 1999.

Cormier, V. F., D" as a transition in the heterogeneity spectrum of the lowermost mantle, *J. Geophys. Res.*, *105 No. B7*, 16,193–16,205, 2000.

Cormier, V. F., and P. G. Richards, Full wave theory applied to a discontinuous velocity increase: the inner core boundary, *J. Geophys. Res.*, *43*, 3–31, 1977.

Cormier, V. F., D. Helmberger, and S. Ni, Sharp lateral transitions in D" structure marked by ScS Waves: Effects of edges of remnant slabs, *AGU FALL MEETING Proceedings*, p. F902, 2000.

Ding, X., High resolution studies of deep earth structure, *Caltech Thesis*, 1997.

Dziewonski, A. M., and D. L. Anderson, Preliminary reference earth model (prem), *Phys. Earth Planet. Inter*, *25*, 297–356, 1981.

Frazer, L., and R. A. Phinney, The theory of finite frequency body wave synthetic seismogram in inhomogeneous elastic media, *Geophy. Journ. Roy. Aus. Soc.*, *63*, 691–713, 1980.

Fuchs, M., P. Silver, and J. D.E., Probing for shear wave anisotropy in the lowermost mantle beneath the Atlantic and Indian oceans, *EOS*, 1999.

Garnero, E. J., and D. V. Helmberger, Seismic detection of a thin laterally varying boundary layer at the base of the mantle beneath the central-Pacific, *Geophys. Res. Lett*, *23*, 977–980, 1996.

Garnero, E. J., and D. V. Helmberger, Further structural constraints and uncertainties of a thin laterally varying ultra low-velocity layer at the base of the mantle, *J. Geophys. Res.*, *103*, 12, 1998a.

Garnero, E. J., and D. V. Helmberger, Further structural constraints and uncertainties of a thin laterally ultralow-velocity layer at the base of the mantle, *J. Geophys. Res*, *103*, 12,495–12,509, 1998b.

Garnero, E. J., D. V. Helmberger, and G. Engen, Lateral variations near the core-mantle boundary, *Geophys. Res. Lett.*, *15*, 609–612, 1988.

Garnero, E. J., S. P. Grand, and D. V. Helmberger, Low p-wave velocity at the base of the mantle, *Geophys. Res. Lett*, *20*, 1843–1846, 1993.

Garnero, E. J., J. S. Revenaugh, Q. Williams, T. Lay, and L. H. Kellogg, Ultralow velocity zone at the core-mantle boundary, *in Geophysical Monograph Series*, *Edited by M. Gurnis et al., AGU, Washington DC*, 1998.

Gilbert, F., and D. Helmberger, Generalized ray theory for a layered sphere, *Geophy. Journ. Roy. Aus. Soc.*, *27*, 57–80, 1972.

Grand, S. P., Mantle shear structure beneath the Americas and surrounding oceans, *J. Geophys. Res.*, *99*, 11591–11622, 1994.

Grand, S. P., and D. V. Helmberger, Upper mantle shear structure of North America, *Geophys. J. R. Astron. Soc*, *76*, 399–438, 1984.

Grand, S. P., R. D. van der Hilst, and S. Widiyantoro, Global seismic tomography: A snapshot of convection in the earth, *GSA Today*, *7*, 1–7, 1997.

Gurnis, J., M., X. Mitrovica, J. Ritsema, and H. Van Heijst, Constraining mantle density structure using geological evidence of surface uplift rates: The case of the African super plume, *Geochem., Geophys., Geosys*, *http://www.g-cubed.org*, 2000.

Gurnis, M., I. Sidorin, S. Ni, J. Ritsema, and D. V. Helmberger, Dynamics of the lower mantle African upwelling consistent with differential travel times, *In preparation*, 1999.

Hager, B. H., R. W. Clayton, M. A. Richards, R. P. Comer, and A. M. Dziewonski, Lower mantle heterogeneity; dynamic topography and the geoid, *Nature*, *313*, 541–545, 1985.

Hedlin, M. A., and P. M. Shearer, An analysis of large-scale variations in small-scale mantle heterogeneity using global seismographic network recordings of precursors to PKP, *J. Geophys. Res.*, *105 No. B6*, 13,655–13,673, 2000.

Helmberger, D., The crust-mantle transition in the Bering sea, *Bull. Seis. Soc. Am.*, *58*, 179–214, 1968.

Helmberger, D., X. Song, and L. Zhu, Crustal structure beneath southern California from waveform modeling, *Journ. Geoph. Res.*, 2001.

Helmberger, D. V., E. J. Garnero, and X. Ding, Modeling two-dimensional structure at the core-mantle boundary, *J. Geophys. Res*, *101*, 13,963–13,972, 1996a.

Helmberger, D. V., L.-S. Zhao, and E. J. Garnero, Construction of synthetics for 2d structures; core phases, *Seismic Modeling of the Earth Structure, edited by E. Boschi, G. Ekstrom and A. Morelli*, 183–222, 1996b.

Helmberger, D. V., S. Ni, L. Wen, and J. Ritsema, Seismic evidence for ultra-low velocity zones beneath Africa and eastern Atlantic, *J. Geophys. Res*, *i105 B10*, 23,865–23,878, 2000.

Hong, T., and D. Helmberger, Glorified optics and wave propagationin nonplanar structure, *BSSA*, *68*, 1313–1330, 1988.

Kellogg, L. H., B. H. Hager, and R. D. van der Hilst, Compositional stratification of the deep mantle, *Science*, *283*, 1881–1884, 1999.

Kito, K., and M. Krueger, Distcontinuities from PcP precusors and scattered waves, *submited to Geoph. Res. Lett.*, 2001.

Lay, T., and E. J. Garnero, Scale lengths of shear velocity heterogeneity at the base of the mantle from S wave differential travel times, *J. Geophys. Res.*, *102*, 9887–9909, 1997.

Lay, T., and D. V. Helmberger, Body wave amplitude patterns and mantle attenuation variations across North America, *Geophys. J. R. Astron. Soc.*, *66*, 691–726, 1981.

Lay, T., and D. V. Helmberger, A lower mantle S wave triplication and the shear velocity structure of D", *Geophys. J. R. Astron. Soc.*, *75*, 799–838, 1983.

Lay, T., Q. Williams, and E. J. Garnero, The core-mantle boundary layer and deep earth dynamics, *Nature*, *392*, 461–468, 1998.

Li, X.-D., and B. Romanowicz, Global mantle shear velocity model developed using nonlinear asymptotic coupling theory, *J. Geophys. Res.*, *101*, 22, 1996.

Lithgow-Bertelloni, C., and P. G. Silver, Dynamic topography, plate driving forces and the African superswell, *Nature*, *395*, 269–272, 1998.

Liu, X. F., and A. M. Dziewonski, Lowermost mantle shear wave velocity structure (abstract), *EOS Trans. AGU*, *75*, 663, 1994.

Loper, D. E., and T. Lay, The core-mantle boundary region, *J. Geophys. Res.*, *100*, 6397–6420, 1995.

Luo, S., S. Ni, and D. Helmberger, Ultra low velocity zone revealed from multipathed PKPab, *submited to EPSL*, 2001.

Masters, T. G., and P. M. Shearer, Large-scale three dimensional structure of the mantle (abstract), *EOS Trans. AGU*, *73*, 201, 1992.

Masters, T. G., S. Johnson, G. Laske, and H. Bolton, A shear-velocity model of the mantle, *Royal Soc. Lon. Phil. Trans.*, *354*, 1385–1411, 1996.

Mori, J., and D. V. Helmberger, Localized boundary layer below the mid-pacific velocity anomaly identified from a PcP precursor, *J. Geophys. Res*, *100*, 20,359–20,365, 1995.

Ni, S., and D. V. Helmberger, Horizontal transition from fast (slab) to slow (plume) structures at the core-mantle boundary, *Earth. Plan. Sci. Lett.*, *in press*, 2001.

Ni, S., X. Ding, and D. V. Helmberger, Low velocity structure beneath Africa from forward modeling, *Earth Plan. Sci. Lett*, *170*, 497–507, 1999.

Ni, S., X. Ding, and D. V. Helmberger, Constructing synthetics from deep earth tomographic models, *Geophys. J. Int*, *140*, 71–82, 2000.

Olson, P., G. Schubert, and C. Anderson, Plume formation in the D" layer and the roughness of the core-mantle boundary, *Nature*, *327*, 409–413, 1987.

Partridge, T. C., and R. R. Maud, Geomorphic evolution of southern Africa since the mesozoic, *S. Afr. J. Geol*, *90*, 179–208, 1987.

Revenaugh, J., and R. Meyer, Seismic evidence of partial melt within a possibly ubiquitous low-velocity layer at the base of the mantle, *Science*, *277*, 670–673, 1997.

Ritsema, J., S. Ni, D. V. Helmberger, and H. P. Crotwell, Evidence for strong shear velocity reductions and velocity gradients in the lower mantle beneath Africa, *Geophys. Res. Lett.*, *25*, 4245–4248, 1998a.

Ritsema, J., A. A. Nyblade, T. J. Owens, C. A. Langston, and J. C. VanDecar, Upper mantle seismic velocity structure beneath Tanzania, *Journ. Geoph. Res.*, *103*, 21,201–21,213, 1998b.

Ritsema, J., H. van Heijst, and J. Woodhouse, Complex shear wave velocity structure imaged beneath Africa and iceland, *Science*, *286*, 1925–1928, 1999.

Schweitzer, J., and G. Muller, Anomalous difference traveltimes and amplitude ratios of SKS and SKKS from Tonga-Fiji events, *Geophys. Res. Lett.*, *13*, 1529–1532, 1986.

Sidorin, I., M. Gurnis, and D. V. Helmberger, Dynamics of a phase change at the base of the mantle consistent with seismological observations, *J. Geophys. Res.*, *104 No. B7*, 15,005–15,023, 1999.

Song, X., and D. Helmberger, High resolution modeling of regional phases, *CIT Thesis*, pp. 91–105, 1998.

Song, X., and D. V. Helmberger, Velocity structure near the inner core boundary from waveform modeling, *J. Geophys. Res.*, *97 No B5*, 6573–6586, 1992.

Steinbach, V., and D. A. Yuen, Viscous heating: A potential mechanism for the formation of the ultra low velocity zone, *submitted to the Earth Planet. Sci. Lett.*, 1999.

Su, W.-J., R. L. Woodward, and A. M. Dziewonski, Degree 12 model of shear velocity heterogeneity in the mantle, *J. Geophys. Res.*, *99*, 6945–6980, 1992.

Tackley, P. J., Three-dimensional simulations of mantle convection with thermo-chemical basal boundary layer: D", *The Core Mantle Boundary, edited by M. Gurnis et al.*, pp. 231–253, 1998.

Thomas, C., M. Weber, C. W. Wicks, and F. Scherbaum, Small scatterers in the lower mantle observed at German broadband arrays, *J. Geophys. Res.*, *107 No B7*, 15,073–15,088, 1999.

Thomas, C., K. M., and T. Heesom, Comparisons of D" anisotropy in three different regions, *SEDI Preceedings*, p. 53, 2000.

Thompson, P. F., and P. J. Tackley, Generation of mega-plumes from the core-mantle boundary in a compressible mantle with temperature-dependent viscosity, *Geophys. Res. Lett.*, *25*, 1999–2002, 1998.

van der Hilst, R. D., S. Widiyantoro, and E. R. Engdahl, Evidence for deep mantle circulation from global tomography, *Nature*, *386*, 578–584, 1997.

Van der Lee, S., D. Giardini, C. Estabrook, A. Deschamps, and C. Chiarabba., New temporary broadband stations in the larger Mediterranean region, *ORFEUS Newsletter*, *1*, 5, 1999.

Vidale, J., and D. Helmberger, Elastic finite-difference modeling of the 1971 Sanfernando, California earthquake, *BSSA*, *78*, 122–141, 1988.

Vidale, J. E., and M. A. H. Hedlin, Evidence for partial melt at the core-mantle boundary north of Tonga from the strong scattering of seismic waves, *Nature*, *391*, 682–685, 1998.

Wahba, G., Spline models for observational data, *Society for Industrial and Applied Mathematics, Philadelphia, Pennsylvania*, pp. 45–52, 1990.

Wen, L., A chemical-thermal layer beneath Atlantic, *Sumitted to Nature*, 2001.

Wen, L., and D. V. Helmberger, A two-dimensional P-SV hybrid method and its application to modeling localized structures near the core-mantle boundary, *J. Geophys. Res*, *103*, 17,901–17,918, 1998a.

Wen, L., and D. V. Helmberger, Ultra-low velocity zones near the core-mantle boundary from broadband PKP precursors, *Science*, *279*, 1701–1703, 1998b.

Wiggins, R., Body wave amplitude calculations, ii, *Geophy. Journ. Roy. Aus. Soc.*, *46*, 1–10, 1976.

Williams, Q., and E. J. Garnero, Seismic evidence for partial melt at the base of earth's mantle, *Science*, *273*, 1528–1530, 1996.

Wysession, M., E. Okal, and C. Bina, The structure of the core mantle boundary from diffracted waves, *Journ. Geoph. Res.*, *97*, 8749–8764, 1995.